Institute of Physics

University of Graz

Diploma thesis

in Physics

submitted by

Stefan A. Brünner

born in Fürstenfeld, Austria

2013

Study of radon adsorption on activated carbon for a purification system in XENON1T

This diploma thesis has been carried out by

Stefan A. Brünner

at the

Max-Planck-Institut fuer Kernphysik

under the supervision of

Prof. Dr. Manfred Lindner

Institut für Physik

Karl-Franzens-Universität Graz

Diplomarbeit

Im Studiengang Physik

vorgelegt von

Stefan A. Brünner

geboren in Fürstenfeld, Österreich

2013

Untersuchung der Adsorption von Radon an Aktivkohle für ein Reinigungssytem in XENON1T

Die Diplomarbeit wurde von

Stefan A. Brünner

ausgeführt am

Max-Planck-Institut für Kernphysik

unter der Betreuung von

Herrn Prof. Dr. Manfred Lindner

Study of radon adsorption on activated carbon for a purification system in XENON1T

Dealing with extremely low event rates, background reduction and discrimination are essential challenges in dark matter direct detection experiments. The major contribution to the internal background in XENON100 is due to the radioactive noble gas radon which emanates from the detector walls into the liquid xenon target. To gain higher sensitivity, the radon contamination of the XENON1T detector, start of construction is in 2013, should be minimized due to careful material selection and a radon purification system based on adsorption. In this thesis, Monte Carlo simulations are performed to study the internal background induced by the radioactive decay of radon and its progenies for a XENON1T model detector. Then, an experimental setup to measure the radon adsorption on porous materials is introduced and tested. A procedure for measuring simultaneously the adsorption of radon and a second present gas component is given. Finally, results of the radon adsorption on activated carbon samples in presence of xenon are shown. These measurements will help to select the most appropriate adsorbent for the radon purification system in the XENON1T experiment.

Untersuchung der Adsorption von Radon an Aktivkohle für ein Reinigungssystem in XENON1T

Reduzierung und Erkennung von Untergrundsignalen ist für Experimente zur direkten Suche dunkler Materie aufgrund der geringen Ereignis-Rate von außerordentlicher Wichtigkeit. Hauptverursacher des internen Untergrundes in XENON100 ist das radioaktive Edelgas Radon, welches aus den Detektorwänden in das Detektionsmaterial, bestehend aus flüssigem Xenon, emaniert. Um eine möglichst hohe Sensitivität des XENON1T Detektors, welcher ab 2013 gebaut wird, zu garantieren, wird nicht nur besonderes Augenmerk auf die Reinheit der verwendeten Materialien gelegt, sondern auch ein auf Adsorption basierendes Radon-Reinigungssystem realisiert. In dieser Diplomarbeit wird zunächst der durch Radon und dessen Tochterisotope verursachte Untergrund für ein Modell des XENON1T Detektors mit Hilfe von Monte Carlo Simulationen untersucht. Anschließend wird ein Versuchsaufbau zur Durchführung von Messungen zur Radon-Adsorption an porösen Materialien beschrieben und getestet. Ein Verfahren zur gleichzeitigen Bestimmung der Adsorption von Radon und einer möglichen weiteren Gaskomponente im System wird gezeigt. Schließlich werden Messungen der Adsorption von Radon an Aktivkohle im Beisein von Xenon durchgeführt. Unter Berücksichtigung der hier gezeigten Resultate soll der für die Anwendung in der Radon-Reinigung geeignetste Adsorber ermittelt werden.

Contents

Chapter 1

Introduction

The mystery of dark matter began in 1933 with a momentous observation of the Swiss astronomer Fritz Zwicky. He found that the velocity dispersion of galaxies in the Coma cluster was far too large to be explained by the gravitational interaction of the luminous matter alone. Hence Zwicky inferred the existence of large amounts of unseen, non-luminous, thus so-called *dark matter* [1].
Since then many other convincing evidences for the existence of dark matter have been found at very different astronomical scales and it is furthermore a key-ingredient of the highly sophisticated ΛCDM model which successfully explains decisive astrophysical observations[1]. The nature and identity of the dark matter, however, is still unknown. Cosmology suggests that the majority of the dark matter has no baryonic nature. Baryons contribute only 4-5% to the total energy density of the universe. Most of the mass, approximately 23% seems to be provided by dark matter particles beyond the Standard Model of particle physics. Several extensions of the model naturally predict potential dark matter candidates. 72% are attributed to the *dark energy*.
Dark matter is certainly one of the most challenging problems in modern Cosmology and its experimental proof a milestone in natural science. Numerous experiments try with different strategies to detect dark matter particles. Altough this effort lead to several constraints on its properties, a clear proof is still missing.

This chapter gives a short introduction to dark matter without striving for completeness. In the first section 1.1 further evidences for its existence are introduced. Then, in section 1.2 properties and possible dark matter candidates are discussed.

[1] The ΛCDM model (cosmological constant Λ, *Cold Dark Matter*) is also referred to as the standard model of Cosmology. It provides explanations for the cosmic microwave background, the universes large scale structure, the expansion of the universe and the abundances of the light elements.

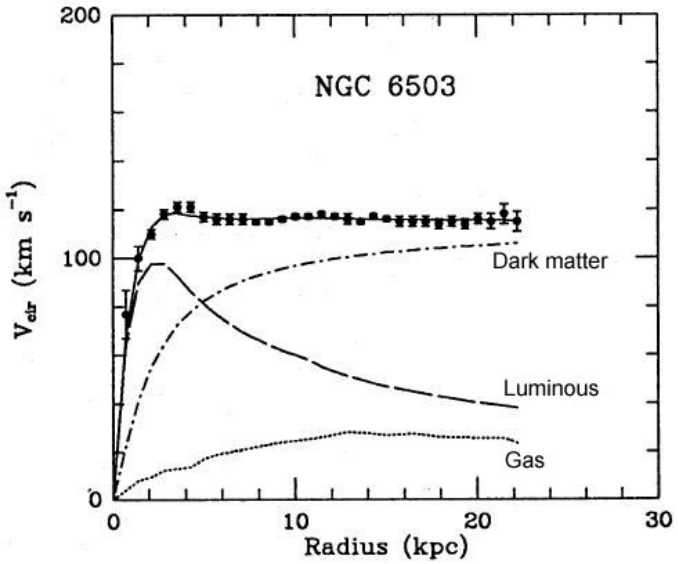

Figure 1.1: Rotation curve of NGC 6503 [6]. The flat shape indicates a non-luminous mass distribution outside the galactic disk.

In section 1.3 the detecting strategies of current dark matter experiments are introduced. For further reading on dark matter [2], [3], [4] and [5] are recommended.

1.1 Observational evidence for dark matter

After the first convincing evidence for dark matter in galaxy clusters, found by Zwicky, several other observations, made in the last decades, suggest its existence. The rotation curves of matter in galaxies, like the one shown in figure 1.1, are a famous hint for dark matter on galactic scales.
It is expected from Newtonian dynamics, that the rotational velocity of a star[2] at the distance r from the galactic center is related to the mass $M(r)$ within the radius by the equation

$$v_{rot}(r) = \sqrt{\frac{G\,M(r)}{r}}\ . \tag{1.1}$$

According to this formula, when r goes beyond the radius of the galactic disk and consequently $M(r)$ is constant, the rotational velocity should show a *Keplerian* $\propto v^{-1/2}$ behavior (in figure 1.1 labelled as *Luminous*).
The actual observed curve, however, is flat at large distances where no luminous matter is found [6]. This discrepancy can be solved by assuming an additional mass distribution $M \propto r$ outside the galactic disk, often referred to as the *dark matter halo* (*Dark matter* in figure 1.1).

[2]Since individual stars are too faint, clouds of hydrogen and helium within the galaxy are usually used for the measurements.

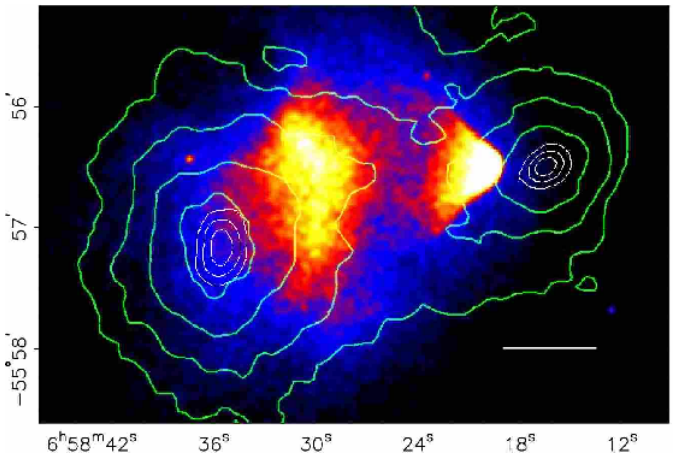

Figure 1.2: The Bullet Cluster [7]. Comparing the mass density contours (green lines) with the X-ray image of the visible matter shows a significant mismatch.

Another strong evidence for dark matter comes from the observation of colliding galaxy clusters. Most famous example is the *Bullet cluster* [7]. The majority of the baryonic mass of galaxy clusters is hot gas. This intergalactic gas is compressed and causes strong X-ray emission when clusters are colliding. Dark matter, on the other hand, is supposed to pass through the collision without interacting with any other matter. As a result luminous and dark matter get separated. Gravitational lensing allowes to map the total mass distribution of the clusters (green contour lines in figure 1.2) while the visible matter can be located by its radiation (see colored areas in figure 1.2). The observed discrepancy between these mass distributions is an impressive evidence for the existence of collisionless dark matter.
Other evidences come from Cosmology. Although the Cosmic Microwave Background (CMB) [8] is remarkably uniform (T= 2.725 K), sensitive instruments like the COBE satellite [9] and WAMP [10], detect anisotropies (fluctuations) of about $30\,\mu$K. Since this anisotropies are dependent on the composition of the universe (baryonic matter, non-baryonic matter, dark energy) the analysis of the CMB allowes to quantify the dark matter content (usually expressed relatively to the universe's critical energy density, see appendix A). The obtained result suggests that the matter contribution to the total energy density in our universe is only 27-28%. Moreover, most of the matter has to be non-baryonic to explain the observed data.
This result is in remarkable agreement with the value of the baryonic mass density obtained from the *Big Bang Nucleosynthesis* (BBN) [11]. In this short period of the early universe, the light elements deuterium, helium and traces of lithium have been created. The rates of the required production reactions are dependend on the baryon density $\eta \equiv n_B/n_\gamma$ (normalized to the photon number density). A great success of the Big Bang model is the explanation of the observed abundances by assuming $\eta \cdot 10^{10}$ in the range of 5.1-6.5 (95% CL) [11]. Since n_γ is known from the Cosmic Microwave Background (CMB) one can infer the range of todays baryon

mass density.

1.2 Dark matter properties and candidates

Although there are strong evidences for dark matter at different scales, the identity of basically all dark matter in the universe is still unknown. It was tried to explain dark matter wit baryonic objects classified as Massive Compact Halo Objects (MACHO). This includes brown dwarfs, neutron stars and black holes. The rather rare discoveries of those objects, but also Cosmology, however, suggests that the majority of dark matter has to be non-baryonic. Other approaches pursue to unravel the mystery of dark matter by modifying the laws of gravity instead of introducing unseen matter. The problem of these MOND theories (Modified Newtonian Dynamics) is that they cannot describe all the various evidences for dark matter at different scales (see section 1.1 at the same time. Therefore the theory of particle dark matter is well established.
The only possible candidates within the Standard Model are neutrinos since they are known to have mass and interact only weakly. Their contribution, however, was also found to be subdominant. Neutrinos are referred to as *hot dark matter* since they are relativistic particles (in contrast to the earlier mentioned *cold dark matter*). The major problem is that the structure formation in our universe cannot be explained by relativistic dark matter due to its high velocity.

Candidate particles to explain dark matter have to satisfy several conditions. They have to be non-baryonic and *cold* (i.e. non-relativistic) and do not interact electromagentically. Moreover dark matter needs to be stable or have a lifetime large compared to the age of the universe, since otherwise it would have been decayed by now. Finally any dark matter candidate has to have a relic density which fits to the predictions from Cosmology.

So called *Weakly Interacting Massive Particles* (WIMPs) are a very promising candidate for dark matter particles. Since no particular dark matter particle has been found yet, the term WIMP refers generally to electrically neutral, massive particles which, like neutrinos, only have weak interaction with baryonic matter. Examples for possible WIMP candidates naturally occur in several extensions of the Standard Model of particle physics. Most notable is the lightest supersymmetric particle (LSP) in SUSY models with exact R-parity[3] [12]. But also the lightest particle in the *Kaluza-Klein theory* is an example for a WIMP candidate [13].
As shown in e.g. [14] the relic density of WIMPs can be calculated by assuming that in the early universe the dark matter was in a thermal equilibrium with the *cos-*

[3] *Neutralino* or *sneutrino* are examples for the LSP in different SUSY-models.

mic soup, i.e. the creation and annihilation processes are equally efficient. As the universe expanded, the WIMPs dropped out of equilibrium and formed a thermal relic. Assuming now a dark matter particle with a mass around the electroweak scale (GeV-TeV scale), the calculated relic density is similar to the predicted dark matter density if the particles annihilation cross section is also approximately at the electroweak scale.

Although WIMPs are very well motivated, there are several other possible dark matter particles. *Axions* for instance or *SuperWIMPs* and *sterile neutrinos* are a promising candidates as well. More information can be found in [3].

1.3 Strategies for dark matter detection

In the last sections non-baryonic dark matter has been motivated by strong observational evidences but also by the natural appearance of possible candidates in required extensions of the Standard Model of particle physics. The identity of the dark matter particle(s) and its properties (mass, spin, etc.), however, will stay a mystery unless its experimentally detection succeeds. For this purpose many collaborations all over the world made a lot of effort to construct and run detectors based on three different detection strategies.
In this section these strategies are introduced where the focus is clearly on *direct detection*, since this work is written in the context of the XENON project as an example for a direct detection experiment (see chapter 2).

1.3.1 Direct detection

Above discussed observational evidences for dark matter (like the flat galaxy rotation curves, etc.) suggest that galaxies are embedded in halos of dark matter particles. From halo models of the Milky Way, the local dark matter density is found to be $\rho_0 = 0.389 \pm 0.025\,\mathrm{GeV\,cm^{-3}}$ [15]. The local velocity distribution $f(v)$ of the dark matter particles can be described by an Gaussian distribution [16] with the local[4]circular velocity $v_c = (220 \pm 20)\,\mathrm{km\,s^{-1}}$ as mean value (in the halo rest frame). There is an upper velocity limit for dark matter given by the galactic escape velocity $v_{esc} = (544 \pm 50)\,\mathrm{km\,s^{-1}}$. These dark matter particles usually penetrate the Earth without any interaction. However, occasionally they scatter on ordinary matter which causes a recoil of the target particle. Direct detection experiments attempt to detect these rare events.

[4] v_c is dependent on the distance to the galactic center. *Local* means $v_c = v_c(r = R_0)$, with R_0 as the Earths distance.

The differential event rate

The *differential event rate* is the most interesting quantity for direct detection experiments since it gives the number of expected events per nuclear recoil energy and per unit time for a target of a defined size. In case of elastic scattering[5] of a WIMP on an atomic nucleus used as a target, the differential event rate for a direct detection experiment can be expressed as:

$$\frac{dR}{dE_{nr}} = N_N \frac{\rho_0}{m_\chi} \int_{v_{min}}^{v_{esc}} dv\, f(v)\, v \frac{d\sigma}{dE_{nr}} \,, \tag{1.2}$$

where ρ_0 and $f(v)$ are the above introduced local dark matter density and velocity distribution respectively, while m_χ labels the WIMP mass. Furthermore the differential rate is dependend on the total number of target nuclei N_N and the WIMP-nucleus differential cross section $d\sigma/dE_{nr}$.
The upper integration limit is given by the galactic escape velocity introduced above. The actual upper limit, however, is given by the energy threshold of a particular detector (usually the detectors energy range is limited). The lower limit is set by the minimum recoil energy required to produce a detection signal in an dark matter detector. The transferred recoil energy in case of elastic scattering is given in the center-of-mass frame by

$$E_{nr} = \frac{p^2}{2\, m_N} = \frac{\mu_N^2\, v^2}{m_N} (1 - \cos\theta) \,, \tag{1.3}$$

where p is the momentum transfer, m_N the mass of the target nucleus, μ_N the reduced WIMP-nucleus mass and θ the scattering angle.
With the help of equation 1.3 one obtains for the lower integration limit

$$v_{min} = \sqrt{\frac{m_N\, E_{nr}}{2\, \mu_N^2}} \,. \tag{1.4}$$

The differential cross section $d\sigma/dE_{nr}$ in equation 1.2 stands for the particle physics contribution to the event rate. It depends on the nature of the WIMP-nucleus interaction. It has to be distinguished between *spin-independent* (SI) and *spin-dependent* (SD) interaction. SD interaction depends on the WIMP's spin and the spin content from the target nucleon[6]. See e.g. [17] for more detail.

[5] In case of *inelastic scattering* the target nucleus is excited in the scattering process and not all energy goes into the nuclear recoil.

[6] SD coupling involves axial vector currents while models for SI coupling are realized with scalar or vector currents.

In case of SI interaction the differential WIMP-nucleus cross section is given by

$$\frac{d\sigma}{dE_{nr}} = \frac{m_N\,\sigma_{SI}\,F^2_{E_{nr}}}{2\,\mu_N^2\,v^2}\ . \tag{1.5}$$

In this expression $F^2_{E_{nr}}$ is the *nuclear form factor* and σ_{SI} the integrated SI cross section of WIMP-nucleus scattering [18]

$$\sigma_{SI} = \frac{[Z\,f_p + (A-Z)\,f_n]^2}{f_p^2}\,\frac{\mu_\chi^2}{\mu_p^2}\,\sigma_p^{SI}\ . \tag{1.6}$$

As one can see in above equation, σ_{SI} does not depend on form factors anymore but on the nuclear structure of the target: Z and A are the charge and atomic mass of the nucleus and $f_{p,n}$ are the SI WIMP-proton/neutron couplings. σ_p^{SI} is the SI WIMP-proton cross section. Since $f_p \approx f_n$ equation 1.6 can be rewritten as

$$\sigma_{SI} = A^2\,\frac{\mu_\chi^2}{\mu_p^2}\,\sigma_p^{SI}\ . \tag{1.7}$$

In case of a SI coherent scatter on nucleons, the differential event rate obtained by inserting equation 1.7 into equation 1.2, is proportional to A^2. Consequently, for SI dark matter search, target nuclei with high mass, like Xe or Ge, are preferred compared to those with a small atomic mass number A.

In case of SD WIMP-nucleus coupling, however, the sensitivity of an experiment depends on the nuclear spin factor. Here nuclei with odd mass number like ^{19}F, ^{73}Ge or ^{127}I are used as targets. In the XENON project (see chapter 2) the isotopes ^{129}Xe and ^{131}Xe are used to set SD limits on the WIMP-nuclon (WIMP-proton, WIMP-neutron) cross sections [19].

By integrating the differential event rate, using the detectors upper and lower energy threshold for the integration limits (equation 1.4 is used for conversion to v_{min} and $v_{max} < v_{esc}$), one obtains the *total event rate*. Expectations ranges usually from 1 to 10^{-3} events per kg detector material and year [20] depending on the WIMP-nucleus cross section.

Direct detection experiments and detection techniques

For direct dark matter detection the transferred energy from the WIMP-nucleus scattering needs to be transformed into a detection signal. Dedicated low background experiments with low energy threshold have been constructed for this purpose based on different detection techniques.

The Edelweiss [21], CDMS [22], and CRESST [23] experiments are solid-state cryogenic detectors [20] operated at sub-Kelvin temperatures. Energy depositions in the target material (germanium, silicon or $CaWO_4$) cause a temperature change which can be measured due to phonons. In addition to the phonon signal these experiments are able to detect ionization (CDMS and Edelweiss) or scintillation (CRESST) signals. The XMASS [24], ZEPLIN-III [25], DarkSide [26] or XENON100 [27] experiments, on the other hand, use liquid xenon or liquid argon, as target material. Both noble gases show good scintillation and ionization properties, which allow to read out light and charge signals in case of an energy deposit in the detector. Reading out two signals (phonons-charge, charge-light, light-phonons) simultaneously, provides a powerful discrimination against background (see 3 in case of XENON100).
A further detection technique is used by the PICASSO [28], SIMPLE [29] and COUPP [30] experiments. As the sensitive material they use *superheated liquids*. They are heated well above the boiling point and are therefore in a metastable state. A small energy deposit (from a WIMP scatter) causes a phase-transition, leading to the formation of bubbles which are detected optically and acoustically. Having fluorine in the target material, these detectors are able to give strong bounds on SI interactions.
Up to now three experiments have reported a possible signature for a dark matter signal. The DAMA/LIBRA experiment [31] uses a scintillating NaI(Tl) (thallium-doped sodium iodide) crystals as target material. Since the Earth orbits the Sun its relative velocity to the dark matter halo and consequently the expected dark matter event rate varies. The DAMA/LIBRA collaboration observed an annual modulation in their low energy rate with a significance of $8.9\,\sigma$ [31] attributed to dark matter.
The CoGeNT experiment attempts to detect energy deposits induced by WIMPs in an ultra-low background germanium detector due to ionization signals. In [32] the collaboration reports that WIMPs with a mass in the range $m_\chi \sim 7 - 11\,\mathrm{GeV/c^2}$ would provide a good fit to the data.
Also the already introduced CRESST-II dark matter search experiment reported in [22] that with a statistical significance of more than $4\,\sigma$ events with an unknown origin contribute to their observed signals. Scattering of WIMPs with mass either $m_\chi = 25.3\,\mathrm{GeV/c^2}$ or $m_\chi = 11.6\,\mathrm{GeV/c^2}$ could be an explanation.
It is important to emphasize that these potential WIMP signals challenge each other and results of other direct detection experiments like XENON100 (see figure 2.3).

1.3.2 Indirect detection

Since dark matter particles can annihilate an alternative to direct detection is the observation of the annihilation products predicted by theoretical models. Since the annihilation rate is proportional to the square of the dark matter density, mass accumulations like the center of our Galaxy, the Sun or the Earth are the observed regions.
Gamma rays, for instance, could be produced in dark matter annihilation processes. A resulting continuous spectrum is as possible as a monoenergetic gamma line which is furthermore dependend on the dark matter particle's mass. The Fermi Gamma-ray Space Telescope [33], for example, is searching for this gamma signatures. Other experiments like IceCube [34] aim to detect high energetic neutrinos produced in dark matter annihilation processes in the center of the Sun or Earth. The PAMELA experiment [35], on the other hand attempts to detect positrons. Crucial in indirect detection experiments is the astronomical background (galactic, extragalactic) which can overlay the signals.
Since indirect detection experiments are sensitive to other dark matter models they are complementary to direct detection.

1.3.3 Detection at the LHC

Another strategy is to produce dark matter particles in accelerators like the Large Hadron Collider (LHC) in Geneva, Switzerland. In high energetic collisions new heavy particles might be created (e.g. SUSY particles) which then decay, amongst others, into dark matter particles (in case of SUSY particles to the LSP). Dark matter particles are neutral and stable and will therefore most likely escape the detector. However, since they carry momentum and energy, it should be possible to reconstruct them due to the missing amount of these quantities. For detailed information on dark matter and the LHC, [36] and [37] is recommended.

1.4 Motivation and outline

Dealing with extremely low event rates makes background reduction and discrimination to the most challenging tasks in dark matter search. In the XENON project, introduced in chapter 2, beside the so-called external background, the radioactive decay of the noble gas ^{222}Rn and its progenies are dominating the total background. In chapter 3 of this work, the radon induced background is analyzed by simulations of the ^{222}Rn decay chain in liquid xenon. After studying the contributions of the single daughter isotopes, the total radon background spectrum is obtained.
The detector of the next generation within the XENON project, the XENON1T de-

tector, aims for gaining a factor 100 in terms of sensitivity compared to XENON1T. To achieve this goal, the radon contamination needs to be minimized due to careful material selection but also due to a radon removal system based on adsorption. In chapter 4 an experimental setup is introduced which allows to select a suited adsorbent for application in the removal system, based on its capability to adsorb radon in presence of xenon.

Chapter 2

The XENON project

The XENON project aims to detect WIMP dark matter using liquid xenon (LXe) as detector medium. The first experiment in this project, XENON10, was deployed in 2006 at the Gran Sasso National Laboratory (LNGS) and operated with 25 kg LXe. After successful operation, the at that time strongest constraint on spin-independent (SI) WIMP-nucleon cross-section over a wide range of WIMP masses was published [38]. As a next step the XENON100 detector, operated with about 160 kg LXe, has been built and is currently running. The latest published data set todays most stringent limit on SI WIMP-nucleon cross section for WIMP-masses $m_\chi > 8\,\mathrm{GeV/c^2}$ [39].
At the beginning of this chapter, LXe as target material for dark matter detection is motivated. The XENON100 detector and the experiment XENON1T, currently under construction, are discussed as the central topics of this chapter.

2.1 Liquid xenon as detector medium

Using LXe as target material yields several advantages. Most important are its ionization and scintillation properties. Energy deposits in LXe cause the production of charge carriers but also scintillation light. This property is shared with liquid argon, which is also used as detector medium in dark matter experiments (see e.g. DarkSide [26], WArP [40], ArDM [41]). LXe shows the largest *ionization yield*, defined as the number of electron-ion pairs produced per unit adsorbed energy, among all liquid noble gases [42]. The VUV (vacuum ultraviolet) *scintillation light* at 178 nm is produced due the de-excitation of xenon *excimers* [42] which arise in the scattering processes. As will be discussed in the following section 2.2 these two properties of LXe, ionization and scintillation light, are used as detection signals in the XENON experiment.
The high density of $\sim 3\,\mathrm{g/cm^3}$ and the atomic number of 54 of LXe cause fur-

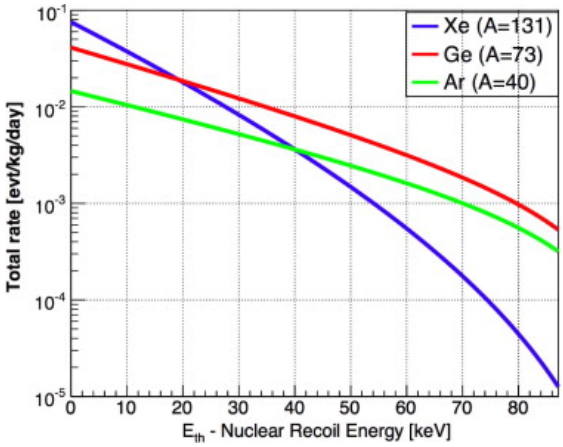

Figure 2.1: Spin-independent event rate calculated for different target materials assuming a WIMP mass of $100\,\mathrm{GeV/c^2}$ and a WIMP-nucleus cross-section of $10^{-43}\,\mathrm{cm^2}$. Figure taken from [43].

thermore a high stopping power. It consequently shields penetrating radiation efficiently. This *self-shielding* is an important property to achieve ultra-low background rates in experiments like XENON100 (see section 2.2.3).
As mentioned in section 1.3, the spin-independent (SI) WIMP-nucleus cross-section scales with the square of the mass number of the nucleus. This makes xenon, with a mean atomic weight of A=131.30, an ideal detection material. In figure 2.1 the calculated event rates for different target materials used in direct detection experiments are given considering a WIMP mass of $100\,\mathrm{GeV/c^2}$ and a SI WIMP-nucleus cross-section of $10^{-43}\,\mathrm{cm^2}$ [43]. One can see that for all materials, particularly for xenon, the event rate decreases quickly at high WIMP recoil energies. For low energy thresholds, however, xenon shows an enhanced event rate. Approximately 50% of the xenon isotopes have an odd mass number. As already mentioned in section 1.3 detectors using xenon as a target material are therefore also sensitive to SD WIMP-nucleus interactions due to the nuclear spin factor of these isotopes. As background reduction is the most challenging task for direct dark matter detection (see section 2.2.3), another important advantage of xenon is that is has, with the exception of ^{136}Xe, no long-lived radioactive isotopes. Detailed information on the properties of LXe and its use in particle and astroparticle experiments can be found in [42].

2.2 XENON100

XENON100, located at the LNGS, is one of the leading dark matter direct detection experiments. With the latest published results it sets the most stringent limit on SI WIMP-nucleon scattering for $m_\chi > 8\,\mathrm{GeV/c^2}$ [39]. As shown in figure 2.2 the limit (blue line) has its minimum at $\sigma = 2 \cdot 10^{-45}$ at a WIMP mass of $m_\chi = 55\,\mathrm{GeV/c^2}$ and 90% confidence level. The green and yellow bands give the expected sensitivity in absence of a dark matter signal. The light and dark gray

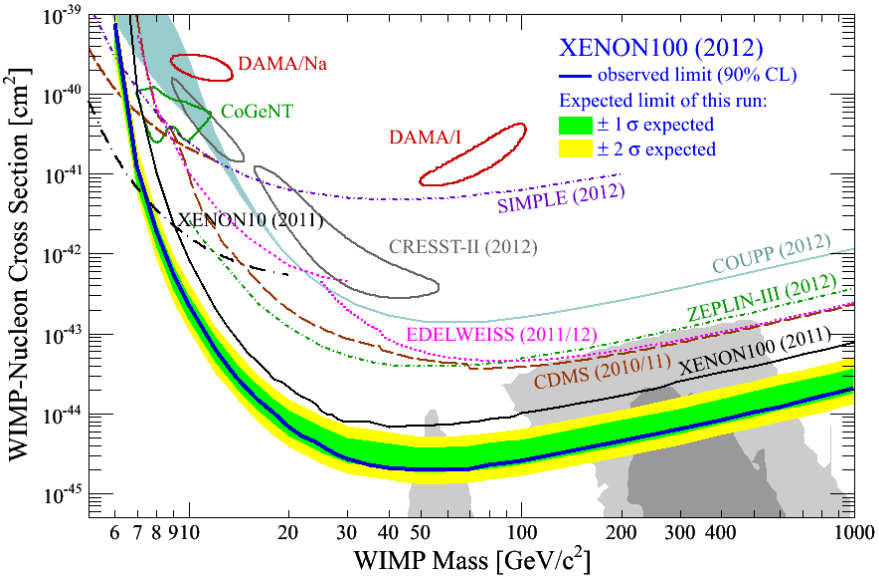

Figure 2.2: XENON100 results from 225 live days data taking for spin-independent WIMP-nucleon cross-section [39]. The obtained limit is the most stringent for m_χ >8 GeV/c^2. The green and yellow bands give the expected sensitivity for the 225 days data, while the various colored lines correspond to the results of other dark matter direct detection experiments.

areas are 1 σ and 2 *sigma* expectations for WIMP parameters in supersymmetric models (CMSSM) respectively (combined region using [44], [45], [46]). The other colored lines are limits obtained by other dark matter direct detection experiments. In case of DAMA, CoGeNT and CRESST-II, the enclosed areas correspond to their published evidences for dark matter. As shown in figure 2.2, the XENON100 result is in conflict with DAMA, CoGeNT and CRESST-II for SI WIMP-nucleus interaction. The latest results for SD WIMP-nucleon (WIMP-proton and WIMP-neutron) interaction have been published in [19].

In SD case, WIMPs couple to the total spin content of the target nucleus. Therefore the two xenon isotopes ^{129}Xe and ^{131}Xe are used for analysis since they have an odd number of neutrons. For WIMP masses >6 GeV/c^2, XENON100 reports the most stringent upper limits on WIMP-neutron cross-section with a minimum of $3.5{\cdot}10^{-40}$ cm^2 at a WIMP mass of 45 GeV/c^2 (see figure 2.3). For the WIMP-proton cross-section, XENON100 reaches a sensitivity of $\sim 1{\cdot}10^{-38}$ cm^2, comparable with other direct detection experiments.

In this section the working principle of the two-phase (liquid-gas) *time projection chamber* (TPC), as used in the XENON project, is explained. Then, the XENON100 detector design is introduced without getting into detail. A compre-

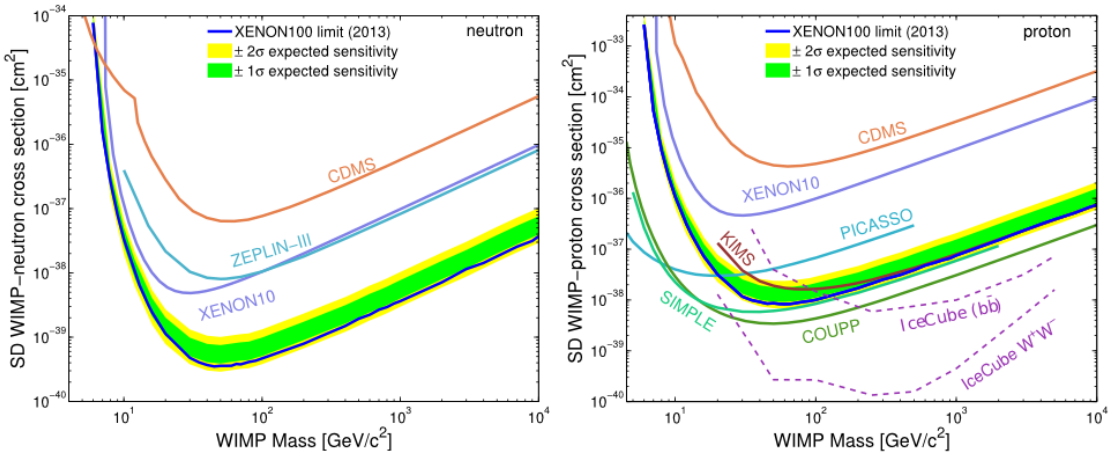

Figure 2.3: XENON100 results from 225 live days data taking for spin-dependent WIMP-neutron (left) and WIMP-proton (right) cross-section [19].

hensive detector description for XENON100 can be found in [27]. Some important signal/background discrimination techniques in XENON100 are given in the last part of this section.

2.2.1 Working principle of a liquid xenon TPC

In case of a scattering event in the LXe target, the transfered energy causes scintillation light at 178 nm due to the de-excitation of xenon excimers. Since xenon does not absorb its scintillation light, it penetrates the LXe target and can be detected by *photomultiplier tubes* (PMTs) which are arranged in arrays at the top and the bottom of the TPC (see figure 2.4). The prompt light, emitted immediately after the scattering process, is called *direct scintillation light* and labelled as S1. Beside scintillation the deposited recoil energy causes also ionization. Due to an electric field (*Cathode* in figure 2.4), the free electrons from ionization are drifted towards the top of the TPC. When the electrons reach the liquid/gas interface[1], they get extracted into the gas phase by an extraction field of ∼12 kV/cm (*Anode* in figure 2.4). In the gaseous xenon (GXe) the extracted electrons cause a *secondary* or *proportional scintillation light* S2, which is also detected by the PMTs. As indicated in figure 2.4 (right), the ratio of the S2 and S1 signals depends on the type of recoil. This fact is efficiently used to discriminate electromagnetic background (electronic recoils due to electromagnetic interactions with atomic shell of the xenon target) from a WIMP signal (nuclear recoils due to elastic scattering with the xenon nucleus). This discrimination technique is discussed in the following section in more

[1]XENON100 uses a two-phase TPC, i.e. there is a liquid gas interface inside the TPC. The top PMT arrays are surrounded by the gaseous xenon (GXe).

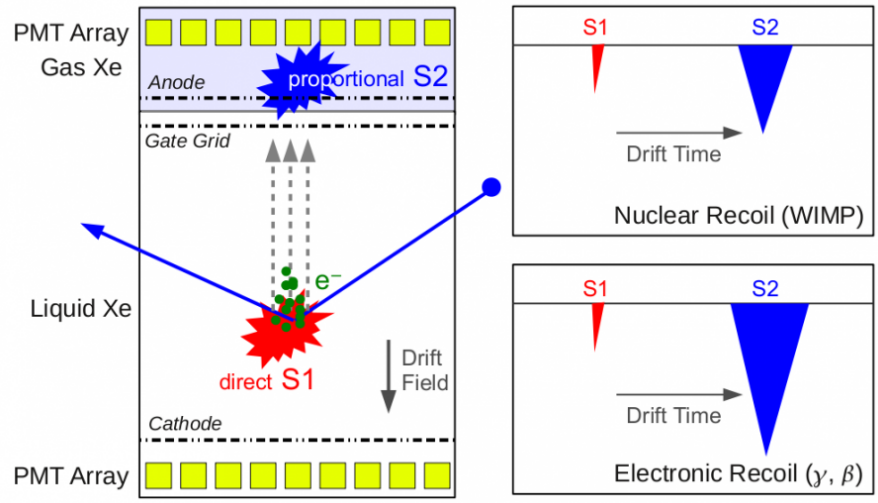

Figure 2.4: (Left) The XENON detection principle with a two-phase time projection chamber. (Right) Sketch of two events, electronic and nuclear recoil. As discussed in chapter 3 the ratio of the S2 and S1 signal can be used to discriminate background events (electronic recoils) from events induced by WIMPs (nuclear recoils). Figure taken from [27].

detail.
The detection signals S1 and S2 are measured in photons (PE), detected by the PMTs. The size of the signals, in PE, naturally depends on the deposited recoil energy of a scattering process. The conversion to the actual recoil energy in keV_{nr}[2] is given by

$$E_{nr} = \frac{\mathrm{S1}}{\mathcal{L}_{eff} \cdot L_y} \frac{S_{ee}}{S_{nr}} \tag{2.1}$$

for the S1 signal and

$$E_{nr} = \frac{\mathrm{S2}}{L_q \cdot \mathcal{Q}(E)} \tag{2.2}$$

for the S2 signal. Both equations hold only in case of nuclear recoil events. The essential parameters for this conversion are the *relative scintillation efficiency* $\mathcal{L}_{eff}$ and the *ionization yield* $\mathcal{Q}$ respectively. $\mathcal{L}_{eff}$ represents the suppression of the scintillation yield for nuclear recoils with respect to that of electronic recoils, obtained for an energy of 122 keV_{ee} at zero electric field. $\mathcal{Q}$, already defined in the last section, is the number of electron-ion pairs produced per unit adsorbed energy.

[2]The energy calculated with equations 2.1 and 2.2 are only reconstructed energies. The unit keV_{nr} has been chosen to emphasize this fact.

The other parameters are quantities related to the detector. S_{ee} and S_{nr} are quenching factors which give the suppression of scintillation light due to the presence of an electric field for electronic and nuclear recoils respectively. L_y is the *light yield* of the detector and defined as the yield measured for the 122 keV$_{ee}$ γ-line of a ^{57}Co source. L_q represents the *charge yield*, defined as the number of photons per electron which gets extracted into the gas-phase of the TPC.
In figure 2.4 one can see that the two detection signals, S1 and S2, are temporally separated (right picture). While the S1 signal is prompt, it takes some time until the electrons, which later cause the S2 signal, drift towards the liquid/gas interface. Due to the homogeneous electric field and the consequently constant drift-velocity, the drift-time can be used to extract the depth (by convention the z-coordinate) of the detected event. The (x,y)-coordinate, on the other hand, can be determined by the hit pattern of the PMTs which detect the S2 signal. As discussed in the following section, the knowledge of the spatial position of an event provides an important tool to identify background events.

2.2.2 XENON100 detector design

The XENON100 TPC has a height of 30.5 cm a cylindrical shape with a radius of 15.3 cm. PTFE (polytetrafluorethylen) is used as construction material since it is a good reflector for VUV scintillation light. 98 PMTs are arranged at the top (in the GXe) and 80 at the bottom of the TPC for detecting the S1 and S2 signals. The TPC contains 62 kg LXe and another 99 kg surround the whole TPC from all sides (4π coverage) in a layer of about 4 cm. This additional LXe is observed by 64 PMTs and is used as a veto. Every event detected in the TPC has to show no coincidence with the LXe veto to be accepted. This effectively reduces background originating from outside the detector. The TPC and the LXe veto are mounted inside a stainless steel cryostat which is cooled down to the operation temperature of $-91\,^{\circ}$C. Finally, a passive shield of layers of copper, polyethylene, lead and water surrounds the detector [27].
For successful detector operation, the xenon needs a continuous purification since impurities affect the detection signals. Electronegative impurities like oxygen, for instance, lead to a suppression of the charge signal S2 due to charge losses. Therefore all xenon in the detector is permanently looped at about 5 SLPM[3], through a purification system including a high temperature zirconium getter.

2.2.3 Signal-background discrimination in XENON100

Since the dark matter event rate is expected to be very low, a low background and a high rejection power from WIMP-scattering events is required. In XENON100

[3]Standard Liter Per Minute

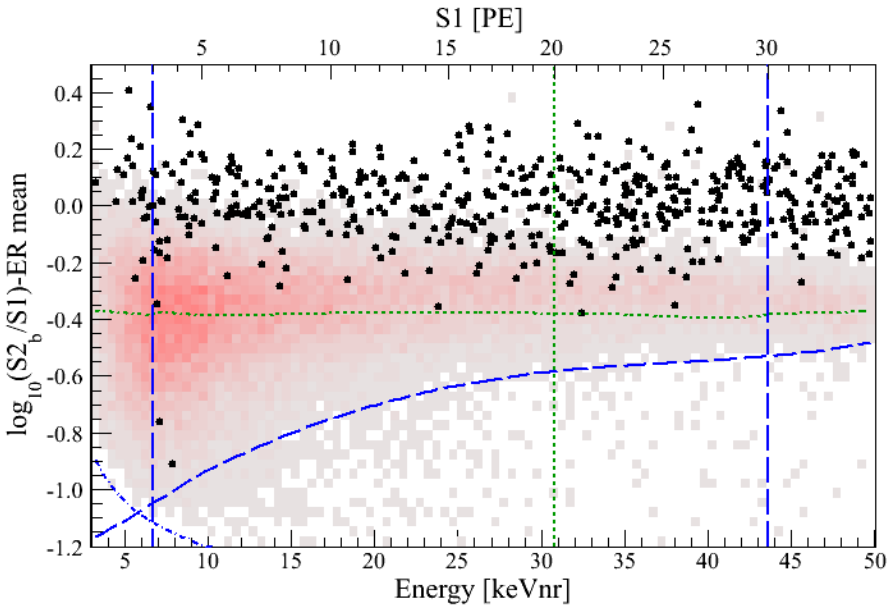

Figure 2.5: Flattened $log_{10}(S2/S1)$ parameter space to discriminate electronic and nuclear recoils [39]. The black points correspond to the measured events in 225 live days of XENON100 after applying all quality criteria (analysis cuts). The distribution of nuclear recoils, measured with an ^{241}AmBe neutron source is given in red. The benchmark WIMP search region is defined to reject 99.75% of electronic recoils (horizontal green dotted line) which are distributed at higher values of $log_{10}(S2/S1)$. Two events have been found in the benchmark region where (1.0±0.2) background events have been expected.

the detected signals have to fulfill various criteria to be accepted as a candidate event. This so-called data cuts contain: data quality cuts, energy selection and threshold cut on S2, selection of single scatter events, selection of the fiducial volume [47]. The remaining events are then used in a Profile Likelihood (PL) analysis. Furthermore, a cut-based analysis is performed to cross check the obtained result. In this approach $log_{10}(S2/S1)$ is additionally used as a discrimination parameter to reject electronic recoil events.
This section gives some introductive information on selected singal-background discrimination methods connected to the following content of this thesis. It is emphasized that it is not aimed to give a description of the complete analysis methods used in XENON100. For a detailed discussion it is referred to [47].

Nuclear and electronic recoil band The ratio of the secondary detector signal S2 (ionization charge) and the primary signal S1 (scintillation light) changes whether the signal originates from nuclear or electronic recoil. A S1 signal produced in the

latter process is usually followed by a much larger S2 than a S1 signal originating from a nuclear recoil of similar energy. This effect, caused by different ionization yields, provides a discrimination parameter for electromagnetic background signals (γ and β background) and nuclear recoil signals (WIMPs and neutrons). γ and neutron calibration data show two event populations as bands in the flattened $log_{10}(S2/S1)$ discrimination parameter space[4]: the electronic recoil band, located at higher values of $log_{10}(S2/S1)$ and the nuclear recoil band respectively.
Figure 2.5 demonstrates the use of this rejection power in the analysis of XENON100 data. The black points correspond to the measured events in 225 live days of XENON100 after applying all data quality criteria (analysis cuts) as they are distributed in the discrimination parameter space. The red event distribution corresponds to nuclear recoils, obtained by calibration with an ^{241}AmBe neutron source. By defining a data cut $C(S1)$, i.e. an event selection criteria, requiring that $log_{10}(S2/S1) > C(S1)$ one can effectively reject electromagnetic background while many nuclear recoil events fulfill this criteria. In figure 2.5 this cut is given by the horizontal green line (dotted), chosen to reject 99.75% of the electronic recoils [39]. The benchmark WIMP search energy region in figure 2.5 is fixed by $(3 < S1 < 20)$ PE (vertical blue dashed line and green dotted line respectively). Using equation 2.1 this corresponds to the energies $(6.6 - 30.5)\,\mathrm{keV}_{nr}$ for XENON100 data published in [39]. The second vertical blue dashed line at 30 PE ($43.3\,\mathrm{keV}_{nr}$) gives the upper energy limit for the PL analysis as used in [39]. The lower border of the benchmark region (horizontal dashed blue line) is given by the 97% quantile of the nuclear recoil distribution while the dashed-dotted blue line corresponds to the S2 energy cut $S2 > 150$ PE to guarantee >99% hardware trigger efficiency. In figure 2.5, two events pass all quality cuts and are located within the benchmark region where (1.0±0.2) background events have been expected. PL analysis and a 26.4% probability for a fluctuation to two background events, however, indicate that there is no dark matter signal.

Fiducial volume cut In the last section the XENON detector has been introduced as a two-phase TPC. Due to this design, detected events can be spatial localized with a resolution of 3 mm [27]. This is achieved by position reconstruction algorithms applied on the PMT hit pattern (x,y-resolution) and due to the different electron drift times depending on the z-coordinate of the scattering position. The knowledge of the event position allows to reject events close to the walls which are mostly induced by radioactive impurities of the detector materials. As shown in figure 2.6 for data analysis a fiducial target mass is defined (red ellipsoid). Background events are accumulated at the edges of the TPC due to the

[4]In XENON100 analysis the log_{10} of the discrimination parameter S2/S1 is used as discrimination parameter. The event distributions of electronic and nuclear recoils, i.e. the recoil bands, are *flattened* by subtracting the electronic recoil band's mean.

selfshielding power of LXe. Events outside the fiducial target mass are rejected by the fiducial volume cut

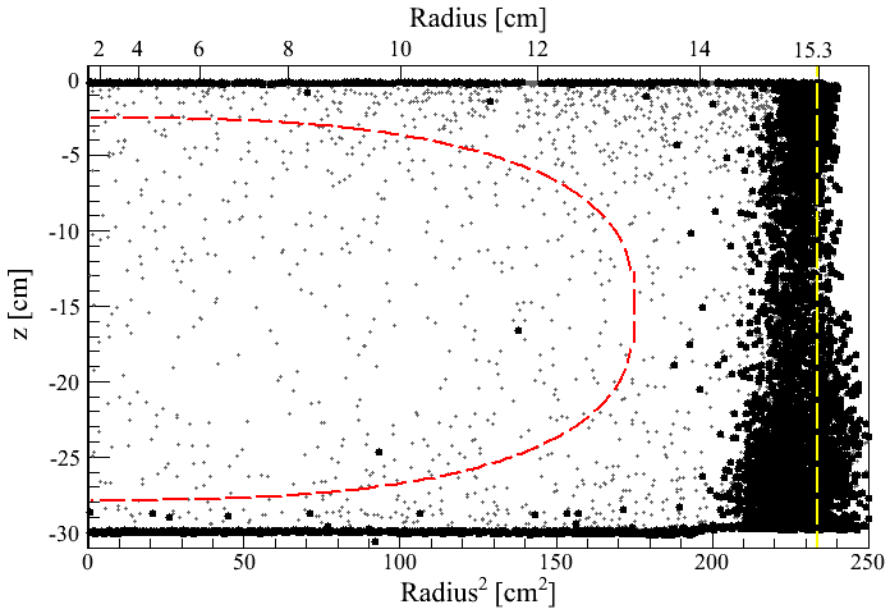

Figure 2.6: The 34 kg fiducial volume (red) with the spatial distribution of detected events in 225 live days (after application of the analysis cuts). The gray points correspond to events which do not fulfill the requirements on the discrimination parameter $log_{10}(S2/S1)$ while the black ones pass this cut. The yellow dashed line marks the border of the TPC. The here plotted data analysis is taken from [39]. Two candidates for nuclear recoil events pass all quality cuts (black points inside the fiducial volume).

Single scatter cut The dark matter interaction cross section is that small that WIMPs are expected to scatter only once inside the target volume. This fact motivates to reject so-called *multiple scatters*, i.e. two or more simultaneous events. Due to the different spatial positions of the single energy depositions, these events are characterized by multiple S2 pulses but only one S1 pulse, since the time difference between the scatters is too small to be resolved in the prompt scintillation light. The *single scatter cut* identifies and rejects events which show multiple S2s.

2.3 XENON1T

Upscaling XENON100 to ton scale, in terms of target mass, has several advantages. Besides the higher total event rate due to the increased target mass, a larger detector is also worthwhile in terms of background minimization. The self-shielding

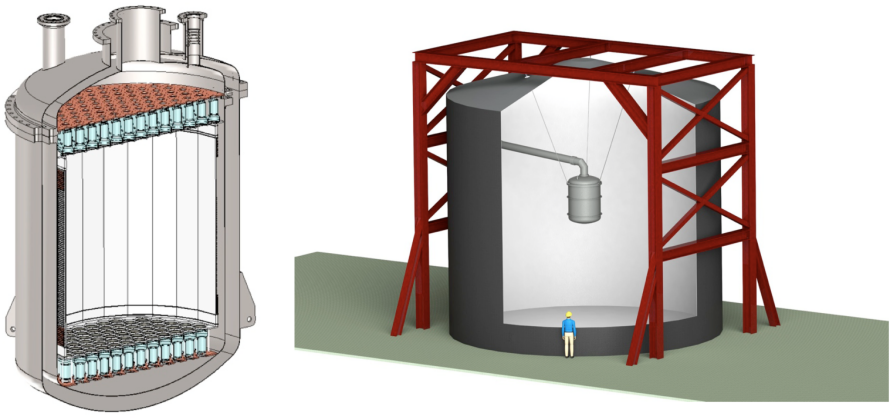

Figure 2.7: (Left) Drawing of the XENON1T cryostat containing the TPC with the PMT arrays and the LXe target. (Right) A water tank used for shielding and as an active Cherenkov muon veto surrounds the cryostat. Figure taken from [48].

property of xenon prevents penetrating radiation from reaching the detector's sensitive core and furthermore the larger target volume allowes a more efficient identification of multiple scatter events which cannot be attributed to WIMPs. The next step in the XENON project, the XENON1T detector [48] [49], will benefit from these effects to reach higher sensitivity for direct WIMP detection. This future detector, currently under construction at the LNGS, is based on the same detection principle as XENON10 and XENON100, but its TPC, $\sim$1 m in hight, will be operated with $>$ 3 t LXe. Approximately 250 PMTs are used for signal detection (see figure 2.7 on the left). One difference in the design, compared to XENON100, is the $\sim$10 m diameter water tank surrounding the cryostat which contains the TPC. Observed by further PMTs, this water tank acts as a shield for neutrons and γ-rays but also as an active Cherenkov muon veto. To achieve the aimed background reduction by a factor 100 compared to XENON100, it is furthermore necessary to remove radioactive contaminations like krypton or radon (see section 3.1.2) from the LXe. Krypton can be removed by distillation of the xenon before it is filled into the detector. In case of radon the aimed radon contamination of $\sim$1 μBq/kg LXe is reached by careful screening and selection of the detector materials but also by a radon removal system which is installed as an additional component of the xenon purification loop (see chapter 4).
The goal of XENON1T is to reach highest sensitivity to detect WIMP dark matter or, in case of the absence of a signal, to set the most stringend limits on the SI WIMP-nucleus cross-section. A sensitivity of $\sigma_{SI} \sim 2 \cdot 10^{-47}\,\mathrm{cm}^2$ for $m_\chi = 50\,\mathrm{GeV/c}^2$ at 90 % confidence level is aimed. Data taking is planed to start in 2015.

Chapter 3

Radon as a source of background in the XENON experiment

One of the most challenging tasks in direct detection dark matter experiments is background reduction and discrimination. Due to the low WIMP-nucleon cross section, scattering events are expected to be extremely rare compared to other events induced by cosmic rays or environmental radiation. Therefore an excellent knowledge of this background sources and their contribution to the overall background rate is necessary. ^{222}Rn turns out to be of particular interest since it permanently emanates from the detector materials and is distributed homogeneously in the whole target material. The investigation of the radon induced background is the main topic of this chapter. In the first section, the two basic background classes, neutron- and electromagnetic-background, are discussed. The spectra of the deposited energies in LXe of the β-decaying ^{222}Rn progenies are simulated with Geant4 [50]. Finally, their individual contribution to the overall radon induced background rate is obtained for a simplified XENON detector geometry.

3.1 Background classification for XENON100

In direct detection dark matter experiments like XENON100, background events are classified by the type of interaction with the target material. WIMPs are supposed to scatter elastically with the xenon nucleus and cause nuclear recoils, as neutrons do. Hence, the *neutron background* is indistinguishable from a dark matter detection signal. *Electromagnetic background* originates from the electromagnetic interaction of gammas or betas with the electrons in the atomic shell of the target material.

3.1.1 Neutron background

Neutrons are the most critical form of background for XENON100. The nuclear recoils caused by them are indistinguishable to those of WIMPs. Therefore, the detector can be calibrated using an ^{241}AmBe neutron source. The estimated total neutron background for the latest published XENON100 result is $\left(0.17^{+0.12}_{-0.07}\right)$ for an exposure of 225 live days $\times$ 34 kg [39].
According to their origin, there are two classes of neutron sources:

Radiogenic neutrons Due to radioactive impurities (^{238}U, ^{232}Th) of the detector and shield materials, neutrons are produced in (α, n) reactions and spontaneous fission. These (α, n) reactions cause most of the neutron background from materials with a low atomic number Z, since its cross-section is inversely proportional to Z. For materials with a high atomic number, e.g. lead, spontaneous fission dominates as a source of neutrons. Once created they can penetrate the detector materials into the LXe target and cause dangerous background.

Cosmogenic neutrons Despite of the $\sim$1.4 km rock overburden of the LNGS laboratory and the resulting reduction of the cosmic muon flux by six orders of magnitude, muons induce about 70% of the neutron background in XENON100 [39]. High energy muons are able to reach the underground lab and produce neutrons in electromagnetic showers. Therefore, the water tank with the Cerenkov muon veto is needed for the XENON1T experimented.

As described in [51] for XENON100, the knowledge of the detectors chemical composition, its radioactive contamination as well as the muon flux in the laboratory with its energetic and angular spectrum, allows the simulation of the neutron production rate. This rate is then used as input for a Monte Carlo simulation to get the final neutron induced background in the detector.

3.1.2 Electromagnetic background

Electromagnetic background events, produced by gammas and electrons, are effectively identified by a different detector response in the ratio of ionization charge (S2 signal) and scintillation light (S1 signal) compared to nuclear recoil events. However, while most of the electromagnetic background events are Gaussian distributed in the discrimination parameter space, some events leak into the nuclear recoil band due to incomplete charge collection and a resulting lower S2 signal (anomalous events). The total electromagnetic background from Gaussian and anomalous events for the latest published XENON100 results, estimated for an exposure of 225 live days $\times$ 34 kg, is (0.79$\pm$0.16) events [39]. Although the elec-

tronic background rejection, as used in the cut-based XENON100 analysis, works at a 99% level (with a mean nuclear recoil acceptance of about 40 % [47]), the remaining electronic recoil events can mimic a WIMP signal.
In XENON100 the electromagnetic background is categorized regarding to its origin:

Radioactive contamination in detector and shield materials

γ-rays from radioactive impurities in the detector and shield materials are usually the dominant contribution to the electromagnetic background. Due to their small penetration depth, electrons from β-decays in the detector materials are only dangerous if they are produced near the surface to the xenon target. The most relevant radioactive impurities for XENON100 are ^{238}U, ^{232}Th, including the noble gases ^{222}Rn and ^{220}Rn and progenies from their decay chains. Furthermore, there is also ^{40}K and ^{60}Co as substantial sources of background. To avoid contamination, most of the detector materials have been screened with highly sensitive germanium detectors before detector construction [52]. This allowed a careful material selection and additionally the screening results can be used as input for Monte Carlo simulations of the electromagnetic background [53].

Intrinsic krypton and radon radioactivity

A big advantage of xenon as a target material is that ^{136}Xe is its only long-lived radioactive isotope. The EXO collaboration reports the observation of the two-neutrino double-beta decay ($2\nu\beta\beta$) of this isotope with a half life of $T_{1/2} = 2.11 \cdot 10^{21}$ yr [54]. For the possible neutrinoless double-beta decay of ^{136}Xe, on the other hand, a lower limit on its half life of $T_{1/2} => 1.6{\cdot}10^{25}$ yr (90% CL) is published, also by the EXO collaboration [55]. Due to this long half lifes, the intrinsic background in XENON100 is basically induced only by the contamination of the LXe target by the radioactive noble gases krypton and radon.

Krypton Commercially available is xenon with a krypton contamination of several ppb[1]. Albeit natural krypton is not dangerous in terms of background, it contains the isotope ^{85}Kr at a level of 10^{-11} [56] , [57]. This man-made beta decaying isotope has an endpoint energy of 687 keV and a half life of 10.8 years. With this properties it is a source of permanent, uniformly distributed background in LXe. Fortunately distillation of the xenon before filling into the detector can reduce the overall krypton level to the ppt[1] level (see section 4.1). For the prediction of the krypton induced internal background its concentration is determined by RGMS measurements, but also by a *delayed coincidence analysis* of the detector

[1]ppb → parts-per-billion (10^{-9}), ppt → parts-per-trillion (10^{-12})

data. ^{85}Kr decays alternatively with a 0.434% propability into ^{85m}Rb (β-decay with 173.4 keV endpoint energy) which then de-excites with a half-life of 1.015 μs by a 514 keV gamma emission. This two energy depositions within a short time window are a unique signature to identify the ^{85}Kr-decay. See [51] and [47] for more details.

Radon ^{222}Rn and its progenies are the second crucial intrinsic source of background. The ^{222}Rn is a daughter isotope of the ^{238}U decay-chain. As a noble gas it easily emanates, once created in the detector materials by ^{226}Ra α-decay, into the LXe. With a half life of 3.8 days it is distributed homogeneously in the liquid xenon [59], [60]. In figure/table 3.1 the radon decay chain and the corresponding half life and decay energies are illustrated. Particularly the background induced by β-events is crucial (see following section 3.2.2). α-decays are in general rather harmless since they typically have energies > 5 MeV; far too high to mimic a dark matter signal. With a half life of 22.3 years the radon daughter ^{210}Pb lives finally long enough, compared to the detectors live time, that its decay and all subsequent progenies are insignificant.
^{220}Rn from the ^{232}Th decay chain is a possible background source as well. However, due to its rather short half-life of 55.6 s it turned out to be subdominant since it does not live long enough to distribute all over the LXe target. The radon contamination of the liquid xenon can be obtained by a *delayed coincidence analysis* of the radon daughters ^{214}Bi and ^{214}Po but alternatively by assigning detected α-events to ^{222}Rn or ^{218}Po decays. With this methods a radon contamination of 63 μBq/kg has been obtained for the latest published XENON100 data [39]. A detailed description can be found in [60]. The results of this analysis is then used as input for a Monte Carlo simulation of the radon background [51].
Since radon is the central topic of this thesis a more detailed discussion of the radon induced background is given in the following section. There is no established method for purifying xenon continuously from this noble gas yet. Possible solutions for XENON1T are discussed in chapter 4.

3.2 Prediction of the radon induced background rate

As discussed in the previous section 3.1.2, radon is a crucial background source for detectors like XENON100. It permanently emanates from the detector materials and has a half-life long enough to distribute homogeneously in the xenon target. Hence the *fiducial volume cut* (see section 2.2.3) has no effect in reducing the event concentration. Moreover, in contrast to krypton, there is no radon removal system reported yet which permanently filters radon from LXe. However, a good detector understanding allowes to monitor the radon contamination and finally to simulate

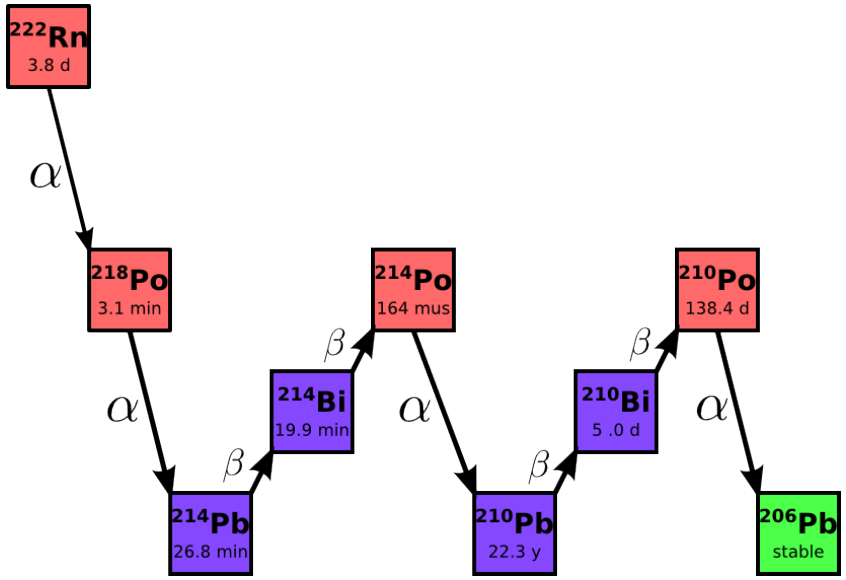

isotope	half life	α-decay energy [MeV]	β-decay energy [MeV] (intensity [%])	γ-emission energy [keV] (intensity [%])
^{222}Rn	3.8 d	5.490	-	-
^{218}Po	3.1 min	6.002	-	-
^{214}Pb	26.8 min	-	0.728 (42.2) 0.670 (48.9) 0.185 (2.8) 1.030 (6.3)[a]	352 (35.1) 295 (15.1) 242 (7.1)
^{214}Bi	19.9 min	-	3.275 (18.2)[a] 1.542 (17.8) 1.508 (17.0) 1.425 (8.2) 1.894 (7.4)	609 (44.6) 1764 (15.1) 1120 (14.7) 1238 (5.8) 2204 (5.0)
^{214}Po	164.3 μs	7.687	-	-
^{210}Pb	22.3 yr	-	0.017 (80) 0.063 (20)[a]	47 (4.3)
^{210}Bi	5.0 d	-	1.162 (99)[a]	-
^{210}Po	138.4 d	5.304	-	-
^{206}Pb	**stable**			

Figure 3.1: Decay energies and γ-emission of ^{222}Rn and its progenies. All numbers are taken from [58] but simplified in terms of subdominant isotope branches.

[a] β-decay Q-value

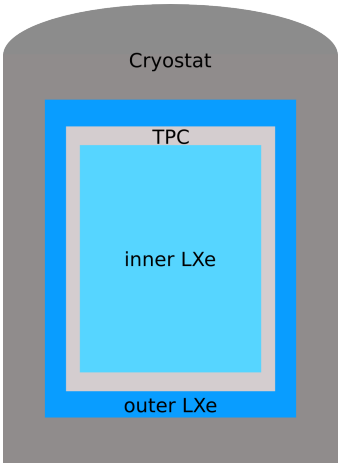

Figure 3.2: Schematic drawing of the simulated detector using the Geant4 toolkit. The TPC (light gray) contains the 2.2 t inner LXe used as target. An additional LXe layer and the cryostat enclose the TPC.

the radon induced background rate.
In this section the energy spectra of the energy deposits of ^{222}Rn and its progenies in liquid xenon is simulated in a simplified detector geometry with respect to the XENON1T detector. After a discussion of the shape of the energy spectra of the radon progenies, their contribution to the total radon induced background rate is analyzed. By defining a *single scatter cut* on the simulations output, its impact on the total background rate is investigated.

3.2.1 Energy spectra of β-decaying radon progenies

Due to their high energies, α-decays usually do not contribute to the low energy background relevant for dark matter search. This discussion is restricted to simulations of the energy spectra of events, detected within a LXe target, which are originating from β-decaying radon progenies. As illustrated in figure/table 3.1 the ^{222}Rn-chain includes four β-decaying isotopes: ^{214}Pb, ^{214}Bi, ^{210}Pb and ^{210}Bi. A simplified XENON detector has been coded in Geant4 for carring out the simulations. Its TPC, made out of teflon, contains the 2.2 t LXe target (orientated by XENON1T) and is surrounded by an additional LXe layer which is again enclosed by a cryostat (see figure 3.2. The inner structure of the TPC, including the PMTs, has not been simulated.
To obtain the spectra of the deposited energy of the β-decaying radon progenies, in the simulation ^{222}Rn is distributed homogeneously in the LXe target. The decay chain of radon to the stable ^{206}Pb isotope is then simulated by Geant4 and information on every single energy deposit (energy, spatial coordinates, mother isotope) is recorded.

Figures 3.4 and 3.3 are the results of the Monte-Carlo simulation of 100 000 decays from ^{222}Rn to ^{206}Pb. With exception of ^{210}Bi, none of the other isotopes

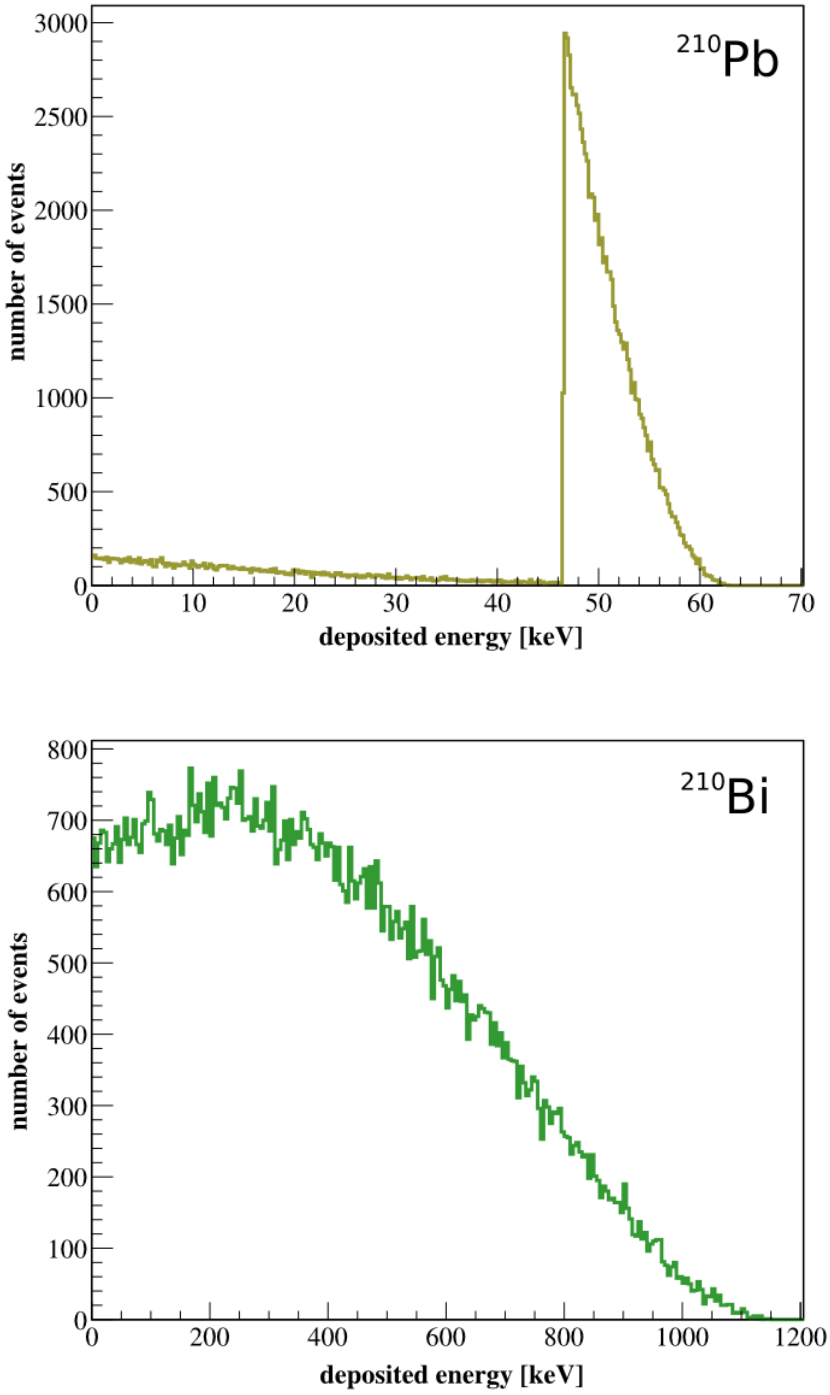

Figure 3.3: The simulated energy spectra from ^{210}Pb (top) and ^{210}Bi (bottom) β-decay in liquid xenon. While latter shows a pure β-spectrum, ^{210}Pb has a peak at 46.5 keV.

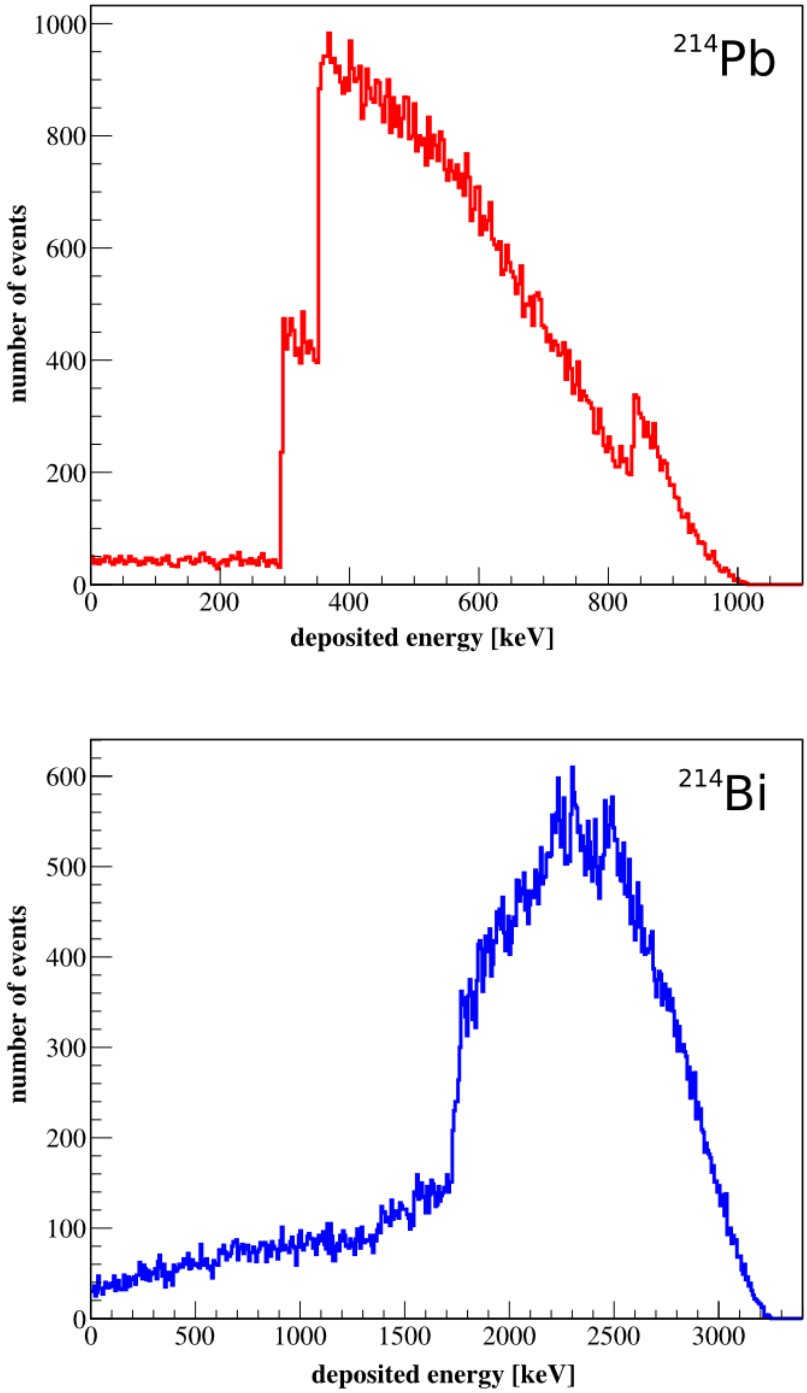

Figure 3.4: The simulated energy spectra from ^{214}Pb (top) and ^{214}Bi (bottom) β-decay in liquid xenon. The pure β-spectrum is overlaid by peaks which are the result of β-decays via excited states of the daughter isotope.

shows a pure β-spectrum. In case of ^{210}Pb, the β-spectrum at low energies is overlaid with a peak at 46.5 keV. As noted in table 3.1, ^{210}Pb disintegrates via β-decay to the ground state but more likely (80%) to an excited level of ^{210}Bi (46.5 keV). These events are responsible for the obtained peak, while the direct decay to the ground state gives the underlaying spectrum. The de-excitation occurs mostly due to internal conversion, in some cases by γ-emission (4.3%). The rather small energy of the excited state is almost always completely deposited in the LXe, which explains the vertical rise of the peak. The time scale of this process is within fractions of a ns [58] and therefore too short to be resolved in the detector. The shape from the peak maximum to the end-point energy, on the other hand, is due to the preceding β-decay to the excited ^{210}Bi state.
^{214}Pb and ^{214}Bi decay via excited states as well. In case of lead, those with level energies of 295 keV, 352 keV and 839 keV are the most frequent ones and responsible for the observed peaks in the spectrum (figure 3.3). The bismuth decay, finally, happens via numerous excited ^{214}Po states [58]. Apart from the ground state, energy levels of 1764 keV, 2204 keV and 2448 keV can be identified. The de-excitation happens via internal conversion and γ-emission (table 3.1).

3.2.2 Radon induced background rate

The simulation of the energy spectra can be used to predict the background rate and background spectrum attributed to the single ^{222}Rn-progenies in the LXe target. A ^{222}Rn contamination of 60 μBq/kg, similar to XENON100 [60], is assumed, altough for XENON1T a radon concentration of approximately 1 μBq/kg is aimed. As reported in [53] the induced background rate varies linearly with the radon concentration. Assuming further a homogeneous distribution within the LXe for the radon and its progenies and furthermore secular equilibrium for the whole decay chain (i.e. same activity for every isotope), the deposited energies in a predefined fiducial volume is recorded in the running simulation. Figure 3.5 illustrates the obtained result for energies <1 MeV. In the crucial low energy region, clearly the background induced by ^{210}Pb and ^{210}Bi dominates. Then, at higher energies, ^{214}Pb becomes more significant due to the 295 and 352 keV peaks in its energy spectrum. However, the assumption of a secular equilibrium is not justified. Due to its long half-life, the equilibrium for ^{210}Pb, and consequently also for ^{210}Bi, is not reached in the operation time of XENON100. Hence, for the total radon induced background rate these two isotopes can be neglected. This assumption is also motivated by data [53] due to the absence of the perfidious 47 keV peak of the ^{210}Pb decay. The other two radon daughters sum up to the background rate given in figure 3.6 (solid red line) for the assumed radon contamination of 60 μBq/kg. From comparison of figure 3.5 with figure 3.6 ^{214}Pb turns outs to be the dominating component of the overall radon induced background.

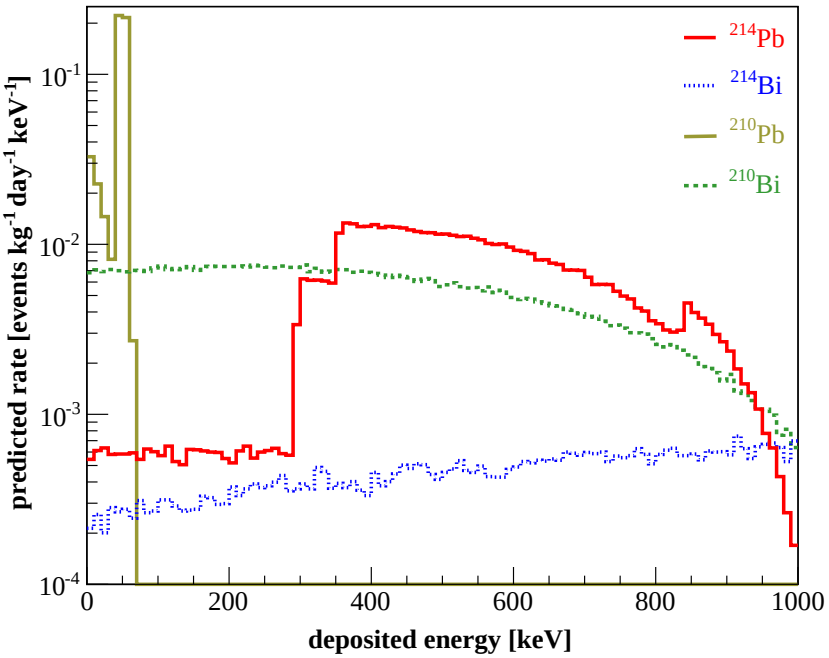

Figure 3.5: Background rate induced by the single β-decaying radon progenies assuming an activity of 60 μBq/kg for each isotope.

As a further step a *single scatter cut* is applied on the obtained result to estimate its rejection power. Since the cut, as used in the XENON100 analysis, is defined on the actual detector output S2 (see section 2.2.3), the here produced data requires a *simulated* single scatter cut. This can be achieved by summing up the energy deposits of a single radioactive decay within a radius of 3 mm, corresponding to the assumed spatial resolution power of the detector. This cluster of deposits is then considered as one event. If several clusters, i.e. events, are found for one single β-decay, they are identified as a multiple scatter event and rejected. The dashed blue line in figure 3.6 illustrates the effect of this single scatter cut on the simulated data. As expected, in the low energy region hardly any events are rejected since the energy deposits are very localized (within the 3 mm resolution). The rate simulated for a contamination of 60 μBq/kg is $9 \cdot 10^{-4}$ events$\cdot$ kg$^{-1}\cdot$ day$^{-1}\cdot$ keV^{-1} in the low energy range. β-decays via excited states are more often identified as multiple scatters due to the following de-excitation by γ-emission. Hence the distinct peaks of the ^{214}Pb decay are suppressed but still present.

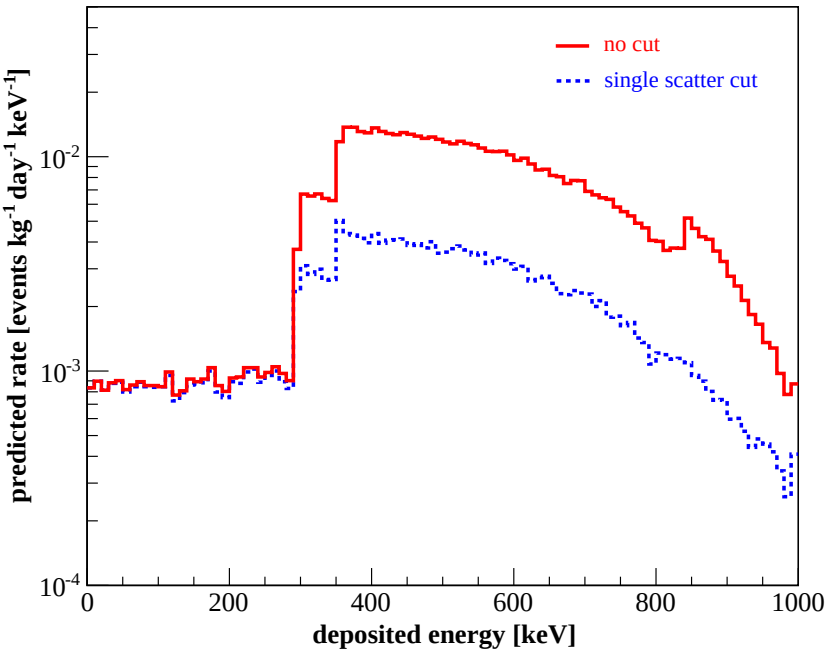

Figure 3.6: Predicted radon induced background rate before (solid red line) and after applying a *single scatter cut* (blue dashed line) assuming an activity of 60 μBq/kg. The shape of the curve identifies ^{214}Pb as the dominating source of radon induced background.

In summary, ^{214}Pb turns out to be the most crucial radon daughter in terms of background in the energy region relevant for dark matter search. The α-decays in the radon chain are with more than 5 MeV too high energetic to contribute to the low energy background and the isotopes ^{210}Pb and ^{210}Bi can be neglected due to the long half-life of lead. The ^{214}Bi isotope, on the other hand, has a very short half-life and its decay is immediately followed by the high energetic ^{214}Po α-decay. Due to this signature a rejection of more than 50% of the ^{214}Bi induced events is achieved.
Although sophisticated analysis methods enable a high signal/background discrimination, radon has the potential to be one of the limiting factors on the sensitivity of future projects like XENON1T. A careful selection of the detector materials, but also the development of a radon removal system are strategies to counter this problem.

Chapter 4

Adsorbent characterization for a radon removal system in XENON1T

Having identified radon as a crucial background component in dark matter detectors like XENON100 one has to think about removal strategies for future experiments. A system based on adsorption seems very promising. This chapter starts with a short overview on the principles of adsorption in general and adsorbents commercially available. After an introduction to the basic theory of adsorption, an experimental setup to characterize materials on their capability to adsorb radon in presence of other gases is presented. This setup is finally used to carry out adsorption measurements with three different activated carbon samples aiming for extracting important features to select the best performing adsorbent for a future adsorption-based radon removal system for XENON1T.

4.1 Motivation

As pointed out in section 2.3 the upscaling of XENON100 to the ton scale yields several advantages which motivate the XENON1T experiment as a next step in the XENON project. In chapter 3, however, it was shown that beside the external background, the intrinsic background due to radon and krypton plays an important role. While an increasing volume-to-surface-ratio causes a further reduction of the external background, the intrinsic background stays almost constant. Hence it has the potential to be a crucial limiting factor on the experiments sensitivity.
Due to their similar chemical properties it is rather difficult to separate radon and xenon from each other. Well established techniques are separation by adsorption and distillation which are both commonly used in industrial processes and low background experiments. While distillation is based on the different boiling points of the single noble gas components, separation by adsorption is based on the

	He	Ne	Ar	Kr	Xe	Rn
mass number	2	10	18	36	54	86
boiling point (1 atm) $[K]$	4	27	87	120	165	211
Van-der-Waals radius $[pm]$	140	154	188	202	216	220
polarizability $[\text{Å}^3]$	0.2	0.4	1.6	2.5	4.0	5.3

Table 4.1: Comparison of selected properties of different noble gases [61] [62].

different van-der-Waals radii and polarizabilities as will be discussed later in more detail. Table 4.1 gives an overview on some for separation important features of noble gases. Both techniques in principle can be used to fight effectively the krypton and radon contamination in xenon to gain higher sensitivity.

Krypton removal To reduce the krypton contamination of commercial available xenon to the sub ppt level required to guarantee a low background rate (see also 3.1.2), purification by distillation achieves convincing results. Cryogenic distillation columns are already used by the XMASS [63] and XENON [27] collaborations. XMASS reported e.g. a krypton level of 3.3 ± 1.1 ppt after processing a sample of 100 kg xenon gas with a collection efficiency of 99% [63]. The xenon can be processed right before it is filled into the detector and stays clean due to the absence of any natural krypton sources. Since this technique is well established it will also be used for the next generations detectors.
Krypton-xenon separation based on adsorption, however, has been studied as well. As reported in [64], 25 kg xenon have been purified by chromatography with a 10 kg charcoal adsorption column, reaching a krypton level of <3 ppt.

Radon removal In case of radon, the situation is more complex since it is continuously brought into the detector by emanation from the detector materials. This requires, in contrast to krypton, an online radon removal system. The basic idea for XENON1T is to operate a removal system in series to the regular gas purification system as illustrated in figure 4.1. Since also the high temperature zirconium getters, used to purify xenon from electro-negative impurities, are radon sources, the radon removal system must be mounted behind the getter in the purification cycle. This obviously sets great demands on purity of the radon removal system itself. Another important aspect is the circulation velocity of the xenon in the purification loop. To gain a reduction effect on radon, the loop velocity needs to be fast enough to exchange the liquid xenon in the detector before the

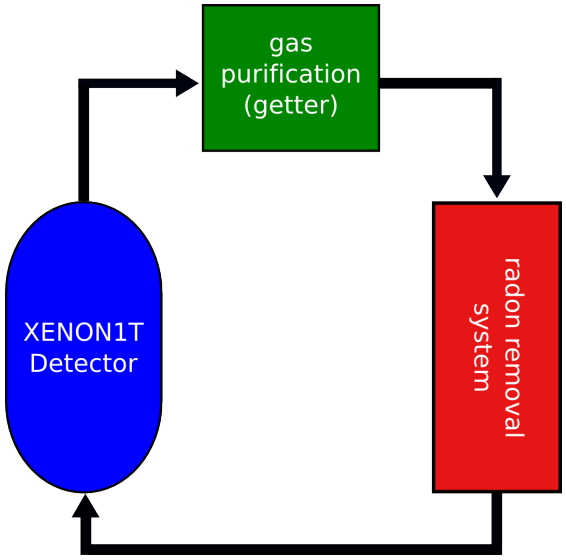

Figure 4.1: A schematic of the gas purification loop in XENON1T. The radon removal system needs to be operated after the electro-negative purification since the getters are a radon source as well. This demands high requirements on purity.

radon decays inside the sensitive volume. Thus, handling gaseous xenon flows of up to 100 SLPM[1] is another criteria the gas purification system, including radon removal, has to fulfill.
In principle again both methods, distillation and adsorption, are possible radon removal techniques. One can think of a distillation system similar to the krypton column but with changed places. In this case the impurity radon has with 211 K a higher boiling point than xenon (table 4.1). An distillation-based radon separation, however, has not been reported so far while adsorption is a commonly used method.

Adsorption-based radon removal Gas separation with adsorbents like activated carbons, molecular sieves, etc. is very well established and easily to handle. Moreover, in contrast to distillation, an adsorption-based, continually radon removal system has been published by the XMASS collaboration in [24].
The idea is to place a cooled trap filled with an adsorbent as the removal system in figure 4.1 and circulating the xenon in the purification loop. The adsorbent has to be selected carefully so that on the one hand radon is bond strongly on the adsorbents surface while on the other hand the adsorption of xenon has to be rather poor. As a result xenon gas flows with low resistance through the adsorbent, while the radon component needs under convenient circumstances days to pass the trap. With a residence period of order of 15 days as reported in [24], the radon most likely decays in the adsorbent trap where it cannot produce any background.
Clearly the performance strongly depends on the amount of adsorbent used and finally on its capacity to particularly adsorb radon altough xenon is much more

[1]Standard Liter Per Minute

abundant. Due to the similarities of those two noble gases it is quite challenging to find a material which adsorbs radon much more efficiently than xenon. Hence it is essential to analyze and select the adsorbent very carefully to take advantage of differences in parameters like the atoms size or polarizability, which of their part have a crucial impact on the adsorption properties.

4.2 Overview on the principles of adsorption

The experimental setup discussed at the end of this chapter aims to characterize adsorbents on their applicability in an adsorption-based radon removal system for XENON1T or other noble gas detectors. Therefore it is appropriate to give initially a short overview on the basics of adsorption and and a description of various adsorbents.
After defining the terminology used in this work and in literature, the adsorption process is discussed in more detail. Here an important adsorption-quality parameter, the *heat of adsorption* is introduced. Basically all adsorption properties of a porous adsorbent can be extracted from *adsorption isotherms*. They are discussed in case of single component in the last part of this section on adsorption principles. For more information on the process of adsorption but also on various application in industry and science it should be referred to [66], [67], [61] and [65].

4.2.1 Terminology of adsorption

Generally *adsorption* means the accumulation of gases or liquids at the surface of a solid. This solid is called *adsorbent* and is ideally highly *porous*, i.e. it has *pores* which make its total surface very large. The total *surface area* is understood as the surface, including the pores, accessibly for the gas or fluid from outside. This area is measured by a given well defined method. Depending on the internal width of the pores they are classified in *micro-, meso-* and *macropores*. For the *pore volume*, however, the volume of all kind of pores, determined by a well defined method is summed up. The gas or liquid in this system is called *adsorbate* when it is in the adsorbed state, but *adsorptive* as long as it is not bound on the adsorbents surface. Further one distinguishes between *chemisorption* and *physisorption*. In the first case adsorption results from chemical bonding between the adsorbate and the surface molecules of the adsorbent. The latter, in contrast, happens with no chemical bonding involved but rather weak intermolecular forces as discussed later. The bonding energy for physisorption is therefore smaller than in case of chemisorption, which is usually more than 40 kJ/mol [68] in the latter case. In this work only physisorption is considered since noble gases do not show chemisorption. For a compact and figuratively introduction of terminology see figure/table 4.1.

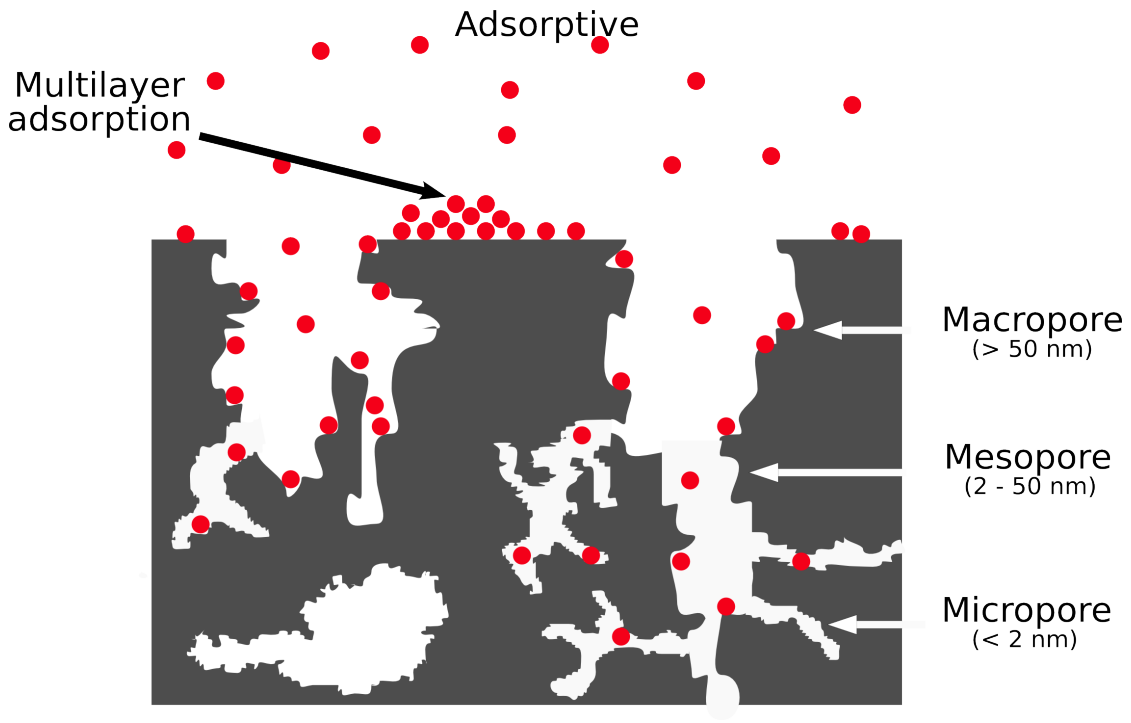

Term	Definition
Adsorbate	substance in the adsorbed state
Adsorbent	solid material on which adsorption occurs
Adsorption	accumulation of one or more components in an interfacial layer
Adsorptive	adsorbable substance in the fluid phase
Chemisorption	adsorption involving chemical bonding
Macropore	pore of internal width greater than 50 nm
Mesopore	pore of internal width between 2 and 50 nm
Micropore	pore of internal width less than 2 nm
Monolayer capacity	physisorbed amount required to cover surface
Physisorption	adsorption without chemical bonding
Pore volume	volume of pores determined by stated method
Porosity	ratio of total pore volume to apparent volume of adsorbent
Porous solid	solid with cavities/channels deeper than wide
Surface area	extent of available surface as determined by a given method
Surface coverage	ratio of amount of adsorbed substance to monolayer capacity

Table 4.2: Terminology of adsorption used in literature and this work (table assembled from [65]).

4.2.2 Description of a selection of adsorbents

In principle adsorption happens on every solid surface. Therefore materials with high porosity are of particular interest. Altough in the later presented measurements only activated carbon are used as samples some other commonly used adsorbents should be introduced here.

Silica gel

Silica gel is an amorphous adsorbent particularly used for drying. Its surface is formed by Si-OH silanol groups having a permanent polarization. As a result silica gel has a high capability to filter other polar molecules like water from mixtures. Nevertheless this bond is rather weak making regeneration by heating at relatively low temperatures of $\sim 150\,^{\circ}\mathrm{C}$ possible. The pore structure can be influenced by the preparation methods but characteristically shows a strongly peaked pore distribution at a desired pore size. While also many other adsorbents are applied for various drying processes, at low temperature and moderate pressures silica gel is often favored, showing here a particular high capacity for water adsorption.

Zeolites

Zeolites are aluminosilicates minerals with high porosity due to their crystal lattice. The framework discriminates different types of zeolites, but all of them are composed by a primary unit formed by SiO_4 and AlO_4. These primary units are again joined together in various polyhedral secondary structural units which finally build up the zeolite crystallin lattice. Figure 4.2 shows three sketches of possible zeolite frameworks. Every vertex represents a Si or Al atoms linked by oxygen bridges. Since the pores are constrained by the crystal lattice, they are precisely uniform as well. Zeolites show no pore-size distribution in contrast to other adsorbents. The framework sets the pore width, allowing to classify different types like *type A, X* or *type RHO* zeolites. It also has a large influence on the adsorption properties since only molecules small enough to reach the inner cavity can be adsorbed effectively. Hence the name *molecular sieve*. The ratio of Si/Al in the lattice is not fixed. In some cases the aluminum can be completely replaced by further silicon with strong impact on the adsorption behavior. The less aluminum in the lattice structure, the more hydrophobic the zeolite adsorbent. Every aluminum atom in the framework introduces a negative charge. Therefore cations are necessary for balance. The type of cations can be varied with additional influence on the adsorption properties. By manipulation of all these parameters, lattice structure, Si/Al ratio and cation types one can reach a range for the pore with of 3 to 10 Å. Alltogether about 40 natural zeolites are known and approximately another 150 types have been synthesized. In [67] one can find a composition of some major

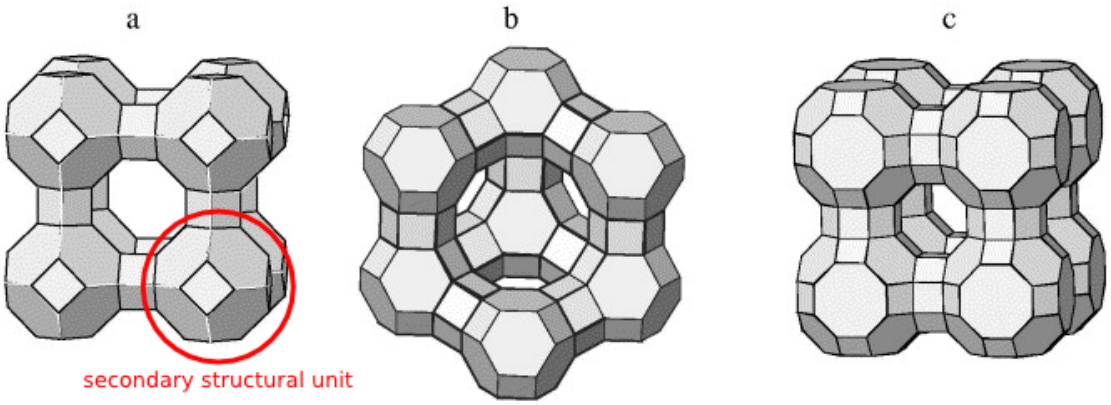

Figure 4.2: Sketch of zeolite structures [70]: (a) zeolite A with highlighted secondary structure unit, (b) X zeolite (and Y zeolite), (c) RHO zeolite. Depending on the composition of the final zeolite framework, the pore width, constrained by the lattice, varies.

synthetic zeolite adsorbents. Due to this flexibility they can be designed for many applications in science and technology [69].

Activated carbon

The term *activated carbon* or *charcoal* is used for highly porous adsorbents produced from carbon rich materials like wood, coconut shell, coal etc., but also synthetic polymers. In the manufacture, this raw materials undergo an *activation process* [71] which increases the primary pore volume and surface area. This manufacturing process has therefore a big influence on the charcoals adsorption properties. The higher the grade of activation, the larger is especially the micropore volume and surface area. Activated carbon may have a particularly large surface area up to $2\,500\,\mathrm{m}^2/\mathrm{g}$.
As sketched in figure 4.3 the structure is figuratively a clew of imperfect aromatic sheets of graphen, randomly connected with each other. This system of partially splitted layers form the complex system of often slit shaped pores.
Another unique, and for many applications useful feature of activated carbon is its, in general, nonpolar surface. This allows a much more efficient adsorption of nonpolar molecules while in case of silica gel, for instance, those with polar momentum are preferred.
All radon adsorption measurements in this work use activated carbon as adsorbent. Its large surface area and microporevolume but also its pore distribution are very promising. The rather large macro- and mesopores can act as transport tubes to the micropores where finally adsorption takes place. In the slit shaped pores the intermolecular forces can act from two pore walls, binding the radon atom, larger

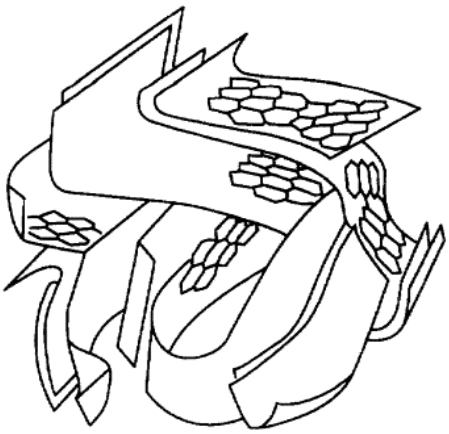

Figure 4.3: Structure of an activated carbon [73]. Imperfect graphite layers form the often slit shaped pores.

in size than xenon, more strongly [72].

4.2.3 Physical adsorption forces and the heat of adsorption

Physisorption is caused by two types of molecular interaction:

- *van-der-Waals forces* from instantaneously induced dipole-dipole and higher multipolar interaction
- *Induction forces* caused by a permanent electric field of the adsorbent material (polar surface)

The final attractive potential for the adsorptive would be a sum of all contributions of those two interactions. In case of adsorption of rare gases on activated carbon, however, in good approximation no permanent electric field is involved. In this simplest case, the potential has only the typical $\propto r^{-6}$ dispersion (van der Waals) term and a short range repulsive term $\propto r^{-12}$ due to the finite size of the molecules. The result for the interaction of one adsorbent-adsorptive molecule pair as a function of theire distance r is of the form of the well known *Lennard-Jones* potential[2]

$$\phi(r) = -\frac{A}{r^6} + \frac{B}{r^{12}}\,. \tag{4.1}$$

While B can be calculated theoretically, A is a semi-empirical constant which can be estimated by considering properties like polarizability or susceptibility of the involved molecules. By summing up the interactions with all adsorbent molecules (surface layer, but also those underneath) one gets an expression for the total potential ϕ for every adsorptive particle. The minimum of this potential is now a

[2]Usually written with constants $4\epsilon\sigma^6$ and $4\epsilon\sigma^{12}$.

measure for the binding energy, i.e. the energy released when a particle gets adsorbed. Adsorption is an exothermic process. Hence one introduces the *isosteric*[3] *heat of adsorption* q as a quantity for the bonding strength.
The proper thermodynamically definition of the isosteric heat of adsorption is given by the difference between the molar enthalpy of the adsorptive and the partial molar enthalpy of the adsorbed material (see [74] and [75]). Nevertheless, following the work of [66] one can show, that except at very high temperatures, $q_i \approx \phi_{min}$ is a quite reasonable approximation for adsorption at low coverage. In the book of O. Ross [61] this approach is used to estimate the heat of adsorption of various noble gases by calculating ϕ_{min} and compares it with experimental data.

4.2.4 Single-component adsorption isotherms

For this work, a system of a solid adsorbent and gaseous adsorbate bond only by physisorption is assumed. The amount of gas adsorbed in an equilibrium can be described phenomenologically by a function

$$ad = ad\ (p,\ T)\ . \tag{4.2}$$

The adsorption capacity decreases with increasing temperature due to the higher kinetic energy of the adsorbed atoms. At some point, when the kinetic energy of the gas is large compared to its heat of adsorption, one can assume that no adsorption takes place. Hence baking can be used to force desorption of the bonded gas and to regenerate the adsorbent.
At a fixed temperature, equation 4.2 becomes the adsorption isotherm of the adsorbent-gas system. From the behavior of adsorption with varying pressure most of an adsorbents properties like surface area, pore volume and even the pore-size distribution can be extracted. A classification recommended by the IUPAC[4] identifies 6 types of physisorption isotherms as shown in figure 4.4. Each of them is typical for particular adsorbents or adsorbates. Type I is the most frequent in adsorption processes and describes the data found in this work as well. Then, isotherm models used in this work for data analysis are introduced. An overview about isotherm models is given in [77].

Langmuir isotherm and Henry's constant

A simple theoretical model for Type I isotherms was introduced by Langmuir [78]. Altough it contains the following simplifications it is still used successfully in many applications.

[3] Processes keeping the coverage of the adsorbent constant are called *isosteric*.
[4] International Union of Pure and Applied Chemistry

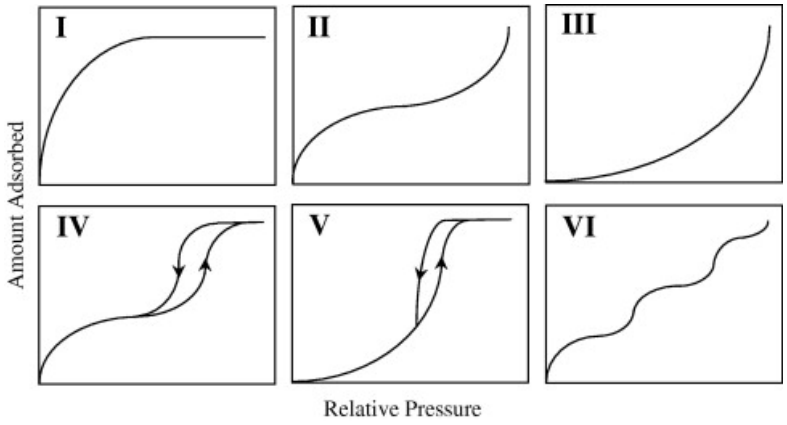

Figure 4.4: IUPAC[4] isotherm classification [76].

- every *site* on the adsorbents surface is unambiguously localized and can hold one and only one adsorbate atom or molecule → monolayer-adsorption
- every *site* is energetically equal
- adsorbed atoms or molecules do not interact with the occupied neighbor-sites

Using this assumptions, the well-known *Langmuir isotherm* for the amount of adsorbed gas n_{ad} in *mol* as a function of adsorption-pressure p can be derived:

$$n_{ad}(p) = \frac{n_\infty \, K_L \, p}{1 + K_L \, p} \tag{4.3}$$

Where n_∞ is the *monolayer capacity*, i.e. the total number of sites in the Langmuir model. For Type I isotherms (figure 4.4), n_∞ is the limit for $p \to \infty$ and its value can change depending on the adsorptive. Hence n_∞ can be used as a quality parameter for adsorption of a particular adsorptive. K_L is the *Langmuir constant* which also varies with the adsorptive.

In the low pressure limit $p \to 0$, the Langmuir isotherm 4.3 reduces to

$$n_{ad}(p) = \underbrace{n_\infty \, K_L}_{H} \, p = H \, p \tag{4.4}$$

which is known as the *Henry's isotherm*. It points out the experimentally observed linear behavior of the isotherms in the low pressure region. The Henry's coefficient H has the dimension [mol/Pa] which reflects the adsorbent capability for a particular adsorptive.

Freundlich isotherm

The *Freundlich isotherm* is an empirical isotherm proposed by Freundlich [79]:

$$n_{ad}(p) = K_F \, p^{\frac{1}{m}} \, . \tag{4.5}$$

K_F is the model constant analogous to the Langmuir constant and m is the so-called *Freundlich parameter*. Both are dependent on temperature and the adsorptive. Initially this model was developed to describe the adsorption of solutions, nevertheless it can be applied on adsorption isotherms of gases as well.

Sips isotherm

The Langmuir and Freundlich isotherms can be combined to the *Sips isotherm* [80] (also: *Langmuir-Freundlich isotherm*):

$$n_{ad}(p) = \frac{n_\infty \, K_S \, p^{\frac{1}{m}}}{1 + K_S \, p^{\frac{1}{m}}} \, . \tag{4.6}$$

K_S is the model constant and m the Freundlich parameter. In contrast to the Freundlich model, the Sips isotherm has Henry's equation 4.4 as a low pressure limit. n_∞ is the saturation value for monolayer adsorption.

Tóth isotherm

The *Tóth isotherm* [77] is another model commonly applied on monolayer adsorption isotherms:

$$n_{ad}(p) = \frac{n_\infty \, p}{\left(\frac{1}{K_T} + p^t\right)} \, . \tag{4.7}$$

Monolayer capacity n_∞, model constant K_T and Tóth parameter t are analogous to the previous models. The Tóth isotherm also reduces to Henry's equation for $p \to 0$ and it simplifies to the Langmuir isotherm for $t = 1$.

4.3 Radon and xenon adsorption measurements

The purpose of this work is to characterize and compare different adsorbent materials based on their ability to adsorb radon. Therefore, several measurements of radon adsorption have been carried at different temperatures, adsorption pressures and adsorption times (i.e. the time the radon was in contact with the adsorbant). As a sample, radon-helium mixtures but also radon-xenon mixtures have been used. Regarding to its abundance in the mixture, radon plays a very subdominant

volume	*radon sample*	*center volume*	*adsorbent volume*	*Lucas-Cell*
[ml]	59.0 ± 1.0	16.0 ± 0.3	8.1 ± 0.2	210 ± 1

Table 4.3: The setups volumes as introduced in figure 4.5 in ml.

role. The low radon concentration ensures that its adsorption can be described by the simple Henry's law which is the low-pressure limit of several adsorption models.
Since helium, in good approximation, is not adsorbed at all, the results obtained with radon-helium mixtures can be considered as single-component adsorption measurements of radon. In contrast to helium, xenon was found to have a large influence on the uptake of radon (see section 4.5.3).

In this section the experimental setup is introduced with a detailed description of the Lucas-Cell as an α-particle detector. Then the measurement procedure at room temperature is described in section 4.3.2. The modifications required for adsorption measurements at other temperatures are explained in 4.3.3. Since it turned out that humidity influences the results for adsorption, the radon sample needs some preparation in advance which is described in section 4.3.4.

4.3.1 Experimental Setup

The experimental setup to determine the static adsorption of radon on any adsorbent is shown in figure 4.5. The basic elements are a volume to store the radon sample (*radon sample* in figure 4.5) which is at the right top of the apparatus separated from the rest by a valve and the volume containing the adsorbant, *activated carbon*, at the bottom of the setup. The *center volume* is the connecting volume and is used to portion the activity of the radon sample. Up to five adsorption measurements can be done with one sample. A pressure gauge (P) in the *center volume* and a Lucas-Cell (see below) act as detectors for pressure and radon activity, respectively. Since for a xenon-radon mixture the total pressure is basically the xenon partial pressure alone, one obtains the xenon adsorption by measuring the change in pressure, while the radon adsorption is gained by the loss of α-activity due to adsorption. This is measured by the Lucas-Cell. Pumping is possible at the *center volume* and the Lucas-Cell.
The sizes of the introduced volumes have been determined for later analysis and can be found in table 4.3.1. This experimental setup has been introduced for the first time by [81].

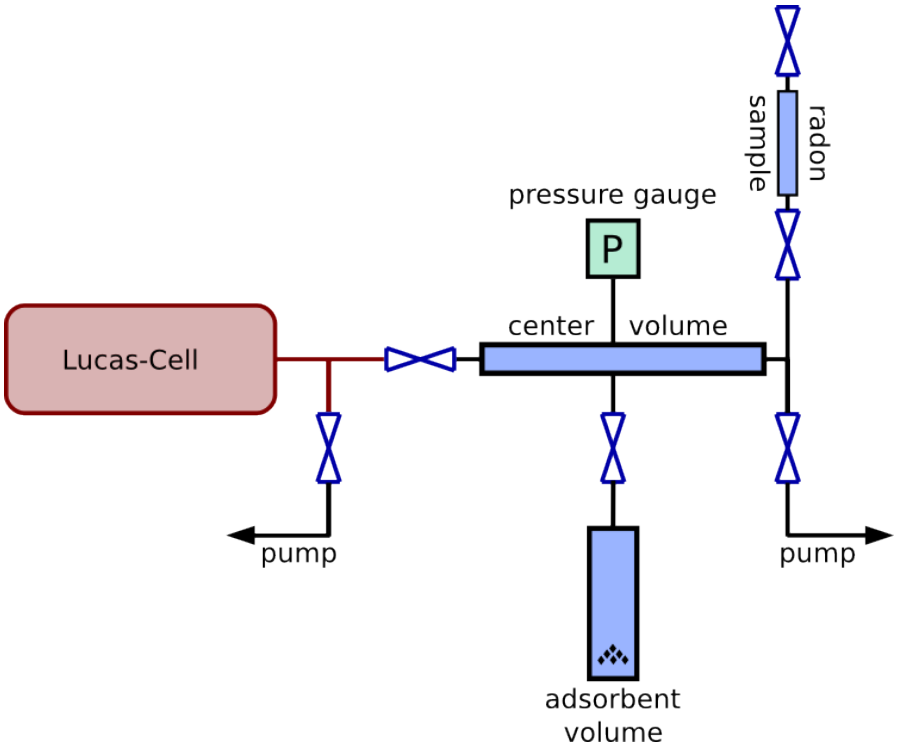

Figure 4.5: Schematic drawing of the experimental setup. On the right side at the top, the radon-helium or radon-xenon sample is mounted. The *center volume* is used to pipette for each measurement only a fraction of the whole sample. By opening the valve between the *center volume* and the *adsorbent volume* the gas sample is brought in contact with the adsorbent and the adsorption equilibrium establishes in both volumes. Xenon adsorption is measured by the mounted pressure gauge. For radon adsorption only the fraction in the *center volume* is expanded into the *Lucas-Cell* where the samples radioactivity is measured. For adsorption measurements at other temperatures the *adsorbent volume* is immersed into a temperature bath. The influence of this partial heating or cooling of the apparatus is quantified and corrected for when finally the adsorption is determined.

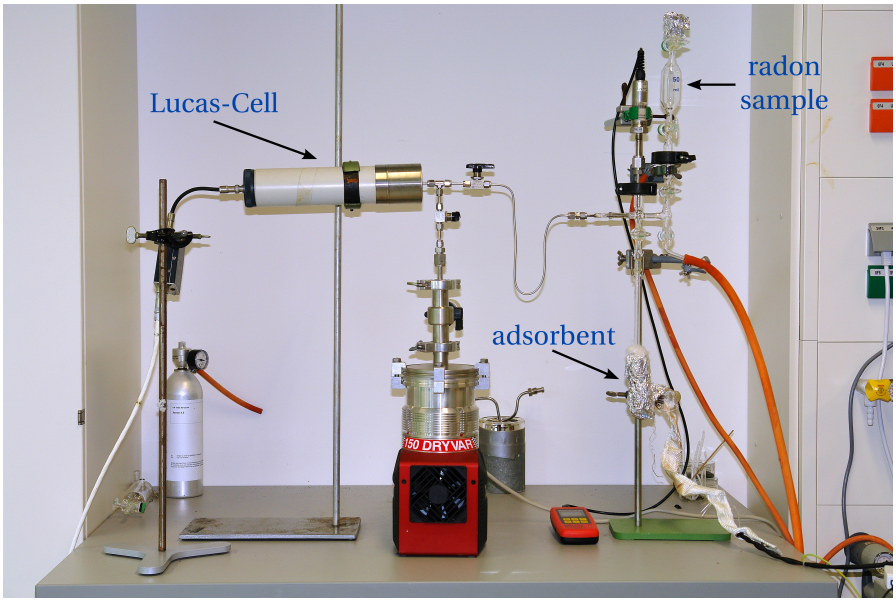

Figure 4.6: Picture of the experimental setup. The *Lucas-Cell* at the very left side and the *radon sample* is at the opposite side at the top. The adsorbent itself, in the *adsorbent volume* at the bottom of the apparatus, can not be seen here since it is covered by a heating mantle.

Radon activity measurements with a Lucas-Cell

A Lucas-Cell [82] is an α-scintillation counter particularly used for measuring radon concentrations. It consits basically of a volume coated with a scintillating material and a photomultiplier tube. The front part of the Lucas-Cell (made of steel in figure 4.6) accommodates the volume to take up the measured gas sample. It is separated from the photomultiplier by a quartz window. The volume's stainless-steel walls are coated with silver-activated zinc sulfide, ZnS(Ag), which is commonly used as scintillator for α-particle detection.
In case of an α-decay inside the Lucas-Cell the emitted α-particle deposits parts of its energy in the coated surface and excites atoms in the scintillator. The gas density during operation is low enough that most of the α-particles reach the walls of the Lucas-Cell (see also section 4.4). The following de-excitation produces photons which propagate through the quartz window and can hit the cathode of the photomultiplier. Due to the photoelectric effect, primary electrons are relieved and directed into an electron multiplier. Here the electrons have to pass a system of dynodes, electrodes which multiply the primary electrons to a measureable voltage. By measuring now the event rate of α-decays inside the Lucas-Cell the radon activity is obtained. However, since the ^{222}Rn progenies ^{218}Po, ^{214}Po and ^{210}Po are α-emitters as well, they can mimic a higher radon concentration. Assuming that

at the time $t = 0$, when the sample is brought into the Lucas-Cell, all counts result from radon decays only,[5] the gradual increase in rate due to progenies produced in the cell by radon decay can then be calculated analytically as shown in section 4.4.2.
Before operation the detector needs to show a negligible background in comparison to the expected radon induced rate. Therefore, after every measurement, the Lucas-Cell needs several half-lifes of the radon progenies to recover. While the radon itself can be pumped easily, the daughter isotopes are collected on the walls where they can contribute to the background.

4.3.2 The measuring procedure

In general the equilibrium adsorption of radon, xenon or any gas can be determined in two ways. By measuring the decrease of pressure in the system or, in case of radon, of the activity when the gas is brought in contact with the adsorbent → *adsorption measurement*. Another way would be by measuring the increase of pressure or activity when an adsorbent is baked and consequently the adsorbed gas is released again → *desorption measurement*.
The experimental setup introduced in this work enables to combine both ways in one cycle of measurements. Both possibilities are not completely independent, since they are based on the same adsorption equilibrium. Nevertheless they allow to cross-check the systematics of both methods.
A cycle of measurements, as carried out in this work, has basically three steps and allows to obtain the radon adsorption and, in case of a radon-xenon mixture, the adsorption of xenon simultaneously.

- *activity measurement of the original mixture*: necessary for radon adsorption measurements to obtain the samples primary activity
- *adsorption measurement*: determination of the decrease of activity and pressure due to adsorption for radon and xenon respectively
- *desorption measurement*: determination of the increase of activity and pressure when the adsorbent is baked for radon and xenon respectively

As already mentioned, one radon sample is used for up to 5 adsorption measurements. This is done by pipetting only a fraction of the sample into the *center volume* which is actual used for one cycle. Once the primary activity is known, the activity of each later measured fraction can be calculated by considering the effect of diluting and the radioactive decay law. Hence, the *activity measurement*

[5] It is assumed that the progenies of radon fall out the gas and stick to the wall. So initially only radon is flushed into the Lucas-Cells volume.

is not necessary in every cycle.

In the following subsections, the process to determine the radon adsorption at room temperature, using a helium-radon or a xenon-radon gas sample, is described in detail. In case of a xenon-radon sample the adsorption of xenon can be determined simultaneously. For changes in the process of measuring for obtaining the adsorption at other temperatures, see subsection 4.3.3. In section 4.4.3 it is explained to calculate from this quantities the relative adsorption coefficient $ad^{Rn/Xe}$ which is then used for further analysis.

Activity measurement

After connecting the pipette containing the sample to the setup, the rest of the apparatus is evacuated, keeping the valve to the *radon sample* closed. After a test for potential leaks all valves are closed. Then the *radon sample* is opened to the *center volume* so that the sample can expand in both volumes. As soon as the pressure, read out on the pressure gauge, is stable, the valve to the *radon sample* is closed again. Only the fraction portioned into the *center volume* is used for the activity measurement. The part of the sample remaining in the pipette is diluted again for further adsorption measurements.
The valve connecting the *Lucas-Cell* is opened and the activity of the sample, A_{act}, is determined. With knowing the apparatus's volume precisely the primary activity of the radon sample is calculated by

$$A_{sample} = \frac{A_{act}\,(V_{RS} + V_{CV})\,(V_{CV} + V_{LC})}{V_{CV} V_{LC}}\,, \tag{4.8}$$

where V_{RS} stands for *radon sample*, V_{CV} for *center volume* and V_{LC} for the *Lucas-Cell* to abbreviate the volume's names.

Adsorption measurement

Once the activity of the sample is known, the radon adsorption can be determined by comparing this value with the activity measured after the adsorption process. It has to be ensured that the adsorbent is baked out (section 4.3.4), all volumes are evacuated and the *Lucas-Cell* has a sufficiently low event rate before the measurement is started. The radon sample is portioned again by pipetting a known activity into the *center volume* only. The pressure is read out at this stage. For every following measurement from the same sample this pressure will decrease due to pipetting into the *center volume*.

Radon-helium-mixtures The decreasing pressure in the *center volume* due to dilution has no influence on the measured radon adsorption. Since helium is in good approximation not adsorbed at all, the mixture is always considered as a single-component radon gas. Furthermore, due to the negligible low partial pressure of this radon gas, Henry's law holds perfectly.

Radon-xenon-mixtures In case of a radon-xenon-mixture however, it is interesting to keep the pressure fixed since xenon, in contrast to helium, has a large impact on the adsorbants capability to adsorb radon. Unless one does not want to examine this suppressing effect by xenon, the pressure at adsorption equilibrium needs to be constant. Hence for the measurements the *Lucas-Cell* is filled with radon free xenon to a pressure higher than that of the sample. This can be done from an additional valve (not shown in figure 4.5) placed before the valve to the pump. By opening carefully to the *center volume* containing the pipetted radon sample, the pressure can be increased to the required constant value p_1. To make sure that no activity escapes from the *center volume* during this process, an activity measurement with the Lucas-Cell is done afterwards. An increased event rate indicates that radon gas has streamed in the opposite direction into the Lucas-Cell.

For both mixtures, the valve to the *activated carbon* is opened to allow adsorption. For the whole time until the adsorption equilibrium is reached, the *center volume* and *adsorbant volume* stay connected so that it is finally reached in both volumes. For radon-xenon-mixtures the pressure p_2, i.e. the adsorption pressure, is read to determine the adsorption of xenon. After reaching equilibrium the valve connecting the *center volume* with the *activated carbon* is closed again. This is essentially to conserve the state of equilibrium in the separated adsorbent volume for the following desorption measurement. The fraction in the *center volume* is now decoupled from the adsorbant but it is still representative for the equilibrium state. It is expanded into the evacuated Lucas-Cell where the activity A_{ad1} is determined. From this quantity the radon adsorption can be determined (see section 4.4.3). Knowing the total activity of the primary sample one can calculate the expected activity of this measurement assuming no adsorption. From the discrepancy to the actual activity the adsorption is obtained.

Desorption measurement

The idea of the desorption measurement is to use the sample's fraction which is conserved in the *adsorbent volume* for an alternative way to obtain the radon adsorption.
Again the *center volume* and the *Lucas-Cell* need to be evacuated and the event

	activity	adsorption	desorption
pressure	-	p_1, p_2	p_3
activity	A_{sample}	A_{ad1}	A_{ad2}

Table 4.4: Overview of the pressure and activity data obtained in the activity-, adsorption- and desorption measurements.

rate has to be low enough. The valve of the *adsorbant volume* is then opened to expand the gas into the *center volume*. A heating mantle is placed around the bottom of the *adsorbant volume* (see figure 4.6) and the adsorbent is baked at 200 °C for 1.5 hours, keeping the valve open. Due to the heating, the radon and xenon desorb and expand in the volume. It has been tested, that this baking time and temperature is sufficient to release practically all adsorbed radon. Since only the bottom part of the *adsorbant volume* is heated the effect of a gradient in temperature on the gas density has to be investigated (see section 4.3.3). The xenon adsorption is obtained by reading the pressure p_3 while the *adsorbant volume* is still heated.
Next the valve to the *adsorbant volume* is closed to decouple it again from the *center volume* and the heating mantel is removed. Because the *center volume* is still warmer than the *Lucas-Cell*, it is necessary to wait until the *center volume* has cooled down to avoid the influence of the temperature gradient between this two volumes. By opening the *Lucas-Cell* the activity measurement A_{ad2} is started.

4.3.3 Adsorption measurements at different temperatures

The temperature dependence of the adsorption properties of different adsorbents has also been studied. The results of measurements at 273 K, 295 K, 333 K and 363 K are shown. To keep conditions stable the *adsorbent volume* is immersed in a water bath which minimizes temperature fluctuations to ±1 K.

As it is not possible to keep the whole apparatus at the same temperature, occurring temperature gradients during the measurement procedure need to be considered. The water bath should not be installed before pipetting the sample into the *center volume* for the adsorption measurement. This is to avoid any gradient in density due to partial heated or cooled volumes/surfaces. Otherwise it cannot be ensured that every time of pipetting the radon sample the same fraction of activity is obtained. For every activity measurement one has to ensure that the water bath is removed and the volumes/surfaces have reached room temperature again, before the valve to the *Lucas-Cell* is opened.

temperature [K]	**helium**	**xenon**
520 (baking)	1.09 ± 0.02	1.06 ± 0.03
273	0.99 ± 0.02	-
333	1.02 ± 0.02	-
262	1.04 ± 0.01	-

Table 4.5: The measured f_{corr} for different temperatures and gases. For xenon only adsorption measurements at room temperature have been carried out.

As already mentioned in the last section, the partial heating of the apparatus when the adsorbent is baked, but also when a water bath is installed, causes a gradient in the particle density. Since the *adsorbent volume* and the *center volume* are connected when the gas is brought into contact with the adsorbent, the pressure measured in the *center volume* is expected to be shifted. Hence it is necessary to corrected the obtained data for this effect.
This is done by applying a factor $f_{corr}(T)$ which specifies the deviation of the pressure in the *center volume* in dependence of the temperature of the *adsorbent volume*. $f_{corr}(T)$ is < 1 for temperatures lower than room temperature and > 1 if the adsorbent is heated. For the baking temperature $f_{corr}(T)$ has allready been introduced as f_T.
To obtain the corresponding $f_{corr}(T)$ for the different temperatures and gases (helium or xenon) several measurements have been performed. To do so, the empty *adsorbent volume* (i.e. without adsorbent) and the connected *center volume* is filled with helium/xenon. Then the water bath is installed. After the pressure, read out in the *center volume* is stable, one calculates from the Δp measured before and after the heating/cooling the correction factor $f_{corr}(T)$. Note that for this correction factor the *center volume* is assumed to be always at room temperature even though the *adsorbent volume* is baked. The obtained values of $f_{corr}(T)$ can be found in table 4.5.

4.3.4 Preparation of the radon sample

The used radon source is an aqueous radium barium-chloride solution with an activity of 28 kBq. For the measurements with radon-helium mixtures the source is kept under helium atmosphere. Produced by α-decay of ^{226}Ra, the ^{222}Rn distributes in the helium. When a sample is extracted, a pipette (i.e. the *radon sample* in figure 4.5) is mounted on the source and evacuated. Using the helium in the source as a carrier gas, the radon in the gas phase is then streaming into the pipette when the connecting valve is opened. The activity of the final sample in the pipette is approximately 5 to 6 kBq. Since the precise value is determined

before every adsorption measurement, it is not required to have a well defined radon source.
For the measurements with radon-xenon mixtures the helium is flushed out from the source and replaced by xenon.

Influence of humidity on adsorption

An issue which has to be considered is the influence of humidity on the adsorbents capability to adsorb radon. It is a well known effect that the adsorption of a particular gas may be suppressed in the presence of an additional gas component. Since the radium solution is a possible source for humidity in the sample, the competitive adsorption of the water vapor might influences the result.
The adsorption of water vapor on activated carbon was studied by [83] and [84]. A typical adsorption isotherm of water vapor is shown in figure 4.7. P is the actual pressure and P_0 the saturation pressure of the vapor. According to the classification of isotherms introduced in section 4.2.4 water vapor shows a Type V isotherm. While at low pressures the isotherm is very flat, i.e. the adsorption of water vapor is very small, it typically shows a sharp rise at a relative pressure of about $\frac{P}{P_0} = 0.5$ until the maximum amount of adsorption is reached at the saturation pressure. This well known shape is explained by condensation of the water in the pores of the activated carbon at higher pressures [85]. Although the sample is diluted during the process the relative humidity might still be high enough to disturb the measurement.

Before the actual adsorption measurements of activated carbons started, the suppression of radon adsorption due to the coexistence of radon and water-vapor was tested by adding humidity to the system on purpose. For this test, a water container was connected to the apparatus enable to fill the *center volume* with water vapor to saturation pressure.
Following the usual measuring process the radon adsorption on the activated carbon *Bluecher: 100050* was determined for the prepared sample. The result showed a suppression of the radon adsorption capability of approximately 33% compared to the same measurement without artificially increased humidity. Then the rest of the same sample was used for a second adsorption measurement. Due to dilution the initial humidity of the prepared sample has been reduced by 50%. This time only a small suppression of about 5% compared to the common measurements without additional humidity was found.

The influence of water vapor from the aqueous radon source has not been studied in detail. However, the above described measurements show that humidity is an issue one has to be taken into account. As a consequence, every radon sample was

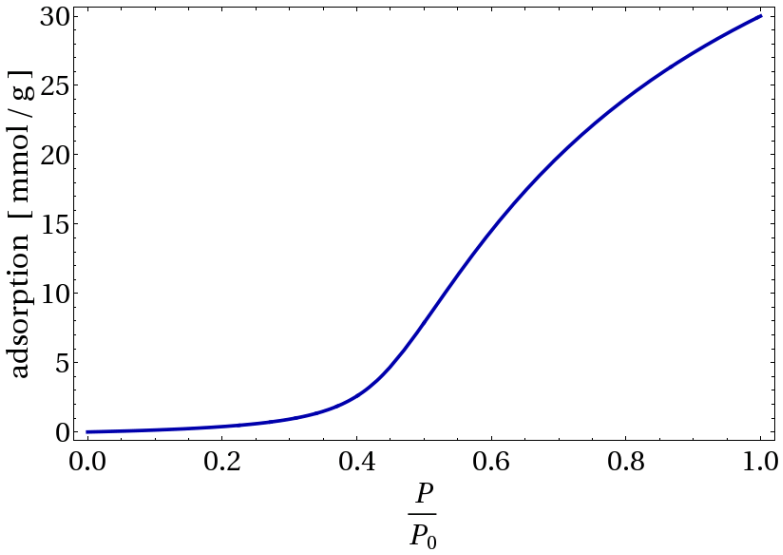

Figure 4.7: An example for a water vapor isotherm measured with activated carbon [83], [84]. Typical is the isotherms shape with the rather poor adsorption capability at low relative pressures and the sharp increase at about $\frac{P}{P_0} = 0.5$ due to condensation of water in the pores of the adsorbent.

treated with silica gel to reduce its humidity before a circle of measurement starts (see section 4.3.4).

Treatment with silica gel

Silica gel is an adsorbent widely used for drying processes (see section 4.2.2). Due to its surface polarity, it adsorbs polar molecules like water more effective than non polar molecules or atoms like xenon or radon. The adsorption of radon by silica gel has been studied in [86]. There it was found that the radon uptake of silica gel is rather poor compared to that of other adsorbents like activated carbon or molecular sieve 13X. In [87] silica gel (Kromasil) was used to separate water vapor from helium-radon and nitrogen-radon mixtures. Even at low temperatures it exhibited a very small adsorption power for radon while water vapor was adsorbed effectively.

These results motivate to use silica gel to get rid a of possible vapor component in the radon sample originating from the radon source. For this purpose a small glass volume containing the silica gel was built. It has two flanges, one to mount the *radon sample* volume and a second one to allow pumping. The pressure is controlled with a pressure gauge. This volume was finally filled with 0.14g of silica

gel from MERCK KGaA[6] (product no.:1.07733.9025). The silica gel was baked for 14 h at 150 °C, while evacuating the same time, to guarantee full capability.
To evaluate the performance of the silica gel a test was carried out by filling the *radon sample* volume with saturated water vapor. After mounting the valve to the evacuated volume containing the silica gel was opened. By reading out the pressure after reaching the equilibrium the reduction of humidity is obtained. It turned out that after this treatment with 0.14 g of silica gel the humidity was reduced to $(25.8 \pm 1)\%$. It should be noticed that 1/3 of the reduction is due to dilution. Increasing the amount of silica gel will obviously reduce humidity more efficient. However, it has to be considered that radon is lost as well.
Every time before a new radon sample is used for adsorption measurements it is now treated with silica gel for 1.5 h. Assuming the above described performance, water vapor is reduced to a level of humidity that its influence on radon adsorption is negligible (low pressure region in figure 4.7). Concerning the loss of radon, a precise value can not be given since the radon sources activity can not be assumed to be stable. Anyway, data suggests a loss of about 30% due to both effects: adsorption on silica gel and dilution.

[6] http://www.merck.de/de/index.html

4.4 Data analysis and evaluation

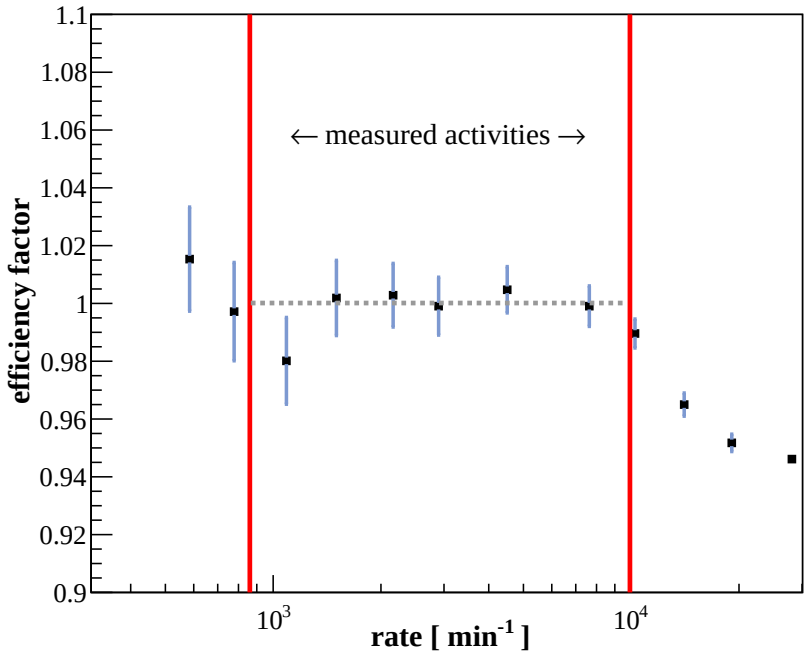

Figure 4.8: Detecting efficiency of the Lucas-Cell as a function of the measured activity. The non-linear behavior is not understood yet but has to be considered in data evaluation. The red lines are marking the range of the measured activities where the efficiency is considered to be constant.

4.4.1 Performance of the Lucas-Cell

The PMT on the Lucas-Cell is operated with a positive bias high voltage of 850 V. A typical signal pulse from the photomultiplier as triggered by an α-particle has then an amplitude of about 5 V. After a steep rising time of 10 μs the pulse decreases with a half life of 40 μs. The signal is fed into a Single Channel Analyzer (Ortec 488 Timing SCA) which allows to set an energy threshold of 1.5 V to reject noise, and from there into a DAQ (National Instruments USB-6009) which can be operated as a counter.
Before data taking, the setup has been tested for stability and the detection efficiency has been determined. Starting with a radon-xenon mixture of about 500 Bq as a benchmark, the activity of the same sample was measured several times at constant xenon pressure. However, due to diluting the activity of the sample decreases after every measurement which needs to be taken into account when

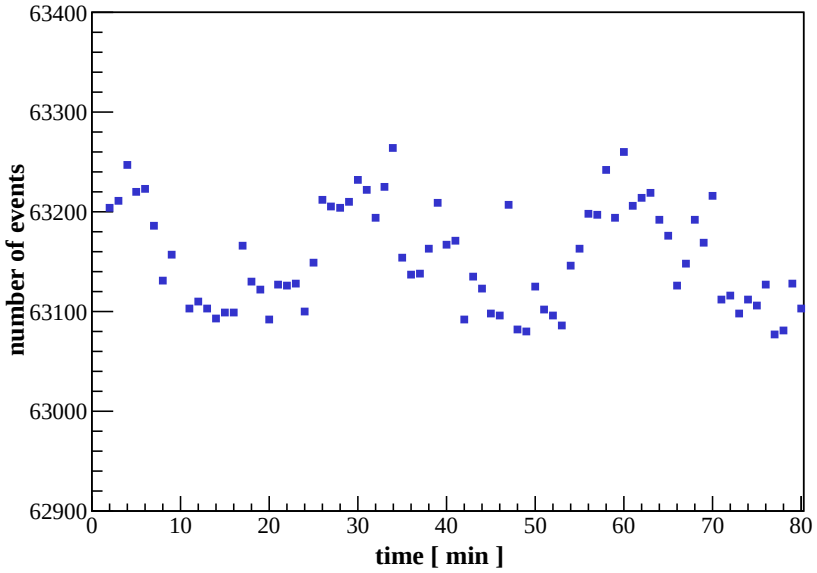

Figure 4.9: The stability of the DAQ has been tested with a pulse generator. A tiny oscillation of $\approx 0.2\%$ was found. The here probed pulse width is 10 μs.

comparing the results with each other. As shown in figure 4.8, the efficiency of the Lucas-Cell at high counting rates increases with decreasing activity as expected from pile-up effects. When the count rate is lower then 10 000 counts per minute the efficiency becomes stable. Since for all measurements the obtained activity is in this stable region, the efficiency is assumed to be the same. A statistical error, extracted by a fit of this plateau-region, is considered for the results. To exclude effects on efficiency caused by the DAQ, its stability has been tested with a pulse generator which simulates the α-rate in the Lucas-Cell. Stability within 0.2% was observed altough an inexplicable oscillation in the efficiency of this size and a period of ≈ 30 min was found (see figure 4.9). The amplitude however, is too small to have any influence on the obtained results for radon adsorption.

Another parameter which could influence the efficiency might be the gas pressure in the Lucas-Cell. The probability of an α-particle to reach the scintillating walls decreases with an increasing particle density of the gas. Results of a Monte Carlo simulation (Geant4) with helium and xenon are shown in figure 4.10. Keeping the pressure in the Lucas-Cell constant for all activity measurements prohibits this effect.

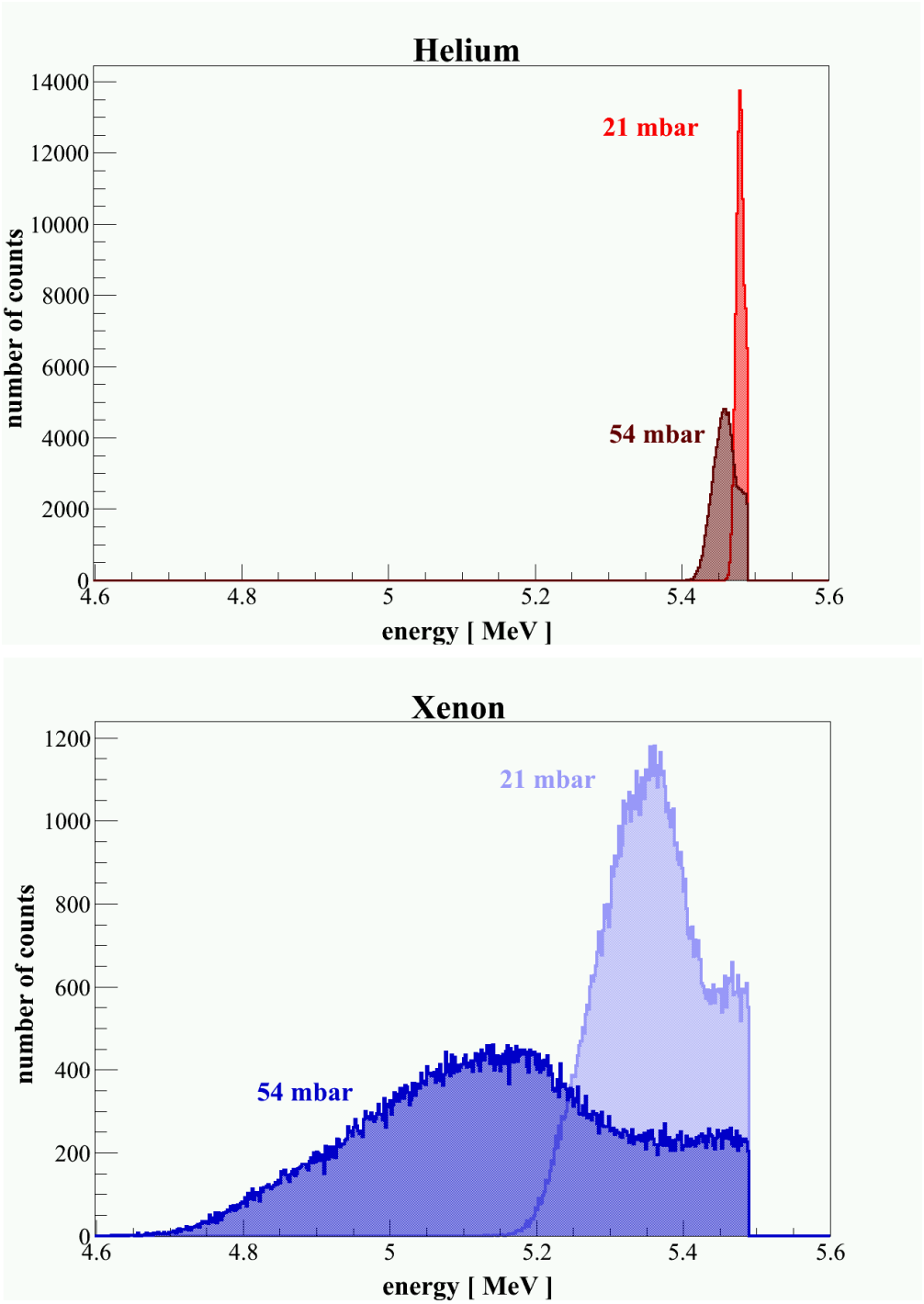

Figure 4.10: Monte Carlo simulation of the energy spectrum of the ^{222}Rn α-decay as detected by the Lucas-Cell for helium-radon mixture (top) and xenon-radon mixture (bottom). Due to the rather dense xenon gas in the detector the spectrum gets smeared at higher pressures which, at some point, influences the detecting efficiency.

4.4.2 Data analysis of activity measurements

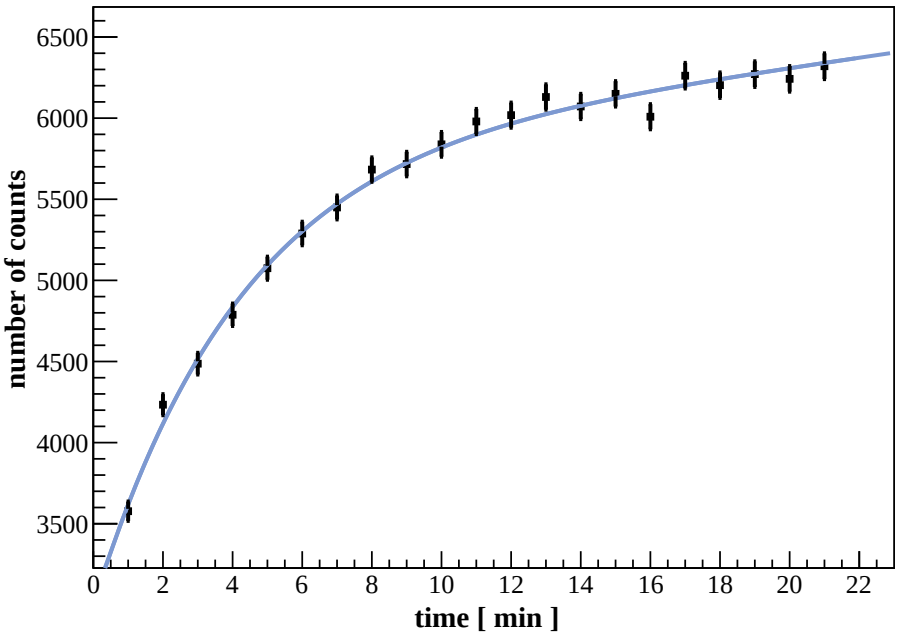

Figure 4.11: Example of experimental data measured with the Lucas-Cell. The fit was done with the analytic function 4.9 to obtain the ^{222}Rn activity.

Over a measured period of 20 min the number of counts per minute is recorded. When the Lucas-Cell is opened for the radon sample the count rate is not constant but increases in time since α-decaying daughter isotopes are produced from the initial radon. This evolution follows the analytical function [88]

$$A(t) = A^0_{Rn}\, e^{-\lambda_a\, t} + A^0_{Rn} \left(\frac{\lambda_b}{\lambda_b - \lambda_a}\right) \left(\, e^{-\lambda_a\, t} - \, e^{-\lambda_b\, t}\right) + A^0_{Rn}\, \lambda_b\, \lambda_c\, \lambda_d\, \lambda_e\, Y \quad (4.9)$$

where

$$\begin{aligned} Y = & \frac{e^{-\lambda_a\, t}}{(\lambda_b - \lambda_a)(\lambda_c - \lambda_a)(\lambda_d - \lambda_a)(\lambda_e - \lambda_a)} + \frac{e^{-\lambda_b\, t}}{(\lambda_a - \lambda_b)(\lambda_c - \lambda_b)(\lambda_d - \lambda_b)(\lambda_e - \lambda_b)} \\ & + \frac{e^{-\lambda_c\, t}}{(\lambda_a - \lambda_c)(\lambda_b - \lambda_c)(\lambda_d - \lambda_c)(\lambda_e - \lambda_c)} + \frac{e^{-\lambda_d\, t}}{(\lambda_a - \lambda_d)(\lambda_b - \lambda_d)(\lambda_c - \lambda_d)(\lambda_e - \lambda_d)} \\ & + \frac{e^{-\lambda_e\, t}}{(\lambda_a - \lambda_e)(\lambda_b - \lambda_e)(\lambda_c - \lambda_e)(\lambda_d - \lambda_e)} \,. \end{aligned}$$

$\lambda_a - \lambda_e$ are the decay constants from ^{222}Rn to ^{214}Po following the ^{238}U decay chain. The pure radon activity A^0_{Rn} in equation 4.9 is the quantity looked for and extracted by a fit to the experimental data like in figure 4.11.

4.4.3 Evaluation of the measurements

Following the measuring procedure as described in section 4.3.2, the pressure and activity quantities summarized in table 4.4 are obtained. Three values of pressure to calculate xenon adsorption and three activity measurements for radon adsorption respectively are determind in one cycle of measuremts. For evaluation a *relative adsorption coefficient* is defined as

$$ad \equiv \left(\frac{n_{ad}}{n_{tot}}\right) = 1 - \left(\frac{n_{free}}{n_{tot}}\right) , \tag{4.10}$$

where n_{ad} is the amount of gas (i.e. radon or xenon) adsorbed, n_{free} the amount in the gas phase (i.e. not adsorbed) in the adsorption equilibrium and $n_{tot} = n_{ad} + n_{free}$ the total amount of gas involved in the measurement. Combining two pressures or activities from table 4.4 respectively, gives three ways of determing the same adsorption coefficient ad (labeled as ad1, ad2 and ad3). This provides an opportunity to cross check the results.

Xenon adsorption

According to the ideal gas law the total amount of substance in a closed system is proportional to the pressure,

$$n_{tot} = \alpha \cdot p , \tag{4.11}$$

where α is a constant. This simplified relation is used to obtain the *relative adsorption coefficient* for xenon.

ad1: The amount of xenon in the *center volume* (V_{CV}) of the setup is therefore given by $n_{tot} = \alpha \cdot p_1$. Following the above described measuring process, the valve to the evacuated *adsorbent volume* (V_{AD}) is opened, the xenon in V_{CV} is diluted by the factor $(V_{AD} + V_{CV})/V_{CV}$. This would be the expected value of p_2 if no adsorption takes place. However, due to adsorption the measured pressure is smaller and the actual xenon in the gas phase in V_{CV} is given by $n_{free} = \alpha \cdot p_2$. The ratio of the actual measured and the expected values of p_2 gives the *relative adsorption coefficient* (equation 4.10):

$$ad^{Xe} = ad^{Xe}(p_1, p_2) = 1 - \frac{p_2\,(V_{AD} + V_{CV})}{p_1\,V_{CV}} \tag{4.12}$$

ad^{Xe} as a function of p_1 and p_2 is labelled as $\mathbf{ad1^{Xe}}$.

ad3: On the other hand it is also possible to obtain ad^{Xe} from the amount of gas getting desorbed when the adsorbent is baked. The associated quantity is p_3.
At the beginning of the desorption measurement V_{CV} is evacuated, while V_{AD} contains the adsorbed xenon, $n_{ad} = ad \cdot n_{tot}$, but also the non-adsorbed xenon in the gas phase, $n_{free} = (1 - ad)\ n_{tot}\ \frac{V_{AD}}{V_{AD}+V_{CV}}$. The amount of xenon in the volume V_{AD} is therefore given by

$$n_{de} = ad^{Xe} \cdot n_{tot} + (1 - ad^{Xe})\ n_{tot}\ \frac{V_{AD}}{V_{AD} + V_{CV}}\ , \tag{4.13}$$

where the factor $\frac{V_{AD}}{V_{AD}+V_{CV}}$ is due to the limitation to the xenon in V_{AD}.
In the next step V_{AD} is baked. When the valve to the evacuated V_{CV} is opened, n_{de} expands in the combined volume. The pressure p_3, measured in V_{CV}, is related to n_{de} by

$$n_{de} = \alpha\ p_3\ \frac{1}{f_T}\ \frac{V_{AD} + V_{CV}}{V_{CV}}\ . \tag{4.14}$$

Since V_{AD} is baked to release the adsorbed radon, it should be noted that only in V_{CV} the temperature is considered to be stable (room temperature). As a result, the above relation has an additional factor $1/f_T$ which corrects for effects on p_3 due to partial heating. The higher particle density in the cooler V_{CV} mimics an increased n_{de}. The correction factor has been measured for the here presented setup and was found to be 1.09 for xenon (see section 4.3.3). The volume-factor is necessary to include also the xenon in V_{AD}[7].
With equation 4.24 and the relation $n_{tot} = \alpha \cdot p_1$, n_{tot} and n_{de} in equation 4.13 can be replaced by the measured quantities p_1 and p_3

$$p_3\ \frac{1}{f_T}\ \frac{V_{AD} + V_{CV}}{V_{CV}} = ad^{Xe}\ p_1 + (1 - ad^{Xe})\ p_1\ \frac{V_{AD}}{V_{AD} + V_{CV}}\ . \tag{4.15}$$

Solving now equation 4.15 for the *relative adsorption coefficient* gives:

$$ad^{Xe} = ad^{Xe}(p_1, p_3) = \frac{p_3\ (V_{AD} + V_{CV})^2 - f_T\ p_1\ V_{AD}\ V_{CV}}{p_1\ f_T\ V_{CV}^2} \tag{4.16}$$

ad^{Xe} as a function of p_1 and p_3 is labelled as $\mathbf{ad3^{Xe}}$.[8]

[7] In the procedure of measurement p_1 is measured in the volume V_{CV}. The above definition $n_{tot} = \alpha \cdot p_1$, α = const., therefore implies V_{CV} as the reference-volume. Ignoring the volume-factor in equation 4.24 would give the amount of xenon in V_{CV} alone.

[8] The unsorted labelling is motivated by the size of the systematic errors (section 4.5).

ad2: The third way of obtaining ad^{Xe} is easily derived from the above equations. Solving equation 4.12 for p_1 gives

$$p_1 = \frac{p_2\ (V_{AD} + V_{CV}}{V_{CV}\ (1 - ad^{Xe})}\ . \tag{4.17}$$

By inserting above expression for p_1 into equation 4.15 and solving it afterwards for ad^{Xe} one finds

$$ad^{Xe} = ad^{Xe}(p_2, p_3) = \frac{p_3\ (V_{AD} + V_{CV}) - f_T\ p_2\ V_{AD}}{p_3\ (V_{AD} + V_{CV}) + f_T\ p_2\ V_{CV}} \tag{4.18}$$

ad^{Xe} as a function of p_2 and p_3 is labelled as $\mathbf{ad2^{Xe}}$.

Radon adsorption

The derivation of the *relative adsorption coefficient* for radon adsorption, $ad^{\,Rn}$, is basically similar to that of the xenon adsorption explained above. To determine the amount of radon in a sample, the pressures p_i, which were used to obtain the xenon adsorption, are replaced by activity measurements. Analogous to equation 4.11 one can write a simplified relation between the amount of radon in a certain volume and the measured activity A_{act}

$$n = \beta \cdot A_{act} \cdot e^{-\lambda_{Rn}\ t}\ , \tag{4.19}$$

where the exponential factor describes the radioactive decay of the radon atoms in the sample. Note that the constant β depends on the detector efficiency.
As described in section 4.3.2 the radon sample is stored in V_{RS} and can be used for several adsorption measurements by pipetting only a fraction into the *center volume* (V_{CV}) each time. Since the activity in V_{CV} is not measured for every single fraction, the total amount of radon n_{tot} of the whole radon sample is determined at the beginning of every *cycle of measurements* (see section 4.3.2).

$$n_{tot}(t) = \beta\ \frac{V_{RS} + V_{CV}}{V_{CV}}\ \frac{V_{CV} + V_{LC}}{V_{LC}}\ A_{act} \cdot e^{-\lambda_{Rn}\ t}\ . \tag{4.20}$$

A_{act} is the activity measured in the *Lucas-Cell* (V_{LC}). The volume factors are due to diluting from the *radon sample* to the *center volume* and from the *center volume* to the *Lucas-Cell*. Since the radon decays n_{tot} has a time dependence, represented by the exponential factor.
The knowledge of n_{tot} at a certain time is used to calculate the amount of radon pipetted into V_{CV} for the actual adsorption measurements. The dilution has to be taken into account by an additional factor $V_{CV}/(V_{RS} + V_{CV})$. Furthermore

another dilution factor is required since the radon concentration in V_{RS} decreases each time when a fraction is pipetted into the *center volume*. This is represented by $(V_{RS}/(V_{RS}+V_{CV}))^a$, where a stands for the number of expansions of the radon sample to V_{CV}. The radon in the *center volume* is finally given by

$$n_{frac} = n_{tot}(t) \left(\frac{V_{RS}}{V_{RS}+V_{CV}}\right)^a \frac{V_{CV}}{V_{RS}+V_{CV}} . \tag{4.21}$$

ad1: Similar to the xenon adsorption the *relative adsorption coefficient* is obtained by comparing the amount of radon in V_{CV} assuming no adsorption (equation 4.21 with additional diluting into V_{AD})

$$n = n_{frac} \frac{V_{CV}}{V_{AD}+V_{CV}}$$

to the actual measured value

$$n_{free} = \beta \cdot A_{ad} \frac{V_{LC}+V_{CV}}{V_{LC}}$$

A_{ad} is the measured activity after adsorption took place (see section 4.3.2), t_{ad} is the time lag of A_{act} and A_{ad} while n_{free} is the amount of radon in the gas phase in the adsorption equilibrium. With the help of equation 4.10 one finds for the *relative adsorption coefficient*

$$ad^{Rn} = ad^{Rn}(A_{act}, A_{ad}) = 1 - \frac{A_{ad}\,(V_{RS}+V_{CV})^a (V_{AD}+V_{CV})}{A_{act}\; e^{-\lambda_{Rn}\, t_{ad}}\; (V_{RS})^a\; V_{CV}} \tag{4.22}$$

ad^{Rn} as a function of A_{act} and A_{ad} is labelled as $\mathbf{ad1^{Rn}}$.

ad3: For the second option to obtain ad^{Rn} one can follow the same derivation as explained for xenon adsorption. Adopting equation 4.13 for radon gives[9]

$$n_{de} = ad^{Rn} n_{frac} + (1 - ad^{Rn})\; n_{frac} \frac{V_{AD}}{V_{AD}+V_{CV}} \tag{4.23}$$

Analogous to equation 4.24 one obtains

$$n_{de} = \beta\; A_{de} \frac{1}{f_T} \frac{V_{LC}+V_{CV}}{V_{LC}} \frac{V_{AD}+V_{CV}}{V_{CV}} \tag{4.24}$$

[9]Note that n_{tot}, as introduced for derivation of ad^{Xe}, is the amount of xenon in V_{CV}. In case of radon the analogous quantity is n_{frac}.

where A_{de} is the activity from the desorption measurement (see section 4.3.2). Using now the relations 4.21 and 4.24 to replace n_{frac} and n_{de} respectively, finally allows to solve equation 4.23 for the *relative adsorption coefficient*:

$$\begin{aligned} ad^{Rn} &= ad^{Rn}(A_{act}, A_{de}) \\ &= \frac{A_{de}\,(V_{AD}+V_{CV})^2\,(V_{RS}+V_{CV})^a\,e^{\lambda_{Rn}t_{de}} - f_T\,A_{act}\,V_{AD}\,V_{CV}\,(V_{RS})^a}{f_T\,A_{act}\,(V_{CV})^2\,(V_{RS})^a} \end{aligned} \tag{4.25}$$

With t_{de} as the time difference between A_{act} and A_{de}.

ad^{Rn} as a function of A_{act} and A_{de} is labelled as $\mathbf{ad3^{Rn}}$.

ad2: For deriving the third option equation 4.22 is solved for A_{act}

$$A_{act} = \frac{A_{ad}\,(V_{RS}+V_{CV})^a\,(V_{AD}+V_{CV})}{(1-ad^{Rn})\,V_{CV}\,(V_{RS})^a\,e^{-\lambda_{Rn}t_{ad}}}\,. \tag{4.26}$$

By inserting above relation into equation 4.25, the *relative adsorption coefficient* is obtained

$$\begin{aligned} ad^{Rn} &= ad^{Rn}(A_{ad}, A_{de}) \\ &= \frac{A_{de}\,(V_{AD}+V_{CV})\,e^{\lambda\,\Delta t} - f_T\,A_{ad}\,V_{AD}}{A_{de}\,(V_{AD}+V_{CV})\,e^{\lambda\,\Delta t} + f_T\,A_{ad}\,V_{CV}} \end{aligned} \tag{4.27}$$

with $\Delta t = t_{de} - t_{ad}$ as the time difference between A_{ad} and A_{de}.

ad^{Rn} as a function of A_{ad} and A_{de} is labelled as $\mathbf{ad2^{Rn}}$.

Adsorption measurements at other temperatures

The above introduced relations for the *relative adsorption coefficient* hold only for measurements at room temperature. To obtain the adsorption at other temperatures, the *adsorbent volume* V_{AD} is cooled/heated. Analogous to f_T, which corrects for the partial heating of V_{AD} when the adsorbent is baked, another correction f_{corr} is required as described in section 4.3.3. This factor has to be applied on p_2 and A_{ad} respectively, to compensate the inhomogeneous particle density in the gas phase (n_{free}) of the adsorption equilibrium due to the cooling/heating of V_{AD}. Apart from that, the derivation of the *relative adsorption coefficients* is identical to the description above.

Xenon adsorption

$$ad1^{Xe} = 1 - \frac{p_2\ (V_{AD} + V_{CV})}{p_1\ f_{corr}\ V_{CV}} \tag{4.28}$$

$$ad2^{Xe} = \frac{p_3\ f_{corr}\ (V_{AD} + V_{CV}) - f_T\ p_2\ V_{AD}}{p_3\ f_{corr}\ (V_{AD} + V_{CV}) + f_T\ p_2\ ((f_{corr} - 1)\ V_{AD} + f_{corr}\ V_{CV})} \tag{4.29}$$

$$ad3^{Xe} = \frac{f_{cor}\ p_3\ (V_{AD} + V_{CV})^2 - f_T\ p_1\ V_{AD}\ V_{CV}}{f_T\ p_1\ V_{CV}((f_{corr} - 1)V_{AD} + f_{corr}V_{CV})} \tag{4.30}$$

Radon adsorption

$$ad1^{Rn} = 1 - \frac{A_{ad1}\ (V_{RS} + V_{CV})^a\ (V_{AD} + V_{CV})}{f_{corr}\ A_{act}\ e^{-\lambda_{Rn} t_{ad}}\ V_{CV}\ (V_{RS})^a} \tag{4.31}$$

$$ad2^{Rn} = \frac{f_{corr}\ A_{de}\ (V_{AD} + V_{CV})\ e^{\lambda(t_{de} - t_{ad})} - f_T\ A_{ad}\ V_{AD}}{f_{corr}\ A_{de}\ (V_{AD} + V_{CV})\ e^{\lambda(t_{de} - t_{ad})} + f_T\ A_{ad}\ ((f_{corr} - 1)\ V_{AD} + f_{corr}\ V_{CV})} \tag{4.32}$$

$$ad3^{Rn} = \frac{f_{corr}\ A_{de}\ e^{\lambda t_{de}}\ (V_{RS} + V_{CV})^a\ (V_{AD} + V_{CV})^2 - f_T\ A_{act}\ V_{AD}\ V_{CV}\ (V_{RS})^a}{f_T\ A_{act}\ ((f_{corr} - 1)\ V_{AD} + f_{corr}\ V_{CV})\ (V_{RS})^a} \tag{4.33}$$

Error determination

The error of the final results is dominated by the error of the pressure gauge. Its error was estimated to be 1 mbar (last digit). Since the ratios of the setup's volumes have been determined by pressure measurements, this error consequentially propagates into the evaluation (see table 4.3.1). In case of xenon adsorption, both, the pressure quantities p_i and the uncertainty on the volumes generate the overall error. The error on the measured radon adsorption results also from the volumes but an additional error of $\sim$1% is due to data fitting (figure 4.11) and due to the detection efficiency of the Lucas-Cell (see figure 4.8). The error for the radon adsorption increases every time when pipetting from the same radon sample.
The relative error of the *relative adsorption coefficients* for radon, $ad1^{Rn}$, was found to be less than 1% for the measurements at room temperature but 3% for the measurement at 363 K where the adsorption coefficient is small. In case of

xenon, $ad1^{Xe}$ showed a relative error of 3%. $ad2^{Xe/Rn}$ and $ad3^{Xe/Rn}$ have larger errors due to systematics and are used to cross check the results.
For the calculation of the amount of gas being adsorbed per gram adsorbent an error for the temperature of 1 K and for the adsorbent mass, 0f ∼0.5%, has been considered. The derived values for Henry's constants have an error of <10%. In appendix C the error calculations for $adi^{Xe/Rn}$ and for Henry's constants are given.

4.5 Results and discussion

In this section the results of radon and xenon adsorption measurements on activated carbon samples are presented. Relevant properties of the three different charcoal samples used in this work are given at the beginning of this section. Starting then with a radon-helium mixture as a sample, the radon uptake on the activated carbon *Blücher 100050* is determined at different temperatures. Using the van t'Hoff equation, as model for the temperature dependence of Henry's constant allows to obtain the isosteric heat of adsorption.
Since for the application in XENON1T the adsorption of radon in presence of xenon is important, results of the two-component radon/xenon-adsorption are presented in the second part of this section. The xenon uptake on the activated carbon *Blücher 100050* is measured at different temperatures and pressures. Radon-adsorption at room temperature and at fixed pressure is then obtained for the same and two further charcoals samples (see table 4.6). This allows the comparison of the different candidate charcoals. Interesting is also the time development of the adsorbed amount of radon. As shown below, the establishment of the radon adsorption equilibrium takes longer than for xenon and depends furthermore on the adsorbent. The time until an adsorbent shows its full capacity is an important quality criteria for the planned application in XENON1T since, as discussed in section 4.1, the radon removal system needs to be operated in a loop mode. The results are summarized and discussed in the last part of this section.

4.5.1 Adsorbent samples

Activated carbons are used as adsorbents as their large surface area and micropore volume are very promising for a high adsorption capability. In addition it as in general a nonpolar surface. Measurements with other adsorbents, zeolite e.g., are planned for the near future.
Selected properties of three different activated carbons samples used are given in table 4.6. Two of them were produced by the German company Blücher [89] and have the product numbers *100050* and *100878*. The third charcoal is a product

Product No.	**100050**	**100878**	***SHIRASAGI* G2x4/6-1**
company	Blücher	Blücher	JEChem
samples mass [10^{-6} kg]	36.5 ± 0.2	39.4 ± 0.2	36.8 ± 0.2
surface, MP BET[a] [m^2/g]	1361[b]	1045[b]	1190
total pore volume [cm^3/g]	0.64[c]	0.51[c]	0.51
micropore volume [cm^3/g]	0.533	0.386	0.449
fraction micropores [%]	83.8	76.3	87.9
average pore width [Å]	18.7	19.4	17.2

Table 4.6: Parameters of measured charcoals in comparison. Data is kindly received from both companies on enquiry.

[a]Multi Point BET (Brunauer, Emmett and Teller) [90]
[b]Method: ASTM D6556-04 [91]
[c]Method: Gurvich at 0.995 [92]

from the Japanese company JEChem[10] and is labelled *SHIRASAGI G2x4/6-1*.
The raw material of both Blücher charcoals are synthetic polymers [89]. This allowes a high grade of reducibility and purity of the adsorbent. Activated carbon *100050* has a higher activation level than *100878* which is reflected in a larger surface area and total pore volume. The average pore width, however, is slightly larger at sample *100878*. Both activated carbons are of spherical shape and show high mechanical robustness.
SHIRASAGI G2x4/6-1, in contrast, is a pelletized charcoal based on coconut-shell as raw material[10]. The surface area is found to be in-between the Blücher charcoals while the total pore volume is the same than of *100878* altough it should be emphasized that the method of measuring for *SHIRASAGI G2x4/6-1* is unknown.

4.5.2 Helium-radon mixture

To study the single component adsorption of radon, helium is used as a carrier gas since it is known to have a negligible adsorption in very good approximation. As pointed out in [93] for zeolites and [94] for activated carbon, the amount of helium being adsorbed strongly depends on temperature and pressure. Only at

[10]www.jechem.co.jp/english/index.html

temperature [K]	**rel. adsorption** [10^2]		
	$ad1^{Rn}$	$ad2^{Rn}$	$ad3^{Rn}$
273	97.3 ± 0.4	97.6 ± 0.4	99 ± 2
294	91.1 ± 0.4	91.1 ± 0.4	91 ± 3
333	59.7 ± 0.5	60.5 ± 0.6	63 ± 3
363[a]	31 ± 1	-	-

Table 4.7: Single component radon adsorption at different temperatures. $ad\mathrm{i}^{Rn}$ ($\mathrm{i} = 1, 2, 3$) correspond to the different methods for obtaining the relative adsorption. Note that this values are not corrected for the adsorbent mass.

[a] no *desorption measurement* → calculation of ad_2 and ad_3 not possible

very low temperatures, a non negligible value of adsorption is reached[11]. For the here shown measurements the approximation that helium is not adsorbed at all is perfectly valid.
Since the partial pressure of radon is basically zero, the sample is perfectly in the *Henry's region* (section 4.2.4), i.e. the adsorbed amount of radon increases linearly with the pressure. Hence the relative adsorption coefficient $ad\mathrm{i}^{Rn}$ ($\mathrm{i} = 1, 2, 3$) at a fixed temperature is expected to be constant, independently of the partial radon pressure.
Following the measuring process in section 4.3.2, the obtained results of radon adsorption measurements with the charcoal sample *Blücher 100050* at four different temperatures are summarized in table 4.7. The *relative adsorption coefficients* $ad\mathrm{i}^{Rn}$ correspond to the different methods to measure the relative adsorption of a single sample in one *cycle of measurement* as described before. The results are consistent within the errors. The relative adsorption coefficient extracted from the *adsorption measurement*, $ad1^{Rn}$, is used for further analysis. The two other coefficients, with their larger error due to systematics, are used as a cross-check and have not been measured in every cycle.
While almost all radon is adsorbed at 0 °C, the capability decreases quite fast with increasing temperature due to the additional kinetic energy of the adsorbate gas. As discussed in section 4.2.4, this correlation can be used to extract the isosteric heat of adsorption q for radon by fitting the temperature dependence of Henry's

[11] This property of helium is also commonly used for determination of an adsorbents total pore volume: the displacement of helium caused by an adsorbent, is compared to that of mercury, which can't penetrate into the adsorbents pores.

constant.

The isosteric heat of adsorption of radon

Henry's law generally relates the amount of gas being adsorbed (n_{ad}), to the gas pressure in the adsorption equilibrium (p) representing the amount of gas in the gas phase (n_{free}). This has been already introduced in equation 4.4. For examining the temperature dependence of a charcoal's adsorption capability, a modified relation is introduced

$$n_{ad}(T) = H(T) \cdot n_{free} \,. \tag{4.34}$$

The temperature dependence of the Herny-constant $H(T)$ is described with the *van t'Hoff* equation (e.g. [66]).

$$H(T) = H_0 \cdot e^{\frac{-q}{R\,T}} \,, \tag{4.35}$$

where q represents the isosteric heat of adsorption while H_0 is a model constant. By setting $n_{ad} = n_{tot} \cdot ad\mathrm{i}^{Rn}$ and $n_{free} = (1 - n_{tot}) \cdot ad\mathrm{i}^{Rn}$ in equation 4.34 and by making use of the *van t'Hoff* equation one obtains

$$ad\mathrm{i}^{Rn}(T) = \frac{H_0 \cdot e^{-\frac{q}{R\,T}}}{1 + H_0 \cdot e^{-\frac{q}{R\,T}}} \,. \tag{4.36}$$

By fitting this expression to the data in table 4.7, the isosteric heat of adsorption q for radon on the charcoal sample *Blücher 100050* can be extracted. The value fitted in figure 4.12 is

$$q_{Rn} = (40 \pm 1)\frac{\mathrm{kJ}}{\mathrm{mol}} \,.$$

No other values for the isosteric heat of adsorption of radon on activated carbon are available in literature. In [86] an estimation of $q_{Rn} = 17$ kJ/mol (4.01 kcal/mol) is given in the presence of N_2. The work of Gubeli and Stori (1954) is mentioned who obtains values between 29 kJ/mol (6.86 kcal/mol) and 33kJ/mol (7.82 kcal/mol) for nitrogen-radon mixtures.
Since xenon is very similar to radon also its value for the isosteric heat of adsorption on activated carbon found by [95] of 28 kJ/mol should be mentioned. All this values have been measured with different charcoal samples.

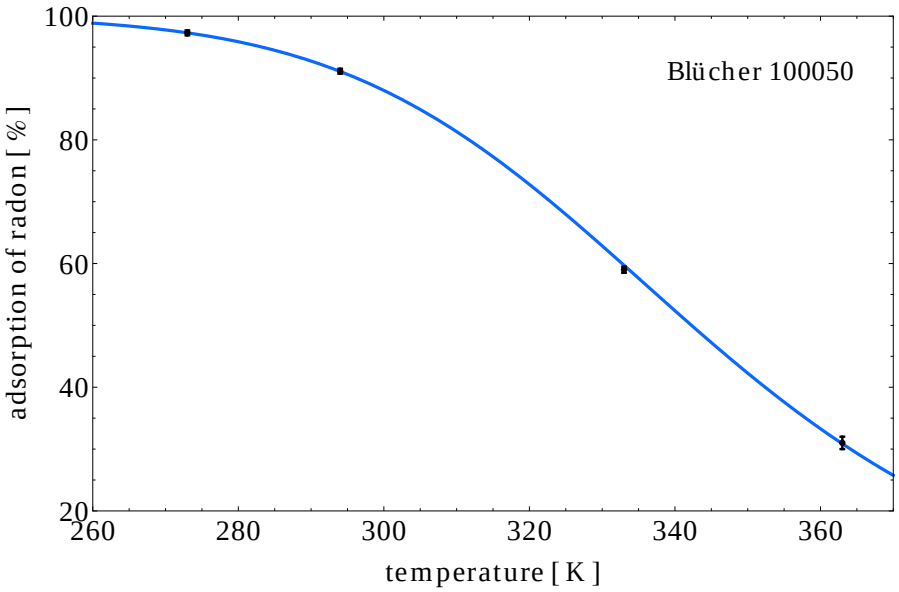

Figure 4.12: Summarized results of radon adsorption measurements of a helium-radon sample at four different temperatures. The temperature dependence of the adsorption is fitted according to equation 4.36. This allowes to extract the isosteric heat of adsorption for radon.

Henry's constant for radon

To obtain the Henry's constant H, introduced in Henry's law (equation 4.4), the adsoption pressure p is replaced by using the ideal gas law:

$$n_{ad} = H \cdot \frac{n_{free}\, R\, T}{V} \,, \tag{4.37}$$

where V labels here the volume in which contains the adsorption equilibrium $(V_{AD} + V_{CV})$ and T the temperature of the gas n_{free} in the gas phase. Since in the presented setup the water bath, used for adsorption measurements apart from room temperature, causes a gradient in the particle density, equation 4.37 is only used to calculate the Henr's constant at room temperature (H_{RT}). This is done by replacing n_{ad} and n_{free} which then results in[12]

$$H_{RT} = \frac{adi^{Rn}\, V}{(\,1 - adi^{Rn}\,)\; R\, T\, m} \,. \tag{4.38}$$

[12]Note that adi^{Rn} is not normalized to the adsorbents mass. Therefore m appears in the denominator of equation 4.37.

The obtained Henry's constant for radon adsorption at room temperature on the charcoal sample *Blücher 100050* is

$$H_{RT} = (2.7 \pm 0.2) \cdot 10^{-3} \, \frac{\text{mol}}{\text{Pa kg}}$$

With the extracted Henry's constant at room temperature and the known isosteric heat of adsorption it is possible to predict the value of $H(T)$ at other temperatures as well.

4.5.3 Xenon-radon mixture

In contrast to helium, xenon is expected to have a large impact on the radon adsorption capability of any adsorbent. While competitive adsorption of radon-xenon mixtures is not available in literature, results for xenon-krypton mixtures are published in [95]. In this work the influence of an increasing amount of xenon on the uptake of krypton by activated carbon is shown. In addition, the increasing suppression factor at higher temperatures is measured. The experimental results are then fitted with a two component adsorption model.
However, in case of the xenon-radon samples used in this work, the system is different since the partial pressure of the radon component is basically zero. As a result xenon adsorption can be treated with a single component model, feeling no influence of radon, while radon adsorption is, as the krypton adsorption in [95], expected to be strongly suppressed. This fact allows the analysis of single-component-adsorption of xenon and simultaneously its influence on the radon uptake of the charcoal.

Adsorption isotherms of xenon at different temperatures

In the measuring setup, the combination of pressure and activity measurement allows to obtain radon and xenon adsorption simultaneously. Since the partial pressure of radon is negligible, the setup allows to record single-component xenon isotherms. In this subsection, xenon isotherms of the charcoal sample *Blücher 100050* at different temperatures are measured.
Figure 4.13 shows a xenon isotherm at 60°C on *Blücher 100050* charcoal (the same sample as used in section 4.5.2) and table 4.8 the corresponding data. The amount of xenon adsorbed per unit mass of the studied charcoal is calculated using

$$n_{ad} = \frac{p_1 \, V_{CV} \, ad1^{Xe}}{m \, R \, T} \, . \tag{4.39}$$

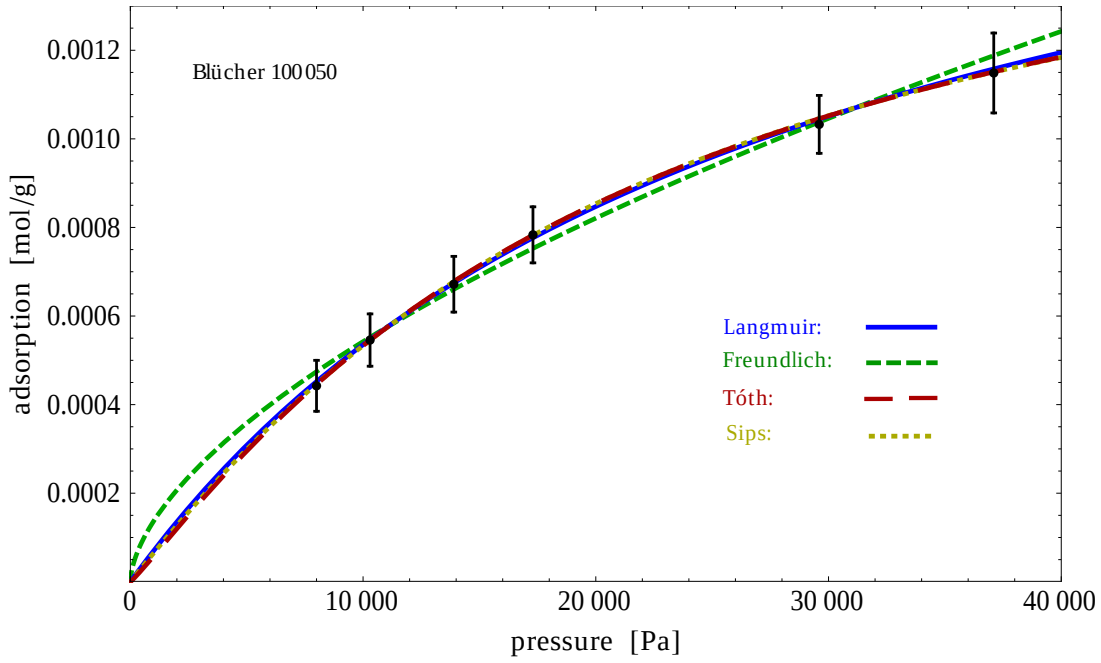

Figure 4.13: Xenon adsorption isotherm measured with $(0.0365 \pm 2) \cdot 10^{-4}$ g of the activated carbon *Blücher 100050* at 60°C. Data is fitted with various single component models introduced in section 4.2.4 (fit parameters are given in Table 4.9). Obviously the linear Henry's law is not valid anymore at higher pressures.

pressure [mbar]	**ad1$^{\mathbf{Xe}}$** [10^2]	**adsorption** [$10^{-4} mol/g$]
80	17 ± 3	4.4 ± 0.6
103	17 ± 2	5.5 ± 0.6
139	16 ± 2	5.5 ± 0.6
173	15 ± 1	7.8 ± 0.6
296	11.5 ± 0.8	10.3 ± 0.7
371	10.5 ± 0.9	11.5 ± 0.9

Table 4.8: Data of the xenon adsorption isotherm at 333 K shown at figure 4.13. For calculating the amount of adsorbed xenon equation 4.39 was used.

The derivation of this formula starts again with the relation $n_{ad} = n_{tot} \cdot ad1^{Xe}$. n_{tot}, on the other hand is calculated from the ideal gas law, using p_1 for pressure and V_{CV} as the samples volume. The combination of these two relations gives equation 4.39 after the mass normalization.
The shape of the isotherm clearly demonstrates that in the studied pressure region the xenon adsorption has left Henry's region (no linearity). It should be emphasized that Henry's constant was introduced in section 4.2.4 as the low-pressure limit of the single-component Langmuir-model. The experimental data is fitted with the four isotherm models introduced in section 4.2.4: Freundlich-, Langmuir-, Sips- and Tóth isotherm.
All models are in good agreement with data within the error which is, dominated by the error from the pressure measurement (see section 4.4.3), overestimated. Therefore also the empirical Freundlich model, which deviates from the other models in the low and high pressure range, cannot be excluded. The Sips and Tóth models were found to be almost identical, while the Langmuir model seems to diverge slightly from the other. This can also be seen in table 4.9 where the fit parameter of the models are given. Of particular interest is the monolayer capacity n_∞ of the charcoal. Sips and Tóth models agree with each other, while Langmuir shows a slightly higher n_∞.
The monolayer capacity was introduced as a temperature independent quantity, however, when analyzing the xenon isotherm at room temperature, a higher value of $n_\infty = (2.9 \pm 0.2) \cdot 10^{-3}$ mol/g, compared to $n_\infty = (2.03 \pm 0.04) \cdot 10^{-3}$ mol/g at 60°C, was extracted by applying the Langmuir model. A possible explanation is the lower kinetic energy of the adsorbed gas at lower temperatures. As a result the interaction of the xenon atoms is smaller and in total the adsorbent has a higher capacity. On the other hand the isotherm at room temperature in figure 4.14 seems to deviate from the fitted model at about 25 000 Pa (dashed line in 4.14). Such a type II isotherm is typical for adsorbents showing multilayer adsorption which could also explain a higher value for n_∞. In this scenario at a certain pressure the adsorption capability is increased due an additional xenon layer bound by already adsorbed xenon (dashed line in figure 4.14).
The monolayer capacity is a quality parameter for the charcols capability to adsorb xenon. However, in case of radon, where a high pressure range cannot be reached, other parameters like the isosteric heat of adsorption and Henry's constant are useful for the comparison of activated carbons.

Xenon adsorption on the other two charcoal samples has only been studied at one fixed temperature and pressure. Results are summarized at table 4.12 together with values for radon adsorption and discussed in the following section. Single component adsorption of xenon on activated carbon has been also studied in e.g. [96].

isotherm-	**fit parameter**		
model	$\mathbf{K_i}$ $[10^{-6}]$	$\mathbf{m_i}$	$\mathbf{n_\infty}$ $[10^{-3}$ mol/g$]$
Freundlich	2.2 ± 0.6	1.65 ± 0.08	-
Langmuir	36 ± 1	-	2.03 ± 0.04
Sips	16 ± 7	0.91 ± 0.04	1.8 ± 0.1
Tóth	2 ± 4	1.3 ± 0.2	1.7 ± 0.2

Table 4.9: Fit parameters of various isotherm models applied on the experimental data as shown in figure 4.13. Of particular interest is the monolayer capacity n_{mon}. While Sips and Tóth model agree very well, the value extracted from the Langmuir model is slightly higher.

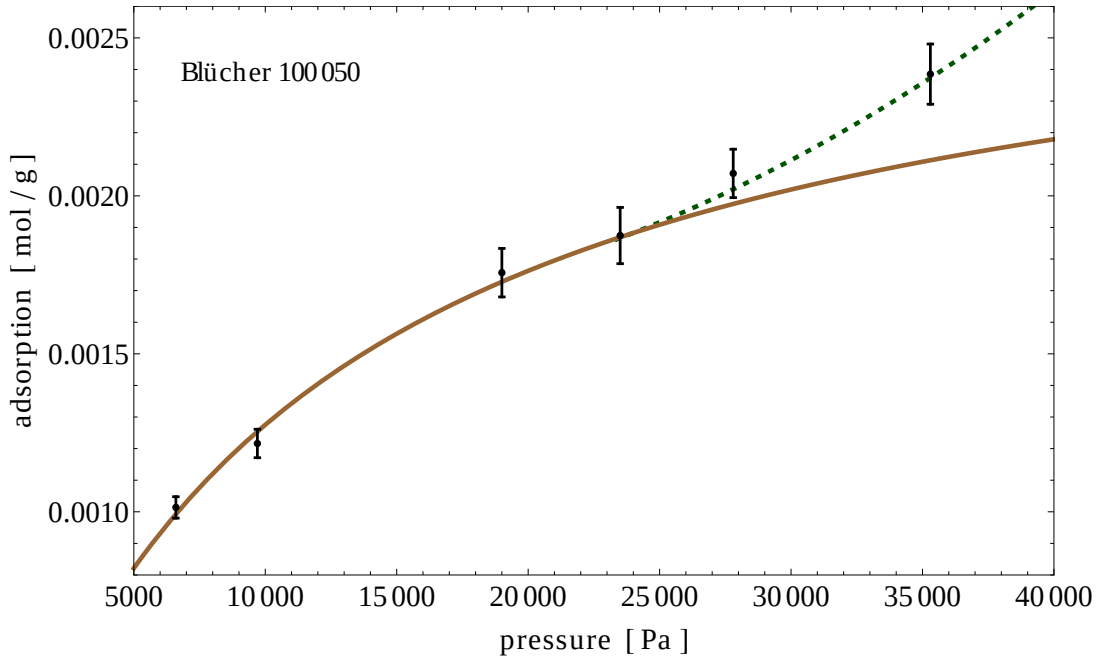

Figure 4.14: Data from xenon adsorption at room temperature. For the solid line monolayer adsorption has been assumed. The bend in data at about 27 000 Pa is propably due to start of multilayer adsorption. This results in a Type II isotherm (dashed line).

	relative adsorption $[10^2]^a$			**adsorption** $\left[10^{-3}\ \frac{\text{mol}}{\text{g}}\right]$
	$ad1^{Xe}$	$ad2^{Xe}$	$ad3^{Xe}$	
Blücher 100050	22.3 ± 0.4	22 ± 1	22 ± 2	2.04 ± 0.04
Blücher 100878	26.6 ± 0.3	26 ± 1	26 ± 2	2.35 ± 0.04
SHIRASAGI G2x4/6-1	24.1 ± 0.3	24 ± 1	23 ± 2	2.22 ± 0.03

Table 4.10: Measured relative adsorption coefficients for xenon at room temperature and a fixed adsorption pressure of 264 mbar. The values for the *absolute* adsorption have been calculated using equation 4.39 and $ad1^{Xe}$.

[a] Averaged values. Find all measurements in detail in appendix D.

Comparison of radon- and xenon-adsorption on charcoal samples

After defining and testing the experimental setup and process of measurement with the charcoal sample *Blücher 100050*, two further activated carbons (section 4.5.1) were studied. Since the radon uptake is related to the pressure of the sample (i.e. the partial pressure of xenon), adsorption-pressure and temperature needs to be kept constant for all measurements:

$$T = (294 \pm 1)\,\text{K}$$
$$P = (264 \pm 4)\,\text{mbar}$$

While the temperature was quite stable, it corresponds to the labs air condition, it was rather difficult to have the adsorption pressure constant. The sample has to reach this value when equilibrium is established, hence one has to prepare it in the first place by adding additional xenon as described in section 4.3.2.

Xenon-adsorption The results found for the xenon-adsorption on the three charcoal samples are summarized in table 4.10. All relative adsorption coefficients adi^{Xe} agree within the errors. However, only $ad1^{Xe}$ was used for further analysis. due to its small error.
The amount of xenon adsorbed per mass unit of the different charcoal samples is calculated using equation 4.39. The results are given in table 4.10 at the very right column. At the above fixed conditions for temperature and adsorption-pressure, the charcoal *Blücher 100878* shows the highest xenon adsorption. At room temperature already roughly 0.27 g of xenon are bound per gram carbon. *Blücher 100050* was found to have the lowest capacity while those of *SHIRASAGI*

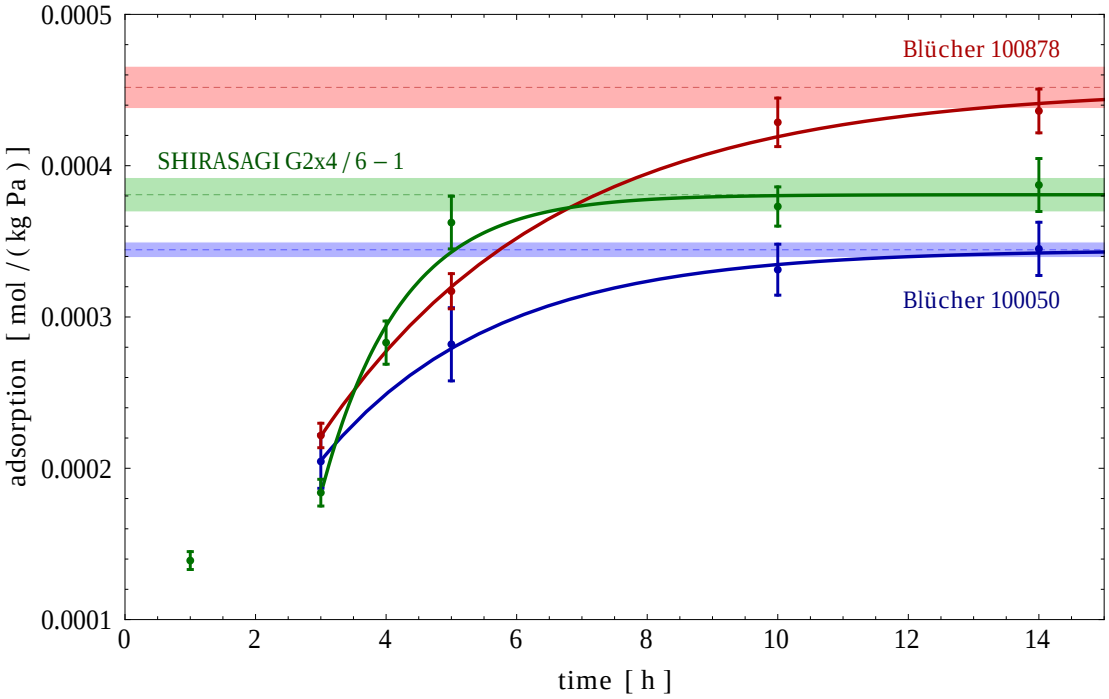

Figure 4.15: Development of Henry's constant for radon adsorption with the adsorption time (i.e. the contact time of the gas with the adsorbent). Data has been fitted with equation 4.40. The values for the fitted Henry's constant are listed in table 4.12.

G2x4/6-1 is inbetween. This is an important quantity for constructing the radon removal system since the xenon, bond by the activated carbon, needs to be replaced by additional xenon. Ongoing measurements of the xenon adsorption on *Blücher 100050* at -70°C show an adsorption of 0.7 g xenon per gramme adsorbent at a adsorption pressure of 200 mbar. This parameter is crucial for determining the size and consequently also the performance of the radon removal system for a fixed amount of available xenon.

While temperature and pressure of all measurements were kept fixed, the *adsorption time*, i.e. the contact time of adsorbent and adsorbate, was varied in a range of 1 to 14 hours. For the adsorption of xenon this had no influence at all, since the pressure was found to be stable after about 15 minutes. Hence xenon reaches adsorption equilibrium relatively fast.

Radon-adsorption Radon adsorption, in contrast to xenon, was found to depend strongly on the adsorption time. In figure 4.15 the radon adsorption capability of the three charcoal samples are given as a function of the contact time with the

	adsorption	**relative adsorption** $[10^2]$			$H_{264\,mbar}$
	[h]	$ad1^{Rn}$	$ad2^{Rn}$	$ad3^{Rn}$	$\left[10^{-4}\,\frac{\text{mol}}{\text{Pa kg}}\right]$
Blücher	3	44.3 ± 0.5	45 ± 1	45 ± 3	2.07 ± 0.08
100050	5	51.9 ± 0.5	53.1 ± 0.9	56 ± 3	2.8 ± 0.1
	10	56.9 ± 0.5	56.1 ± 0.9	54 ± 3	3.4 ± 0.1
	14	57.5 ± 0.7	57 ± 1	55 ± 3	3.5 ± 0.2
Blücher	3[a]	48.2 ± 0.5	-	-	2.2 ± 0.1
100878	5	57.1 ± 0.5	57.1 ± 0.9	57 ± 1	3.2 ± 0.1
	10	64.2 ± 0.5	64.3 ± 0.8	65 ± 4	4.3 ± 0.2
	14	64.7 ± 0.3	64.8 ± 0.8	65 ± 4	4.4 ± 0.2
SHIRASAGI	1[a]	35 ± 1	-	-	1.2 ± 0.1
G2x4/6-1	3[a]	41.6 ± 0.6	-	-	1.8 ± 0.1
	4[a]	52 ± 1	-	-	2.8 ± 0.2
	5	58.5 ± 0.4	58.6 ± 0.9	59 ± 3	3.6 ± 0.1
	10	59.1 ± 0.4	60.4 ± 0.9	64 ± 3	3.7 ± 0.1
	14	60.1 ± 0.4	59.5 ± 0.9	57 ± 3	3.9 ± 0.2

Table 4.11: Results of the radon adsorption measurements in detail. $ad\text{i}^{Rn}$ corresponds to the relative adsorption coefficient. In the very right column Henry's constant at coexisting xenon pressure of 264 mbar is calculated using $ad1^{Rn}$.

[a] no *desorption measurement* → calculation of ad_2^{Rn} and ad_3^{Rn} not possible

sample	$\mathbf{H_{264\,mbar}}\left[10^{-4}\,\frac{\text{mol}}{\text{Pa kg}}\right]$
Blücher 100050	3.44 ± 0.05
Blücher 100878	4.52 ± 0.14
SHIRASAGI G2x4/6-1	3.81 ± 0.12

Table 4.12: Fitted values for Henry's constant $\mathbf{H_{264\,mbar}}$.

activated carbon (i.e. adsorption time). Table D.1 contains the corresponding data. Since radon is in the low-pressure limit the linear Henry-model can be used to describe the adsorption. Due to the presence of xenon, however, the obtained Henry's constant is suppressed by about one order of magnitude and hence labelled as $H_{264\,mbar}$. This quantity, given in $\left[10^{-4}\,\frac{\text{mol}}{\text{Pa kg}}\right]$, is calculated from the measured relative adsorption coefficient $ad1^{Rn}$ using equation 4.38. Figure 4.15 and table D.1 reveal, that the adsorption equilibrium for radon is not reached before 5-10 hours adsorption time, in contrast to xenon. Assuming that the adsorption capability increases to a maximum, which depends on the amount of the present xenon/radon and the temperature, the dependence of the radon adsorption on the time can be fitted with a function representing limited growth

$$ad^{Rn}(t) = ad^{Rn}_{equi} - (ad^{Rn}_{equi} - ad^{Rn}_{0})\; e^{-\lambda\, t}\;. \tag{4.40}$$

ad^{Rn}_0 is the adsorption at the time $t = 0$, which has no accurate physical meaning here, and λ is the time constant. The fitted values for ad^{Rn}_{equi} are summarized in table 4.12. The ranking of the charcoals with regard to their capability to adsorb radon is the same as for xenon. *Blücher 100878* shows with an equilibrium Henry's constant of $H_{264\,mbar} = 4.4 \pm 0.2\ \left[10^{-4}\,\frac{\text{mol}}{\text{Pa kg}}\right]$ the highest radon adsorption. The capability of *SHIRASAGI G2x4/6-1* turns out to be approximately 16% lower, that of *Blücher 100050* about 24%.
Of particular interest is the comparison of the individual time developments. While the *Blücher* charcoals show quite similar behavior, *SHIRASAGI G2x4/6-1* has a much steeper slope. Data suggest that it reaches the actual adsorption equilibrium after approximately 5 hours, much faster than the other two charcoals. Furthermore, below 3 hours adsorption time its capability turned out to be even lower than that of *Blücher 100050*. This behavior is not fully understood yet and discussed in section 4.5.4.
The fit with equation 4.40 gives quite reasonable estimates for the final equilibrium adsorption ad^{Rn}_{equi} altough it is not based on a well motivated physical modell.

Latest measurements at rather short adsorption time (1 h in figure 4.15) show deviation from the fitted function. The behavior at relatively short times needs to be examined in future measurements.

Estimation for the performance of a 500 kg radon adsorption column

The results above can be used to compare the charcoal samples also in terms of the radon retention time T_{Rn} in an adsorption column. For an efficient radon removal system, high values for T_{Rn} are required since in that case the radon decays with high probability inside the column and not in the detector where it contributes to the background. In its current version, the radon column as planned for XENON1T contains in total about 500 kg activated carbon. As discussed in section 4.1, this column is integrated in the xenon purification loop. The LXe needs to be looped with about 100 SLPM to achieve the required level of purification[13]. Investigations of the influence of dynamics on Henry's constants as measured in a static system has been started. In [88] an experimental setup for measuring the radon retention time T_{Rn} for a charcoal trap and a xenon-radon gas sample is described. When cooling the trap, containing 25 g of *Blücher 100050* charcoal, to −70 °C, a retention time of $T_{Rn} = 331.0$ min has been measured at a flow of 0.14 SLPM and a xenon pressure of 200 mbar. As shown in [88], T_{Rn} can be used to determine Henry's constant by using the relation [88]

$$H(\phi, T) = \frac{\phi\, T_{Rn} - V}{R\, T\, m} \,, \tag{4.41}$$

where V stands for the total volume of the circulation loop, ϕ for the gas flow and m is the adsorbent mass. They obtain at −70 °C a Henry's constant of $H(\phi, T) = (10.7 \pm 0.4) \cdot 10^{-4}$ mol Pa^{-1} kg^{-1}, a value 3 times larger than the equilibrium $H_{264\,mbar}$, measured in this work for the same charcoal at room temperature (see table D.1).
Equation 4.41 can be used to compare the different charcoal samples, measured in section 4.5.3, also in terms of T_{Rn}, assuming a 500 kg radon column and a flow of 100 SLPM. Since $(\phi \cdot T_{Rn}) \gg V$ is usually valid, equation 4.41 can be written, independently from the systems volume, as

$$H(\phi, T) = \frac{\phi\, T_{Rn}}{R\, T\, m} \,. \tag{4.42}$$

The obtained results for Henry's constants measured in the adsorption equilibrium are given in table 4.5.3. For the activated carbon with the highest equilibrium adsorption, *Blücher 100878*, a retention time of already T_{Rn}=3.75 days is obtained

[13] To remove electronegative impurities from the LXe target the xenon needs to be purified.

	Blücher 100050	*Blücher 100878*	*SHIRASAGI*
T_{Rn} [d]	2.98	3.75	3.32
ads. Xe [kg]	134	154	145

Table 4.13: Retention times T_{Rn} and the amount of adsorbed xenon, estimated for a 500 kg charcoal column and the equilibrium Henry's constants of the different charcoal samples measured at room temperature (see table D.1 and table 4.10 respectively).

at room temperature, which is close to the ^{222}Rn half life of 3.82 days. For an estimation of the amount of xenon adsorbed in a 500 kg radon column, the adsorption measurements given in table 4.10 are used. In case of *Blücher 100878*, even at room temperature, 154 kg xenon are bond inside the column.
It should be noted that the radon removal system is planned to be operated at lower temperatures than the here presented room temperature. While the efficiency of the system will increase at lower temperatures (in terms of a larger T_{Rn}), it has to be considered that the amount of xenon, required for detector operation, increases due to adsorption as well.

4.5.4 Summary and discussion

In section 4.5.2, a helium-radon mixture is used for measuring the single-component radon adsorption since helium, in very good approximation, is not adsorbed at all. For the charcoal sample *Blücher 100050*, the *relative adsorption coefficient* at various temperatures is determined. By fitting the temperature dependence of $ad\mathrm{i}^{Rn}$ ($\mathrm{i} = 1, 2, 3$), the *isosteric heat of adsorption* of radon is extracted. For the activated carbon *Blücher 100050* a value of $q = 40 \pm 1$ kJ/mol was found. The obtained Henry's constant for radon adsorption at room temperature is $H_{RT} = (2.7 \pm 0.2) \cdot 10^{-3} \frac{\mathrm{mol}}{\mathrm{Pa\ kg}}$.

In section 4.5.3, the competitive adsorption of a radon-xenon mixture on different charcoal samples is investigated. The adsorption isotherms of xenon on *Blücher 100050* are presented. Since the partial pressure of radon in the gas mixture is negligible, the obtained results apply for single-component adsorption. The xenon isotherms are fitted with the *Langmuir-model* which allowes to obtain n_∞, the total number of adsorption sites in this model. A value of $n_\infty = (2.03 \pm 0.04) \cdot 10^{-3}$ mol/g has been found.

Then the radon adsorption in the presence of xenon (264 mbar partial xenon pressure) on three charcoal samples (see table 4.6) is measured at room temperature. Henry's constant obtained for *Blücher 100050*, the same sample as used for the helium-radon mixture, is $H_{264\,mbar} = (3.44 \pm 0.05) \cdot 10^{-4}\,\mathrm{mol\,Pa^{-1}\,kg^{-1}}$ and the lowest of all charcoal samples. Henry's constant of *Blücher 100878* has the highest value of $H_{264\,mbar} = (4.52 \pm 0.14) \cdot 10^{-4}\,\mathrm{mol\,Pa^{-1}\,kg^{-1}}$ while for *SHIRASAGI G2x4/6-1* $H_{264\,mbar} = (3.1 \pm 0.12) \cdot 10^{-4}\,\mathrm{mol\,Pa^{-1}\,kg^{-1}}$ is found.

The most interesting result is that it takes for both *Blücher* charcoals more than 10 hours until the adsorption equilibrium is reached. In case of *SHIRASAGI G2x4/6-1* it is reached in almost half of the time. A possible explanation is the finite diffusion coefficient of radon in xenon. When the xenon-radon mixture gets into contact with the adsorbent, only the radon in the near sourrounding gets adsorbed. The remaining radon in the gas phase is spread all over the volume and needs to diffuse to the adsorbent to get adsorbed.
Since a difference in the time development between the charcoal samples has been found, diffusion is probably not the only process which has to be considered to explain this behavior. At the beginning of the measurement, xenon probably occupies most of the adsorption sites of the activated carbon due to its much larger abundance. Depending on the binding energy, expressed by the isosteric heat of adsorption, and the kinetic energy, the adsorbed atoms wont stay adsorbed but will be released again after some time. This fluctuation of adsorption and desorption can lead to the observed time dependence of radon adsorption since the initial adsorbed xenon gets exchanged by the tighter bond radon atoms. Depending on the isosteric heat of adsorption of radon and xenon for a particular activated carbon sample the resulting time dependence can show a different slope.
Furthermore the pore structure and pore distribution might can have a big influence. It is thought that relatively wide pores are necessary for transporting the radon to finer pores where it finally gets adsorbed. Interesting in this context is that *Blücher 100878* has the smallest micropore volume of all measured charcoals and also the total pore volume is much smaller than that of *Blücher 100050*. Nevertheless it shows the highest adsorption capability. This indicates that the micropore structure of the other two samples, particularly of *Blücher 100050*, is not accessible for the gas. Correlations between the pore distribution of the samples, given in table 4.6, and the time until the adsorption equilibrium is reached, have not been found.
For the selection of an adsorbent for a radon removal system this dependence of the adsorption capability on contact time can be crucial.
In XENON1T it is planned to circulate the xenon with a flow of $\sim$100 SLPM through the purification system. Hence, an adsorbent with a high adsorption capability after short contact times should be selected, even if the equilibrium

adsorption is worse compared to others. Certainly, the time dependence needs further investigation.

The obtained results for the radon adsorption can be used to estimate the radon retention time T_{Rn} for the circulation through an adsorbent column. Assuming a column containing 500 kg charcoal with a Henry's constant as measured for *Blücher 100878* in the static setup at room temperature, a retention time of T_{Rn}=3.75 days is obtained for a flow of 100 SLPM. That is, the reduction factor of such the assumed activated carbon column would be approximately 0.5 at room temperature. The actual operation temperature, however, is planned to be lower than room temperature to achieve a higher reduction factor.

Chapter 5

Summary and conclusions

The search for dark matter is one of the most interesting questions in today's experimental particle physics. Although several evidences have been seen, the identity of dark matter is still a mystery which is aimed to be solved by experiments all over the world following different strategies for detection. The XENON project is one of the leading experiments for the direct detection of WIMP dark matter, setting the most stringent limits on the cross section for elastic WIMP-nucleus scattering over a wide range of dark matter particle masses. Since dark matter search deals with extremely low event rates, background reduction and background/signal discrimination are the most challenging tasks. The background is classified by its origin in neutron and electromagnetic (γ, β) background. The so-called intrinsic background from the radioactive isotopes ^{85}Kr and ^{222}Rn is a major challenge, as it cannot be reduced by shielding. Due to the absence of sources inside the detector, the LXe can be purified from ^{85}Kr by distillation before it is filled into the cryostat. ^{222}Rn, in contrast, is permanently produced by the radioactive decay of ^{226}Ra inside the detector materials and can emanate into the target material which makes purification more challenging. In this work the radon induced background has been analyzed and measurements for a radon removal system based on its adsorption on activated carbon are presented.

The decay of ^{222}Rn and its progenies until the stable isotope ^{206}Pb have been simulated in LXe. To do so, a dark matter detector with a LXe target of $\sim$1 ton, following the XENON1T detector geometry, has been simulated using the Geant4 toolkit. The deposited energy spectra of the radioactive β-decays of the radon progenies have been recorded and analyzed. Furthermore the simulation has been used to determine the contributions of the single daughter isotopes to the overall radon induced internal background. Since the α particles in the decay chain are high energetic, the background is dominated by the β-decaying daughter isotopes.

The simulation identified ^{214}Pb as the isotope which contributes most to the radon induced background in LXe detectors assuming a homogeneous distribution of all isotopes inside the detector.

Radon can be a limiting factor on the sensitivity of future dark matter detectors like XENON1T. Thus, its concentration in the LXe target needs to be controlled. Since radon permanently emanates from the detector materials, a removal system has to work permanently as well, i.e. the xenon has to be purified during detector operation. A solution based on adsorption has been presented in this work. In this approach the xenon, contaminated with radon, is flushed through an adsorbent trap. Due to different adsorption coefficients of radon and xenon, the radon should be caught for several half-lifes in the trap while xenon flows with rather low resistance through the adsorbent trap. Consequently, the radon most likely decays inside the trap and not in the detector. Certainly, the efficiency of this system strongly depends on the adsorbents capability to adsorb radon in the presence of xenon.
To measure the radon adsorption on an adsorbent sample, an experimental setup, introduced for the first time by [81], has been developed further. Its central element is a Lucas-Cell, an α-scintillation counter, to detect the radon activity before and after the adsorption process. With this setup the equilibrium adsorption of a helium-radon gas mixture on an activated carbon sample has been measured. Since helium in good approximation is not adsorbed at all, this measurement allows to study the radon adsorption without any suppression of other gas components due to competitive adsorption. From the temperature dependence of the adsorption capability the isosteric heat of adsorption, a quantity representing the bonding strength between radon and a particular activated carbon, has been determined. For the activated carbon *Blücher 100050* [89] it has been found to be $(40 \pm 1)\frac{\mathrm{kJ}}{\mathrm{mol}}$. The Henry's constant, a measure for an adsorbent's adsorption capability, was measured to be $H_{RT} = (2.7 \pm 0.2) \cdot 10^{-3}\ \frac{\mathrm{mol}}{\mathrm{Pa\ kg}}$ for radon adsorption at room temperature for the same charcoal sample.

For a later application of the radon removal system in XENON1T, the radon adsorption in presence of xenon has been measured. Using a xenon-radon mixture as a gas sample, the adsorption of radon and xenon could be obtained simultaneously with the Lucas-Cell and a manometer respectively. The xenon adsorption isotherms of the activated carbon *Blücher 100050* has been determined for different temperatures. These can successfully be described by the Langmuir, Sips and Tóth models [77]. For the comparison of three different activated carbon samples, the adsorption of radon was measured at a fixed temperature (room temperature) and a fixed xenon pressure (264 mbar). While in this competitive two component adsorption process the equilibrium of xenon adsorption is reached within 15 min-

utes, it took more than 10 hours until the measured charcoal samples showed their full capacity in terms of radon adsorption. This behavior is thought to originate from the finite diffusion length of radon in xenon, but also from the competitive adsorption of the much more abundant xenon. The adsorption capacity as a function of the adsorption time could be described by a function representing limited growth. Of particular interest for a later application in a radon removal system is the significant variation of the fitted time constants of the activated carbon samples. In a dynamic system, the equilibrium adsorption might not be the crucial parameter, but rather the performance of an adsorbent after short contact times. The charcoal *SHIRASAGI G2x4/6-1* was found to reach its adsorption equilibrium faster than the other two Blücher charcoal samples. The highest radon adsorption capability at adsorption equilibrium, however, was measured for the sample *Blücher 100878* with $H_{264\,mbar} = (4.52 \pm 0.14)\,10^{-4}\,\mathrm{mol\,Pa^{-1}\,kg^{-1}}$ (264 mbar xenon pressure at room temperature). The origin of the time dependence of the radon adsorption but also the capability of the activate carbon samples in a dynamic system needs to be further investigated.

The construction phase of the XENON1T detector will start this year (2013), first data taking is planned in 2015. It is aimed for a background reduction by a factor 100 compared to XENON100. This should be reached due to careful material selection and dedicated purification methods including the radon removal system under investigation in this work. The presented experimental setup allows to characterize adsorbents, due to their ability to adsorb radon in the presence of xenon. Amongst others, based on this measurement the most appropriate adsorbent for the radon removal system can be selected in order to reach the challenging task of a radon contamination below μBq/kg LXe in the target of XENON1T.

Appendices

Appendix A

Cosmological parameters

In the standard model of cosmology the expansion of the universe is described by the time dependent *cosmic scale factor* $a(t)$. By definition the current value at the reference time t_0 is $a(t_0) = 1$. The *Hubble parameter* defined as

$$H(t) \equiv \frac{\dot{a}(t)}{a(t)} \tag{A.1}$$

is the rate of expansion. The present Hubble parameter is $H_0 = 70.0 \pm 2.2$ $\mathrm{km\,s^{-1}\,Mpc^{-1}}$ or in its dimesionless form $h \equiv H_0/(100\,\mathrm{km\,s^{-1}\,Mpc^{-1}}) = 0.700 \pm 0.022$. The expansion of an isotropic, homogeneous model of our universe is described by the *Friedmann equation*

$$H^2(t) = \left(\frac{\dot{a}(t)}{a(t)}\right) = \frac{8\,\pi\,G}{3}\,\rho_{tot}(t) - \frac{k}{a^2}\,, \tag{A.2}$$

where G is the gravitational constant and k describes the spatial curvature[1]. ρ_{tot} corresponds to the total average energy density in the universe. Equation A.2 makes clear that for a flat universe (i.e. $k = 0$) the critical energy density

$$\rho_c \equiv \frac{3\,H_0^2}{8\,\pi\,G} \tag{A.3}$$

is required. The total energy density ρ_{tot} itself is composed of different contributions ρ_i (matter, radiation, vacuum energy). It is common to express this contributions relative to ρ_c,

$$\Omega_i \equiv \frac{\rho_i}{\rho_c}\,. \tag{A.4}$$

[1] $k = 0 \rightarrow$ flat universe, $k = -1 \rightarrow$ open universe, $k = 1 \rightarrow$ closed universe

After introduction of these parameters the Friedmann equation A.2 can be written as

$$\sum_i \frac{H_0^2}{H^2}\,\Omega_i - 1 = \frac{k}{a^2\,H^2}\ . \tag{A.5}$$

The contributions of baryonic matter Ω_b, of cold dark matter Ω_{CDM} and of dark energy Ω_Λ are the energy density parameters in the ΛCDM-model.

Appendix B

Thermal relic density

In the early universe WIMPs and all other particles are in thermal equilibrium with the cosmic soup, i.e. the creation and annihilation processes are equally efficient. If m_χ is the mass of a WIMP candidate χ, the number density of this particle in the thermal equilibrium is given by

$$n_\chi^{eq} = g_\chi \left(\frac{m_\chi T}{2\,\pi} \right)^{\frac{3}{2}} \, e^{-\frac{m_\chi}{T}} \, , \tag{B.1}$$

where g_χ stands for the degrees of freedom of χ and T the temperature. As the universe cools down its temperature at some point drops below $T < m_\chi$. Looking at above equation B.1 one can see that now the number density of χ becomes Boltzmann suppressed. It decreases exponentially with the temperature since due the lower thermal energy the annihilation processes dominate. On the other hand, the expansion of the universe causes dilution of the particle densities with the result that interactions happen less frequent till finally the particles do not find each other to annihilate. At some temperature T_F they *freeze out* with a certain relic density. It can be calculated by describing the competing effects of creation, annihilation and diluting with the Boltzmann equation

$$\frac{dn_\chi}{dt} = -3\,H\,n_\chi - \langle \sigma\, v \rangle (n_\chi^2 - (n_\chi^{eq})^2) \, , \tag{B.2}$$

where n_χ is the WIMP number density, H the Hubble parameter and $\langle \sigma\, v \rangle$ the product of the thermal average of the annihilation cross section with the particles relative velocity.
Following the deviation in [4] and [12], the order of magnitude of the relic density can be estimated by

$$\Omega_\chi h^2 \approx \frac{3 \cdot 10^{-27}\,\mathrm{cm^3 s^{-1}}}{\langle \sigma\, v \rangle} \, . \tag{B.3}$$

Equation B.3 holds for any dark matter candidate and needs to be fulfilled of any proposed dark matter particle.

Appendix C

Error determination

In this appendix, the formulas for the error calculation of the obtained results are given. The single contributions to the total error are discussed in section 4.4.3.

C.1 Relative adsorption coefficients

The relative adsorption coefficient $ad1^{Rn/Xe}$ has the smallest error compared to $ad2^{Rn/Xe}$ and $ad3^{Rn/Xe}$ and is therefore treated as the main result (see section 4.4.3).

C.1.1 Radon

$$
\begin{aligned}
&\left(\Delta ad1^{Rn}\right)^2 = \\
&\frac{e^{2\lambda_{Rn} t_{ad}} (1+V_{CV})^{2a} \left(\Delta V_{AD}^2 f_{corr}^2 A_{act}^2 A_{ad1}^2 V_{CV}^2 + \Delta A_{ad1}^2 f_{corr}^2 A_{act}^2 V_{CV}^2 (V_{AD}+V_{CV})^2\right)}{f_{corr}^4 A_{act}^4 V_{CV}^4} \\
&+ \frac{e^{2\lambda_{Rn} t_{ad}} (1+V_{CV})^{2a} \left(\Delta A_{act}^2 f_{corr}^2 A_{ad1}^2 V_{CV}^2 (V_{AD}+V_{CV})^2\right)}{f_{corr}^4 A_{act}^4 V_{CV}^4} \\
&+ \frac{e^{2\lambda_{Rn} t_{ad}} (1+V_{CV})^{2a} \left(\Delta f_{corr}^2 A_{act}^2 A_{ad1}^2 V_{CV}^2 (V_{AD}+V_{CV})^2\right)}{f_{corr}^4 A_{act}^4 V_{CV}^4} \\
&+ \frac{\Delta V_{CV}^2 e^{2\lambda_{Rn} t_{ad}} A_{ad1}^2 (1+V_{CV})^{-2+2a} \left(a V_{CV}^2 + V_{AD} (-1+(-1+a) V_{CV})\right)^2}{f_{corr}^2 A_{act}^2 V_{CV}^4}
\end{aligned}
\tag{C.1}
$$

The obtained error refers to equation 4.31.

C.1.2 Xenon

$$\left(\Delta ad1^{Xe}\right)^2 =$$

$$\frac{\Delta V_{AD}^2\, p_2^2}{f_{corr}^2\, p_1^2\, V_{CV}^2} + \frac{\Delta p^2\, (V_{AD}+V_{CV})^2}{f_{corr}^2\, p_1^2\, V_{CV}^2} + \frac{\Delta p^2\, p_1^2\, (V_{AD}+V_{CV})^2}{f_{corr}^2\, p_1^4\, V_{CV}^2}$$

$$+ \frac{\Delta f_{corr}^2\, p_1^2\, (V_{AD}+V_{CV})^2}{f_{corr}^4\, p_1^2\, V_{CV}^2} + \Delta V_{CV}^2 \left(-\frac{p_1}{f_{corr}\, p_1\, V_{CV}} + \frac{p_1\, (V_{AD}+V_{CV})}{f_{corr}\, p_1\, V_{CV}^2}\right)^2 \tag{C.2}$$

The obtained error refers to equation 4.28.

C.2 Radon Henry-constant

The error of the Henry-constant H_{RT} for radon adsorption at room temperature, as given by equation 4.38, is calculated by

$$(\Delta H_{RT})^2 =$$

$$\frac{(ad1^{Rn})^2\, (\Delta V_{AD}+\Delta V_{CV})^2}{(1-ad1^{Rn})^2\, m^2\, R^2\, T^2} + \frac{(ad1^{Rn})^2\, \Delta T^2 (V_{AD}+V_{CV})^2}{(1-ad1^{Rn})^2\, m^2\, R^2\, T^4} + \frac{(ad1^{Rn})^2 \Delta m^2\, (V_{AD}+V_{CV})^2}{(1-ad1^{Rn})^2\, m^4\, R^2\, T^2}$$

$$+ (\Delta ad1^{Rn})^2 \left(\frac{(V_{AD}+V_{CV})}{(1-ad1^{Rn})\, m\, R\, T} + \frac{ad1^{Rn}(V_{AD}+V_{CV})}{(1-ad1^{Rn})^2\, m\, R\, T}\right)^2 . \tag{C.3}$$

C.3 Xenon adsorption

The error for the amount of adsorbed xenon (equation 4.39) is given by

$$\left(\Delta n_{ad}^{Xe}\right)^2 =$$

$$\frac{\Delta T^2\, p_2^2\, p_1^2\, V_{CV}^2}{m^2\, R^2\, T^4} + \frac{\Delta V_{CV}^2\, p_2^2\, p_1^2}{m^2\, R^2\, T^2} + \frac{\Delta p^2\, p_2^2\, V_{CV}^2}{m^2\, R^2\, T^2} + \frac{\Delta p^2\, p_1^2\, V_{CV}^2}{m^2\, R^2\, T^2} + \frac{\Delta m^2\, p_2^2\, p_1^2\, V_{CV}^2}{m^4\, R^2\, T^2} . \tag{C.4}$$

Appendix D

Summary of xenon adsorption measurements

	adsorption	**relative adsorption** $[10^2]$		
	[h]	$ad1^{Xe}$	$ad2^{Xe}$	$ad3^{Xe}$
Blücher	3	22.2 ± 0.7	22.8 ± 0.9	21 ± 2
100050	5	22.2 ± 0.7	22.8 ± 0.9	21 ± 2
	10	22.3 ± 0.7	23.3 ± 0.9	22 ± 2
	14	23.3 ± 0.9	23 ± 1	22 ± 2
Blücher	3^a	26.2 ± 0.7	–	–
100878	5	26.5 ± 0.7	26 ± 1	25 ± 2
	10	26.5 ± 0.7	26 ± 1	26 ± 2
	14	27.2 ± 0.7	26 ± 1	–
SHIRASAGI	1^a	24.0 ± 0.7	–	–
G2x4/6-1	3^a	24.5 ± 0.7	–	–
	4^a	24.2 ± 0.7	–	–
	5	24.1 ± 0.7	23 ± 1	23 ± 2
	10	24.5 ± 0.7	24 ± 1	23 ± 2
	14	24.5 ± 0.7	24.4 ± 0.9	22 ± 2

Table D.1: Relative adsorption coefficients obtained for xenon at 264 mbar adsorption pressure and room temperature.

[a] no *desorption measurement* → calculation of ad_2^{Xe} and ad_3^{Xe} not possible

Bibliography

[1] F. Zwicky. Spectral displacement of extra galactic nebulae. *Helv. Phys. Acta.*, 6, 1933.

[2] K. A. Olive. Tasi lectures on dark matter. *arXiv:astro-ph/0301505*, 2003.

[3] J. L. Feng. Dark matter candidates from particle physics and methods of detection. *arXiv:1003.0904 [astro-ph.CO]*, 2010.

[4] G. Bertone, D. Hooper, and J. Silk. Particle dark matter: evidence, candidates and constraints. *Phys. Rept.*, 405, 2005.

[5] K. Garrett and G. Duda. Dark matter: A primer. *arXiv:1006.2483 [hep-ph]*, 2011.

[6] K. G. Begeman, A. H. Broeils, and R. H. Sanders. Extended rotation curves of spiral galaxies: Dark haloes and modified dynamics. *Mon. Not. Roy. Astron. Astrophys. J.*, 638, 1991.

[7] D. Clowe et al. A direct empirical proof of the existence of dark matter. *Astrophys. J.*, 648, 2006.

[8] D. Scott and G.F. Smoot. Cosmic Microwave Background (2012 Particle Data Group mini-review). 2011.

[9] George F. Smoot, C.L. Bennett, A. Kogut, E.L. Wright, J. Aymon, et al. Structure in the COBE differential microwave radiometer first year maps. *Astrophys.J.*, 396:L1–L5, 1992.

[10] G. Hinshaw, D. Larson, E. Komatsu, D.N. Spergel, C.L. Bennett, et al. Nine-Year Wilkinson Microwave Anisotropy Probe (WMAP) Observations: Cosmological Parameter Results. 2012.

[11] Brian Fields and Subir Sarkar. Big-Bang nucleosynthesis (2006 Particle Data Group mini-review). 2006.

[12] Gerard Jungman, Marc Kamionkowski, and Kim Griest. Supersymmetric dark matter. *Phys.Rept.*, 267:195–373, 1996.

[13] Dan Hooper and Stefano Profumo. Dark matter and collider phenomenology of universal extra dimensions. *Phys.Rept.*, 453:29–115, 2007.

[14] Dan Hooper. TASI 2008 Lectures on Dark Matter. pages 709–764, 2009.

[15] Riccardo Catena and Piero Ullio. A novel determination of the local dark matter density. *JCAP*, 1008:004, 2010.

[16] J.D. Lewin and P.F. Smith. Review of mathematics, numerical factors, and corrections for dark matter experiments based on elastic nuclear recoil. *Astropart.Phys.*, 6:87–112, 1996.

[17] Felix Kahlhoefer. Sensitivity of liquid xenon detectors for low mass dark matter. Master's thesis, University of Heidelberg, 2010.

[18] Joachim Kopp, Thomas Schwetz, and Jure Zupan. Global interpretation of direct Dark Matter searches after CDMS-II results. *JCAP*, 1002:014, 2010.

[19] E. Aprile et al. (XENON100 Collaboration). Limits on spin-dependent WIMP-nucleon cross sections from 225 live days of XENON100 data. 2013.

[20] Laura Baudis. Direct dark matter detection: the next decade. *Phys.Dark Univ.*, 1:94–108, 2012.

[21] E. Armengaud and others (The EDELWEISS Collaboration). Final results of the EDELWEISS-II WIMP search using a 4-kg array of cryogenic germanium detectors with interleaved electrodes. *Phys.Lett.*, B702:329–335, 2011.

[22] Z. Ahmed and others (The CDMS-II Collaboration). Dark Matter Search Results from the CDMS II Experiment. *Science*, 327:1619–1621, 2010.

[23] G. Angloher, M. Bauer, I. Bavykina, A. Bento, C. Bucci, et al. Results from 730 kg days of the CRESST-II Dark Matter Search. *Eur.Phys.J.*, C72:1971, 2012.

[24] K. Abe et al. (The XMASS Collaboration). Radon removal from gaseous xenon with activated charcoal. *Nuclear Instruments and Methods in Physics Research A*, 2012.

[25] D. Yu. Akimov, H.M. Araujo, E.J. Barnes, V.A. Belov, A. Bewick, et al. WIMP-nucleon cross-section results from the second science run of ZEPLIN-III. *Phys.Lett.*, B709:14–20, 2012.

[26] Alex Wright for the DarkSide Collaboration. The DarkSide Program at LNGS. *arXiv:1109.2979 [physics.ins-det]*, 2011.

[27] E. Aprile et al. (XENON100 Collaboration). The xenon100 dark matter experiment. *Astropart. Phys.*, 35:573–590, 2012.

[28] S. Archambault and others (The PICASSO Collaboration). Constraints on Low-Mass WIMP Interactions on ^{19}F from PICASSO. *Phys.Lett.*, B711:153–161, 2012.

[29] M. Felizardo, T.A. Girard, T. Morlat, A.C. Fernandes, A.R. Ramos, et al. Final Analysis and Results of the Phase II SIMPLE Dark Matter Search. *Phys.Rev.Lett.*, 108:201302, 2012.

[30] E. Behnke and others (The COUPP Collaboration). First Dark Matter Search Results from a 4-kg CF_3I Bubble Chamber Operated in a Deep Underground Site. *Phys.Rev.*, D86:052001, 2012.

[31] R Bernabei, P Belli, F Cappella, V Caracciolo, R Cerulli, C J Dai, A d'Angelo, A Di Marco, H L He, A Incicchitti, X H Ma, F Montecchia, X D Sheng, R G Wang, and Z P Ye. Dama/libra results and perspectives. *Journal of Physics: Conference Series*, 375(1):012002, 2012.

[32] C.E. Aalseth et al. Results from a Search for Light-Mass Dark Matter with a P-type Point Contact Germanium Detector. *Phys.Rev.Lett.*, 106:131301, 2011.

[33] W.B. Atwood et al. The Large Area Telescope on the Fermi Gamma-ray Space Telescope Mission. *Astrophys.J.*, 697:1071–1102, 2009.

[34] R. Abbasi et al. (The IceCube Collaboration). Multiyear search for dark matter annihilations in the sun with the amanda-ii and icecube detectors. *Phys.Rev.*, D85, 2012.

[35] V. Barger, Wai Yee Keung, D. Marfatia, and G. Shaughnessy. PAMELA and dark matter. *Phys.Lett.*, B672:141–146, 2009.

[36] Patrick J. Fox, Roni Harnik, Joachim Kopp, and Yuhsin Tsai. Missing Energy Signatures of Dark Matter at the LHC. *Phys.Rev.*, D85:056011, 2012.

[37] Howard Baer and Xerxes Tata. Dark matter and the LHC. 2008.

[38] E. Aprile et al. (XENON10 Collaboration). First results from the xenon10 dark matter experiment at the gran sasso national laboratory. *Phys. Rev. Lett.*, 100:021303, Jan 2008.

[39] E. Aprile et al. (XENON100 Collaboration). Dark matter results from 225 live days of xenon100 data. *arXiv:1207.5988v1 [astro-ph.CO]*, 2012.

[40] WArP Collaboration. *The WArP Programme*. PhD thesis, http://warp.lngs.infn.it/papers/proposal.pdf.

[41] M. Haranczyk et al. The ArDM experiment. 2010.

[42] E. Aprile and T. Doke. Liquid Xenon Detectors for Particle Physics and Astrophysics. *Rev.Mod.Phys.*, 82:2053–2097, 2010.

[43] Kaixuan Ni and Laura Baudis. Direct dark matter searches with cdms and xenon. *Advances in Space Research*, 41(12):2019 – 2023, 2008.

[44] Andrew Fowlie, Malgorzata Kazana, Kamila Kowalska, Shoaib Munir, Leszek Roszkowski, et al. The CMSSM Favoring New Territories: The Impact of New LHC Limits and a 125 GeV Higgs. *Phys.Rev.*, D86:075010, 2012.

[45] O. Buchmueller, R. Cavanaugh, A. De Roeck, M.J. Dolan, J.R. Ellis, et al. Higgs and Supersymmetry. *Eur.Phys.J.*, C72:2020, 2012.

[46] C. Strege, G. Bertone, D.G. Cerdeno, M. Fornasa, R. Ruiz de Austri, et al. Updated global fits of the cMSSM including the latest LHC SUSY and Higgs searches and XENON100 data. *JCAP*, 1203:030, 2012.

[47] E. Aprile et al. (XENON100 Collaboration). Analysis of the xenon100 dark matter search data. *arXiv:1207.3458 [astro-ph.IM]*, 2012.

[48] E. Aprile et al. (XENON1T Collaboration). The xenon1t dark matter search experiment. *arXiv:1206.6288v1 [astro-ph.IM]*, June 2012.

[49] E. Aprile et al. (XENON1T Collaboration). Xenon1t at lngs. `http://www.bo.infn.it/xenon/docs/tdr2010.pdf`, 2010.

[50] J. Sulkimo et al. (GEANT4). Geant4-a simulation toolkit. *Nucl. Instrum. Methods Phys. Res. Sect. A*, 506, 2003.

[51] A. Kish. *Dark Matter Search with the XENON100 Experiment*. PhD thesis, Univerity of Zurich (Switzerland), http://opac.nebis.ch/ediss/20121322.pdf, 2011.

[52] E. Aprile et al. (XENON100 Collaboration). Material screening and selection for xenon100. *Astropart. Phys.*, 35, 2011.

[53] E. Aprile et al. (XENON100 Collaboration). Study of the electromagnetic background in the xenon100 experiment. *Phys. Rev. D*, 83, 2011.

[54] N. Ackerman et al. Observation of Two-Neutrino Double-Beta Decay in ^{136}Xe with EXO-200. *Phys.Rev.Lett.*, 107:212501, 2011.

[55] M. Auger et al. Search for Neutrinoless Double-Beta Decay in ^{136}Xe with EXO-200. *Phys.Rev.Lett.*, 109:032505, 2012.

[56] X. Du, R. Purtschert, K. Bailey, B. E. Lehmann, R. Lorenzo, Z.-T. Lu, P. Mueller, T. P. O'Connor, N. C. Sturchio, and L. Young. A new method of measuring ^{81}Kr and ^{85}Kr abundances in environmental samples. 30(20), Oct 2003.

[57] S. Lindemann. Reinigung und nachweis von edelgasen mit miniaturisierten proportionalzählrohren. Master's thesis, University of Heidelberg, 2009.

[58] Table de radionucleides - vol. 4. http://www.bipm.net/utils/common/pdf/monographieRI/Monographie_BIPM-5_Tables_Vol4.pdf, 2008.

[59] M. Weber for the XENON100 collaboration. *A Study of Radon Background in the XENON100 Experiment*, 2011.

[60] Marc Weber. *in preparation*. PhD thesis, University of Heidelberg, 2013.

[61] Sydney Ross and James P. Olivier. *On pyhsical Adsorption*. John Wiley & Sons, 1964.

[62] http://easycalculation.com/chemistry/elements/test.php?name=radon.

[63] K. Abe et al. Distillation of liquid xenon to remove krypton. *arXiv:0809.4413v3 [physics.ins-det]*, 2009.

[64] A. I. Bolozdynya, P. P. Brusov, T. Shutt, C. E. Dahl, and J. Kwong. A chromatogrphic system for removal of radioactive ^{85}kr from xenon. *Nuclear Instruments and Methods in Physics Research A*, 2007.

[65] F. Rouquerol, J. Rouqerol, and K. Sing. *Adsorption by Powders & porous Solids, Principles, Methodology and Applications*. Academic Press, 1999.

[66] D.M. Ruthven. *Principles of Adsorption & Adsorption Processes*. Wiley-Interscience, 1984.

[67] Ralph T. Yang. *Gas Separation by Adsorption Processes*. Imperial College Press, 1997.

[68] Hardy Simgen. *Hochempfindlicher Nachweis radioaktiver Edelgasnuklide und natuerlicher Radionuklide aus der Uran-Zerfallsreihe*. PhD thesis, University of Heidelberg, 2003.

[69] Mark E. Davis and Raul F. Lobo. Zeolite and molecular sieve synthesis. *Chem. Mater*, 4, 1992.

[70] H.W. Langmi et al. Hydrogen adsorption in zeolites a, x, y and rho. *Journal of Alloys and Compounds*, 2003.

[71] G.J. McDougall. The physical nature and manufacture of activated carbon. *J. S. Afr. Min. Metall*, 91(4), 1991.

[72] Norit Americas Inc. Understanding activated carbons - identifying the best type for the application. http://www.norit.com/files/documents/Understanding_AC_rev2.pdf, 2009.

[73] R.C. Bansal, J.-B. Donnet, and F. Stoeckli. *Active Carbon*. Marcel Dekker, 1988.

[74] William A. Steele. The physical interaction of gases with crystalline solids. *Surface Science*, 36, 1973.

[75] S. Sircar, R. Mohr, C. Ristic, and M. B. Rao. Isosteric heat of adsorption: Theory and experiment. *J. Phys. Chem. B*, 103(31), 1999.

[76] Onuma Carmody, Ray Frost, Yunfei Xi, and Serge Kokot. Surface characterisation of selected sorbent materials for common hydrocarbon fuels. *Surface Science*, 2007.

[77] K. Y. Foo and B. H. Hameed. Insights into the modeling of adsorption isotherm systems. *Chemical Engineering Journal*, 156, 2010.

[78] Irving Langmuir. The adsorption of gases on plane surfaces of glass, mica and platinum. *J. Am. Chem. Soc.*, 40, 1918.

[79] H. Freundlich. Ueber die adsorption in loesungen. *Z. Phys. Chem*, 57, 1906.

[80] R. Sips. On the structure of a catalyst surface. *J. Chem. Phys*, 16, 1948.

[81] J. Schick. Entwicklung eines versuchaufbaus zur adsorptionsmessung von radon an aktivkohle. Master's thesis, University of Heidelberg, 2011.

[82] Henry F. Lucas. Improved low-level alpha-scintillation counter for radon. *The Review of Scientific Instruments*, 28(9), 1957.

[83] M. M. Dubinin, E. D. Zaverina, and V. V. Serpinsky. The sorption of water vapour by active carbon. *Chem. Soc.*, 1955.

[84] H. F. Stoeckli, F. Kraehenbuehl, and D. Morel. The adsorption of water by active carbons, in relation to the enthalpy of immersion. *Carbon*, 21(6), 1983.

[85] Neguib M. Hassan, Tushar K. Ghosh, Anthony L. Hines, and Sudarshan K. Loyalka. Adsorption of radon from a humid atmosphere on activated carbon. *Separation Science and Technology*, 1995.

[86] Neguib M. Hassan, Anthony L. Hines, Tushar K. Ghosh, Sudarshan K. Loyalka, and Alan R. Ketring. New apparatus for measuring radon adsorption on solid adsorbents. *Ind. Eng. Chem. Res.*, 1991.

[87] Wolfgang Rau. *Low level radon measurements for the solar neutrino experiment BOREXINO*. PhD thesis, University of Heidelberg, July 1999.

[88] Gianna L. Marschmann. Aufbau und betrieb eines hochempfindlichen detektors zum kontinuierlichen nachweis von radon in xenon. Master's thesis, University of Heidelberg, 2012.

[89] http://www.bluecher.com.

[90] P.H. Emmett S. Brunauer and E. Teller. Adsorption of gases in multimolecular layers. *Journal of the American Chemical Society*, 60, 1938.

[91] http://www.astm.org/DATABASE.CART/HISTORICAL/D6556-04.htm.

[92] http://www.patentstorm.us/patents/7737083/claims.html.

[93] L. A. Vashchenko and V. V. Katal'nikova. Adsorption of helium on zeloite naa. *Russian Chemical Bulletin*, 45(5), May 1996.

[94] L. Duband, A. Ravex, and J. Chaussy. Adsorption isotherms of helium on activated charcoal. *Cryogenics*, 27, July 1987.

[95] Kenzo Munakata, Teruki Fukumatsu, Satoshi Yamatsuki, Kenji Tanaka, and Masabumi Nishikawa. Adsorption equilibria of krypton, xenon, nitrogen and their mixtures on molecular sieve 5a and activated charcoal. *Journal of Nuclear Science and Technology*, 36(9), September 1999.

[96] Susumu Kitani and Junichi Takada. Adsorption of krypton and xenon on various adsorbents. *Journal of Nuclear Science and Technology*, 2(2), February 1965.

List of Figures

List of Tables

Acknowledgements

I want to express my gratitude to all people who enabled me to write this diploma thesis at the MPIK in Heidelberg. To Manfred Lindner, who gave me the opportunity to work in the exciting field of dark matter search, and Willibald Plessas from the University Graz, who made it possible to become a master student at the Max-Planck Institute. Furthermore, I want to thank Manfred for the conferences I could visit during my time in Heidelberg.

This thesis would not have been possible without the help and supervision of my colleagues at the MPIK. I would particularly like to thank Sebastian, Hardy and Marc, who spend a lot of time in answering my questions and helping me in any problems occurring during this work. The right word to express my gratitude is a loud DULLIÖH. Moreover, I am indebted to Jochen, Teresa and Erich for giving their advice in many occasions.

The biggest thanks goes to my parents who have given me any support in all my life decisions.

During the time writing this theses I met so many nice people at the institute who have became very good friends. They made me really enjoying to work at the MPIK and I want to thank them all for the great time.

Heidelberg, 08.04.2013 Stefan A. Brünner

Erklärung:

Ich versichere, dass ich diese Arbeit selbstständig verfasst habe und keine anderen als die angegebenen Quellen und Hilfsmittel benutzt habe.

Heidelberg, den 08.04.2013 .....

(Stefan A. Brünner)